國立臺灣大學工學院化學工程學系
碩士論文
Department of Chemical Engineering
College of Engineering
National Taiwan University
Master’s Thesis

中高壓雙反應器系統二氧化碳加氫生產甲醇
CO_2 Hydrogenation for Methanol Production using Two Reactor System at Medium-High Pressure

邱豔娣
Elicia Kusuma

指導教授：吳紀聖博士
Advisor: Jeffrey Chi-Sheng Wu, Ph.D

中華民國 113 年 7 月
July, 2024

doi:10.6342/NTU202403130

ACKNOWLEDGEMENT

This research and thesis is made possible due to the guidance and support that is received by the author during the process. The author would like to express the highest gratitude to Prof. Jeffrey Chi-Sheng Wu as the advisor in this reseach for providing countless advice and suggestion for the research material. Special thanks is also given to the National Science and Technology Council for providing the opportinuty to conduct this research topic (NSTC112-2221-E-002-016) and provide the author a valuable understanding on industry process.

The author would also like to thank the entire lab member in the Catalyst Laboratory of National Taiwan University in the Department of Chemical Engineering for providing countless assiatance such as teaching the catalyst synthesis, calibrating the gas chromatography, buying materials required for the experiments and assisting troubleshoot during experiments. Lastly, the author is very grateful for her parents for providing financial and moral support for studying and conducting research in National Taiwan University.

doi:10.6342/NTU202403130

ABSTRACT

Pollution has exponentially increased since the industrial revolution. One of the most abundant pollutants within our ecosystem is CO_2, a greenhouse gas that caused rising global temperature and sea level. The scientific field has poured time and resource to reduce greenhouse gas. Along with the depleting source of non-renewable fuel, the prospect of recycling greenhouse gas as a renewable fuel has been on demand. CO_2 pollution can be synthesized as a renewable fuel using H_2 which produces methanol as an easier to store hydrogen-based fuel. Commercially, this process is conducted in at high pressure (50-100 bar) and low temperature (200-250 ^{o}C) with a copper-based catalyst, such as $Cu/ZnO/Al_2O_3$. However, due to the hydrophilic nature of alumina support, catalyst is easily deactivated and thus reduce methanol yield.

One method to increase the production of methanol is water removal via the two-reactor system, where one reactor is used to produce CO by Reverse Water Gas Shift, RWGS, which is then flowed to a desiccator to remove water and the second reactor to reduce mixture of CO and CO_2 to methanol by hydrogenation. To improve the reduction capability, an additional promoter to the $Cu/ZnO/ZrO_2$ catalyst (such as addition of La, Ce, Mo, and W) was tested.

Catalytic hydrogenation showed that $Cu/ZnO/ZrO_2/CeO_2$ (CZZC) catalyst being loaded with an addition of hexagonal Boron Nitride (hBN) showed the best performance for RWGS and CO_2 hydrogenation. The ratio of the metal and hBN is 4:6, as such it is referred as 40CZZC_hBN. RWGS using 40CZZC_hBN had CO selectivity of 99.64%, CO_2 conversion 37.95%, and CO STY 1026.01 mg/g_{cat} h. 40CZZC_hBN performance of MeOH selectivity of 36.42%, CO_2 conversion 12.41%, and methanol STY 140.04 mg/g_{cat} h. In addition, the performance of 40CZZC_hBN in CO conversion of 3.62% and methanol STY of 97.63 mg/g_{cat} h for CO hydrogenation to methanol had better performance than the commercial catalyst with a result of 2.50% conversion and 91.57 mg/g_{cat} h methanol STY.

Lastly, the two reactor system was for CO_2 hydrogenation to methanol was compared to the performance of one reactor system and the result showed an almost similar methanol STY of 127.69 mg/g_{cat} h for the two reactor system with 0.8 g of 40CZZC_hBN loaded in the second reactor compared to 140.04 mg/g_{cat} h for the one reactor system; both operating at 10 bar. The desiccant that is used for water removal in between the two reactor had a significant effect on the methanol yield as using $CaCl_2$ lowers the methanol STY of 86.26 mg/g_{cat}h than using molecular sieve 3A. Increasing the pressure of the two reactor system significantly improved the methanol space time yield as increasing the pressure to 30 bar more than double the methanol STY to 266.11 mg/g_{cat}h. By utilizing two CO_2 hydrogenation to methanol reaction in series, the highest methanol STY can achieve 337 mg/g_{cat} h at 30 bar.

Keyword: CO_2 hydrogenation, copper based catalyst, methanol synthesis, reverse water gas shift, two-reactor system

ABSTRACT (Chinese)

自工業革命以來，污染呈指數級增長。二氧化碳是生態系統中最豐富的污染物之一，這是一種導致全球氣溫和海平面上升的溫室氣體。科學界投入了時間和資源來減少溫室氣體排放。隨著不可再生燃料資源的枯竭，回收溫室氣體作為再生燃料的前景日益迫切。二氧化碳可以使用氫氣合成再生燃料、產生甲醇，作為 更容易儲存的氫基燃料。在商業上，該過程是在高壓（50-100 bar）和低溫（200-250 oC）下使用銅基催化劑例如 Cu/ZnO/Al2O3 進行的。然而，由於氧化鋁載體的親水性，會很容易發生催化劑失活並降低甲醇產率。

提高甲醇產量的一種方法是透過雙反應器系統除水。在雙反應器系統中，其中一個反應器用於透過反向水煤氣變換生產 CO，然後流至乾燥器以除去水，第二個反應器用於減少水。為了提高還原能力，會在 Cu/ZnO/ZrO2 催化劑中加入額外促進劑（例如添加 La、Ce、Mo 和 W）。

加氫反應表明，添加六方氮化硼（hBN）的 Cu/ZnO/ZrO2/CeO2 催化劑顯示出最佳的逆水煤氣變換和 CO2 加氫性能。金屬和 hBN 的重量比例為 4:6，因此這裡將其稱為 40CZZC_hBN。使用 40CZZC_hBN 的逆水煤氣轉換的 CO 選擇性為 99.64%，CO2 轉化率為 37.95%，CO 產率 1026.01 mg/gcat h。 40CZZC_hBN 的甲醇選擇性為 36.42%，CO2 轉化率為 12.41%，甲醇產率為 140.04 mg/gcat h。此外，40CZZC_hBN 在 CO 加氫製甲醇的 CO 轉化率 3.62%和甲醇產率為 97.63 mg/gcat h 方面比商業催化劑 2.50%轉化率和甲醇產率 91.57gcat h 更好。

最後，將用於 CO2 加氫製甲醇的雙反應器系統與一個反應器系統的性能進行比較，結果顯示甲醇產率幾乎相似，對於在第二個反應器中裝載 0.8 g 40CZZC_hBN 的雙反應器系統，甲醇產率為 127.69 mg/gcat h，與單一反應器系統的 140.04 mg/gcat h 相似；兩者皆在 10 bar 下運作。用於兩個反應器之間除水的乾燥劑

對甲醇產率有顯著影響，使用 $CaCl_2$ 時甲醇產率為 86.26 mg/gcath ，比使用分子篩 3A 降低了甲醇產率。增加雙反應器系統的壓力將顯著提高甲醇產率，因為將壓力增加至 30 bar 將使甲醇產率增加一倍以上，甲醇產率為 266.11 mg/gcath。透過串聯兩次 CO_2 加氫至甲醇反應，可以獲得最高的甲醇產率為 337 mg/gcat h，30 bar。

Keyword: CO_2 加氫、銅基催化劑、甲醇合成、逆水煤氣轉換、雙反應器系統

TABLE OF CONTENT

Page

doi:10.6342/NTU202403130

doi:10.6342/NTU202403130

doi:10.6342/NTU202403130

doi:10.6342/NTU202403130

LIST OF ILLUSTRATION

doi:10.6342/NTU202403130

doi:10.6342/NTU202403130

LIST OF TABLES

doi:10.6342/NTU202403130

CHAPTER I

INTRODUCTION

1.1 Background

CO_2 emmision has been a major environmental problem in recent years. As industrial activity grows in term of number and scale, the discharge of CO_2 from fuel combustion also shown to have increase. CO_2 has been classified as greenhouse effect, a category of gases that prevents excess heat from escaping the atmosphere. This resulted in heat being trapped inside the Earth, increasing the global temperature of the planet. As CO_2 is build up the majority of greenhouse gas, reducing CO_2 discharge has been a major issue globally.

Several methods have been proposed to reduce CO_2 emission, such as alternative fuel source and carbon capture. Carbon capture is being done to decrease the amount of CO_2 in the atmosphere while also utilize the captured CO_2 into a more valueable product, such as methanol, that can be used as an alternative for fossil fuel. Methanol is categorized as a blue hydrogen fuel, and has the advantages of easy to be converted to hydrogen, easy transportation, and renewable. Methanol synthesis using CO_2 as the raw material is a promising method to reduce CO_2 emission.

Commercially, methanol synthesis is conducted in at high pressure (around 50-100 bar) and low temperature (200-250 ^oC) with a copper based catalyst, such as $Cu/ZnO/Al_2O_3$. However, due to the hydrophilic nature of alumina support, catalyst poisoning will occur and will induce the side reaction, Reverse Water Gas Shift, producing CO. Thermodynamically, CO_2 hydrogenation to methanol is exothermic, as such the optimal operating condition is harder to control as the methanol selectivity and CO_2 conversion has the opposite effect on the reaction temperature. One method to increase the production of methanol is water removal via the two reactor system, where one reactor is used to produce CO, which is then flowed to a desiccant to remove water and the second reactor

doi:10.6342/NTU202403130

will reduce CO to methanol.

1.2 Problem Formulation

1. What is the best catalyst for CO_2 hydrogenation to methanol, CO hydrogenation to methanol, and RWGS?
2. What is the optimum operating condition for CO_2 hydrogenation to methanol, CO hydrogenation to methanol, and RWGS?
3. What characteristic affects the catalyst’s performance?
4. Which reaction system is better for CO_2 hydrogenation, single reactor or two reactor?

1.3 Purpose of Research

1. Determine the best catalyst to be used for CO_2 hydrogenation to methanol, CO hydrogenation to methanol, and RWGS.
2. Determine the best operating condition (pressure, temperature, catalyst loading) for CO_2 hydrogenation to methanol, CO hydrogenation to methanol, and RWGS.
3. Determine the characteristic that affects catalyst performance.
4. Determine the best operating condition for CO_2 hydrogenation, single reactor or two reactor.

1.4 Scope of Work

Hexagonal boron nitride (hBN) support is chemically exfoliated to ensure it will mix with the metal catalyst. An improved Hummer’s method is employed to chemically exfoliate h-BN at 40 ^oC for 6 hours in 60 mL sulfuric acid. The ratio of h-BN and oxidizing agent $KMnO_4$ is set at 1:3. The exfoliation reaction is then stopped with ice bath and 100 mL of H_2O_2. hBN is then separated from acid via centrifugation at 3000 rpm for 15 minutes and neutralized with NaOH until the pH is 7. The h-BN is then filtered, washed with DI water, dried at 60^oC at least overnight.

The metal loading of the catalyst will be tested at 30 wt.% metal loading, 40 wt.% wt

doi:10.6342/NTU202403130

metal loading and 100 wt.% metal loading. The metals in the catalyst consists of Cu:Zn:Zr:X with the ratio 6:3:(1-y):y, with X being (W, Mo, La, Ce) and y is between 0 and 0.25. The catalyst will be synthesized by mixing the exfoliated h-BN and nitrite salt of each metals via co-precipitation method with Na_2CO_3 until the solution's pH reach 7 and aged for 2 hours. The catalyst is then filtered, washed with DI water, dried at 60^{o}C at least overnight and muffled at 400^{o}C for 4 hours. A Cu/Ce catalyst (Cu:Ce =1:3) is also synthesized using similar condition with the CuZnZr based catalyst to conduct the CO hydrogenation test, the catalyst is tested with and without hBN loaded. Another catalyst is synthesized to be tested for reverse water gas shift reaction, composed of Cu/Fe/Ce (ratio 0.25:0.75:3). This catalyst is synthesized with a similar method.

Hydrogenation reaction is performed with a stainless steel tube reactor, where inert quartz wool are stuffed below and above the catalyst. The standard operating condition for the CO_2 hydrogenation reaction is at 10 bar pressure, 230^{o}C temperature, 0.5 g catalyst loading, 100 mL/min flow rate, and 1:4 ratio of CO_2 and H_2. Reverse water gas shift reaction is being conducted at 1 bar pressure, 350^{o}C and 450 ^{o}C temperature, 0.5 g catalyst loading, 100 mL/min flow rate, and 1:4 ratio of CO_2 and H_2. CO hydrogenation reaction is at 6 bar pressure, 230^{o}C temperature, 0.5 g catalyst loading, 100 mL/min flow rate, and 1:3 ratio of CO and H_2. After finding the best catalyst for each reaction, a two reactor system where the first reactor will conduct reverse water gas shift reaction, followed by water absorption midway and CO/CO_2 hydrogenation in the second reactor. Parameters such as water absorbent type, catalyst loading on the second reactor and catalyst type for the second reactor will be tested to determine the best combination. Another alternative system for the two reactor system where the first and second reactor underwent CO_2 hydrogenaton to methanol and water removal midway is also tested as a comparison.

Catalyst characteristic will be performed with XRD, XPS, H_2-TPR, CO_2-TPD, SEM and

BET. Gas produced by the hydrogenation (H_2, CO_2, CO, and CH_3OH) is analyzed with GC.

1.5 Catalyst Flowchart

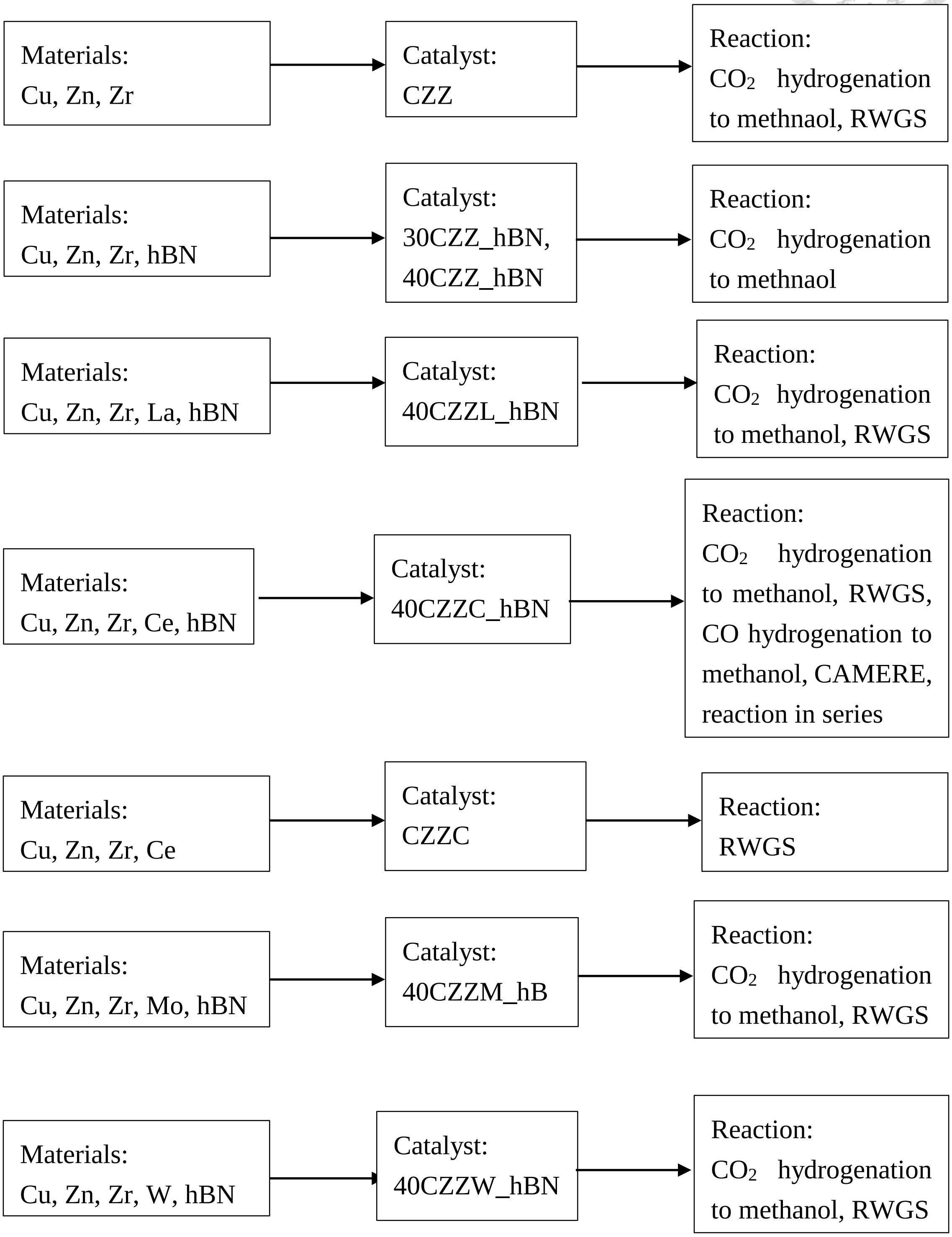

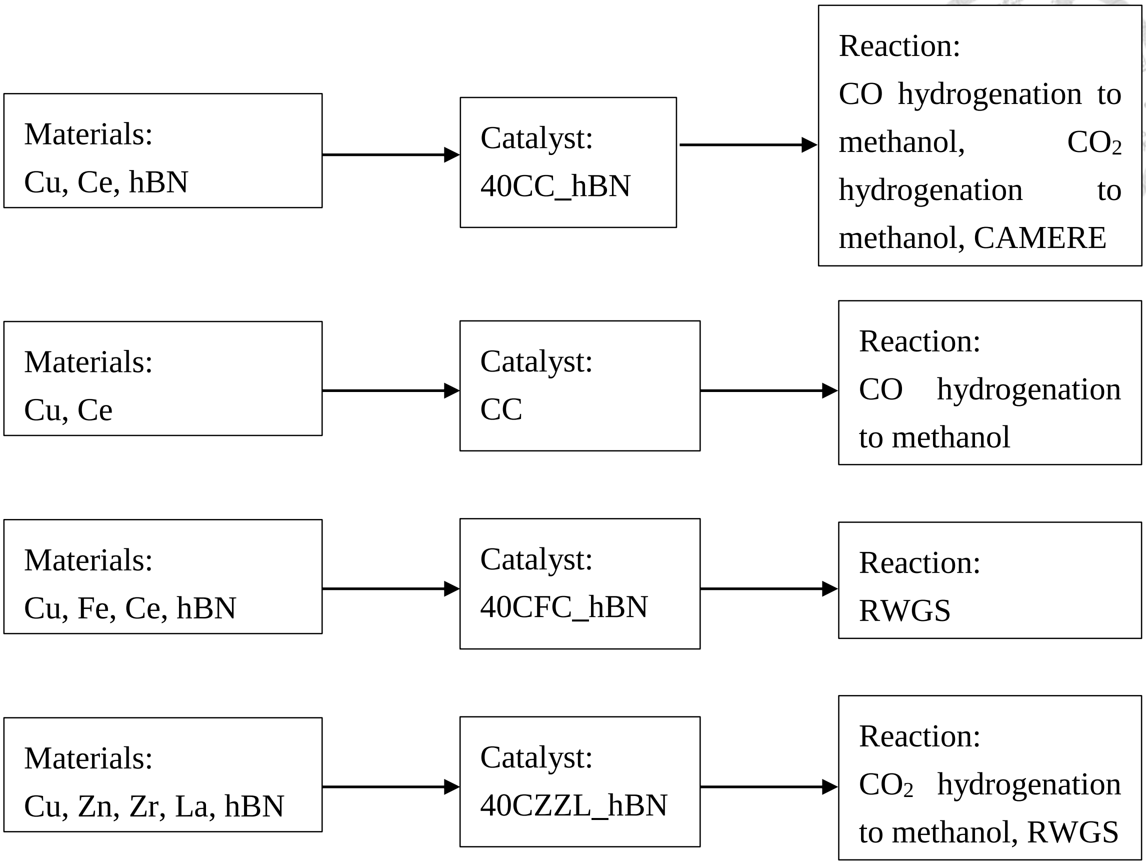
Materials:
Cu, Ce, hBN
Catalyst:
40CC_hBN
Reaction:
CO hydrogenation to methanol, CO_2 hydrogenation to methanol, CAMERE
Materials:
Cu, Ce
Catalyst:
CC
Reaction:
CO hydrogenation to methanol
Materials:
Cu, Fe, Ce, hBN
Catalyst:
40CFC_hBN
Reaction:
RWGS
Materials:
Cu, Zn, Zr, La, hBN
Catalyst:
40CZZL_hBN
Reaction:
CO_2 hydrogenation to methanol, RWGS

CHAPTER II

LITERATURE REVIEW

2.1 CO_2 Emission

2.1.1 Overview

As industrialization and population globally keeps on increasing, a number of human activity such as transportation, power plant, and manufacturing will emit a huge amount of pollution. One of the most prevalent pollution exhaled is carbon dioxide (CO_2). CO_2 is commonly produced via fuel combustion with oxygen, where it will produce CO_2, H_2O and energy (exothermic energy)

$$\mathrm{C_xH_y} + \left(\mathrm{x} + \frac{\mathrm{y}}{4}\right)\mathrm{O_2} \rightarrow \mathrm{x\,CO_2} + \frac{\mathrm{y}}{2}\mathrm{H_2O} + \mathrm{energy}$$

There are several major problems that arise from this fundamental reaction in real life. The first issue is the fuel source commonly used globally are coal, oil and fossil fuels, which are considered non-renewable energy.Non-renewable energy are energy sources that will not generate on a very slow regenation rate, as such the supply is limited. However, the Executive Summary from Internation Energy Agency shows that the share for non-renewable energy global demand remains at a high value at around 80%. An example of coal demand is shown in Fig 2.1.

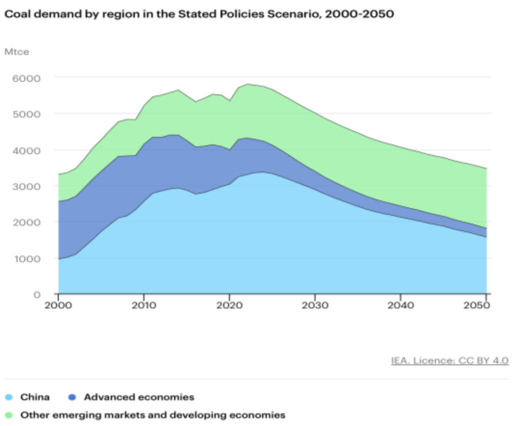

Fig. 2.1 Coal demand trend from 2000-2050 (IEA, 2023)

The second major issue lies on CO_2 itself. CO_2 is one of the abundantly present air pollutant in our atmosphere, where it affect the global climate at large. CO_2 is classified as a Greenhouse Gas (GHG), a category of gases that are capable to trap heat emitted from the sun and prevent them from escaping the Earth's atmosphere. CO_2 make up about 79.4% of GHG, as such limiting and eventually the elimitation of CO_2 emission is seen as a priority. (EPA, 2023) The result is the rising of global temperature that will eventually affect the global climate at large, with the rising global temperature and climate change being the most prominent side effect of excess GHG emission. The trend of CO_2 emission, global temperature and greenhouse gas composition is shown at Fig 2.2, Fig. 2.3, Fig. 2.4 respectively.

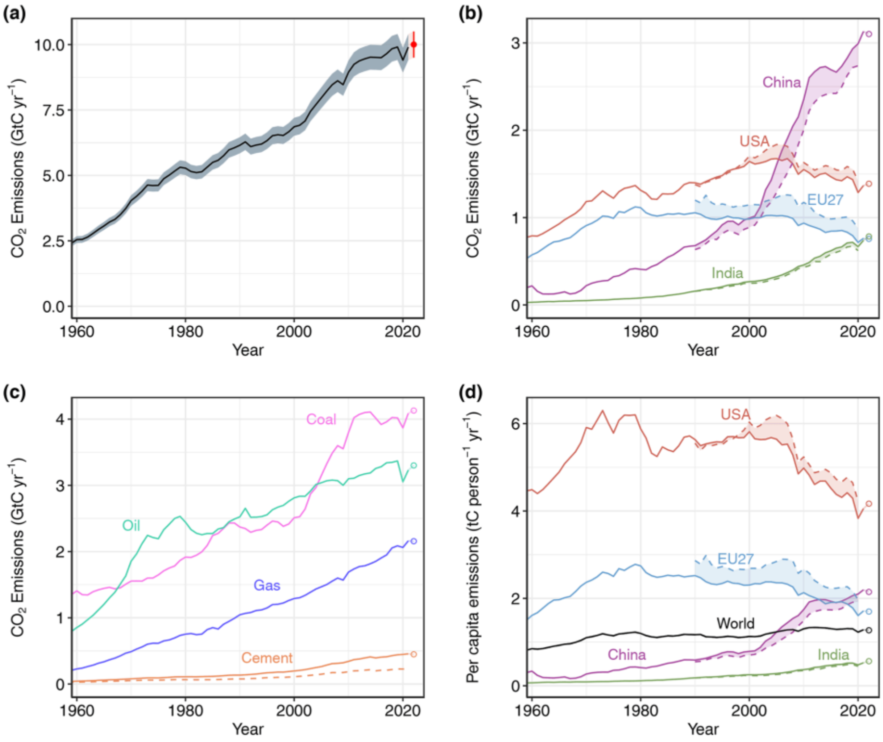

Fig. 2.2 CO_2 emission (a) total, (b) per country, (c) emission source, (d) per capita (Friedlingstein, et al., 2022)

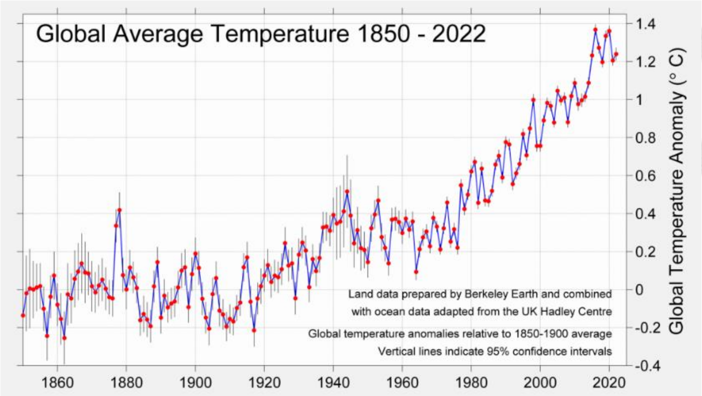

Fig. 2.3 Average global temperature rise (Rohde, 2023)

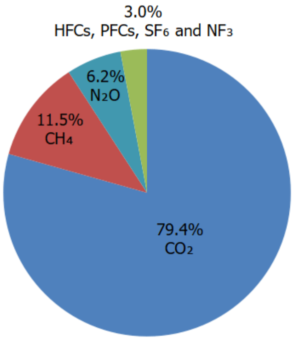

Fig. 2.4 Greenhouse Gas Distribution (EPA, 2023)

2.1.2 Mitigation

Renewable energy such as wind, solar, hydropower, geothermal and biomass has been utilized by several country as an alternative option to non-renewable energy. One of the most promising trait of renewable energy is the availability of the energy sources, without a worry of resource depletion (Owusu and Asumadu-Sarkodie, 2016). High energy demand due to increasing global population will possibly lead to resource depletion as theses resources are being overexploited and overused, which poses a threat for unrenewable energy are becoming scarces in amount (Xu and Zhao, 2023). It also shown that compared to non-renewable energy, renewable energy emits less CO_2 emission to the atmosphere as seen in Fig. 2.5 (Maradin, 2021).

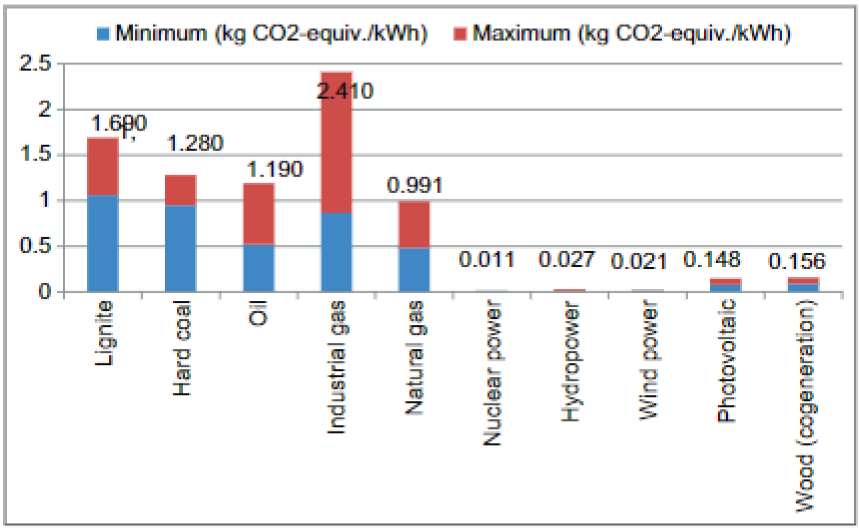

Fig. 2.5 GHG emission of power plant based on fuel source (Maradin, 2021)

However, renewable energy still has some disadvantages such as the dependency on geological location and weather condition. While these advantages can be mitigated by using the natural resources available in a certain region, the most glaring cons is the energy efficiency of these renewable energy, as they have lower electricity capacity production compared to fossil fuel as seen in Fig. 2.6 (Maradin, 2021).

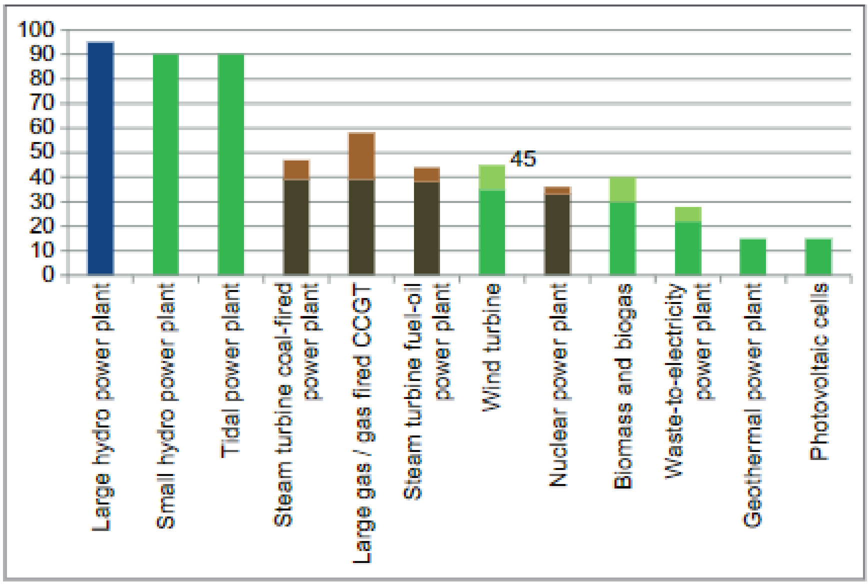

Fig. 2.6 Energy efficiency of power plant based on fuel source (Maradin, 2021)

While the research and development of renewable energy is important for sustainable industry practice, the amount of CO_2 in the atmosphere is still stagnant or rising due to the continuation of using fossil fuel and the emitted pollution is still present. As such, a global scale effort is required in order to decrease the amount of CO_2 emission worldwide. The Paris Agreement signed in 2015 by almost 200 countries has strongly outlined a commitment to keep the global temperature increase below 2^{o}C and low carbon emission. One of the most popular practice to reduce CO_2 emission is carbon capture (Kammerer, et al., 2022). CO_2 that is emitted in the atmosphere will be captured and repurpose as a more valueable product such as methanol, methane, dimethyl ether or formic acid (Yang, et al., 2023). Carbon capture method that has been developed included absorption (chemical and physical), gas-solid reaction, adsorption (chemical and physical), membrane technology, etc. (Yang, et al., 2023). It is estimated that carbon capture has an efficiency of 90% of capturing CO_2 (Peppas et al., 2023). The utilization of CO_2 to a more valuable product is presented in Fig 2.7.

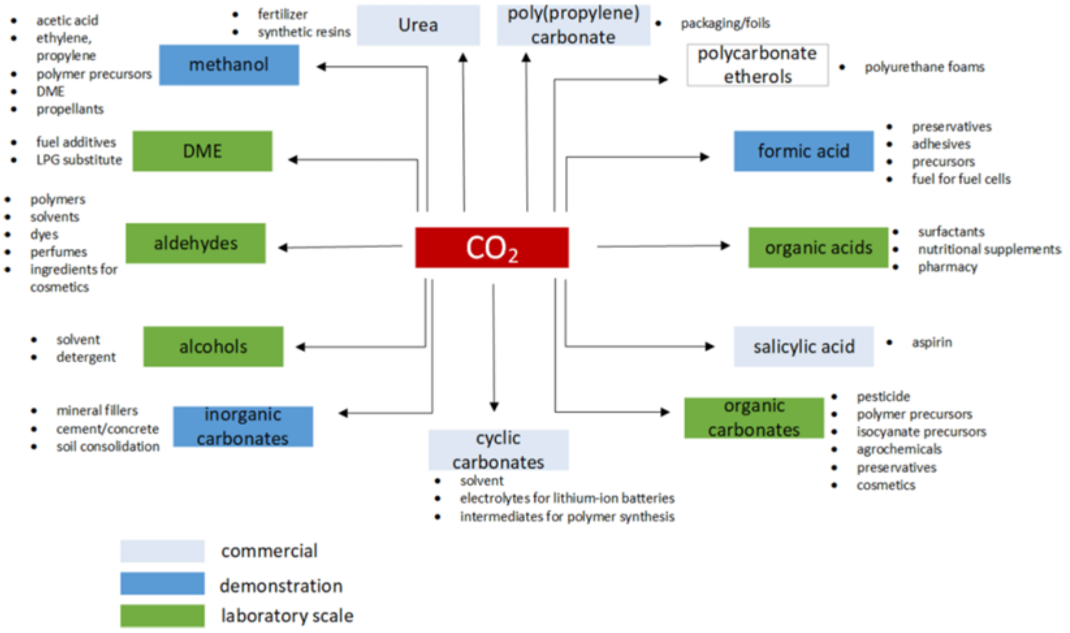

Fig. 2.7 CO_2 utilization (Yang, et al., 2023)

2.2 Methanol Production

As stated above, methanol is one of the product that can be synthesized from captured CO_2. Methanol, also known as methyl alcohol, is the most basic form of alcohol with a chemical formula CH_3OH and is present as a colorless, liquid form in room temperature with an odor similar to ethanol. There are several properties that make methanol a promising fuel alternative as it has higher octane number, higher heat of vaporization and higher oxygen level compared to commercial gasoline fuel (Wang et al., 2019). Furthermore, methanol has a high hydrogen to carbon ratio (4:1) compared to gasoline which makes methanol a highly efficient energy source and lower CO_2 emission (Balachandar et al., 2013). In addition, the absence of C-C bond in methanol's structure will reduce the risk of coking in a machine (Kundu et al., 2007). The synthesis of methanol is commonly conducted in a gas phase,where typically 1 mole of CO_2 is reacted with 3 moles of hydrogen to form methanol and water, a process known as CO_2 hydrogenation as shown in Fig 2.8. (Peppas, et al., 2023).

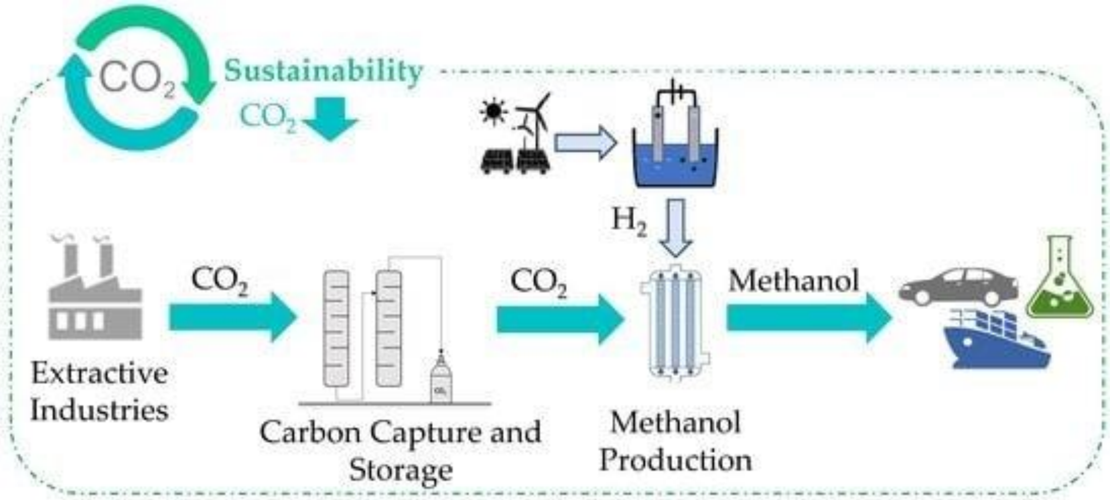

Fig. 2.8 CO_2 hydrogenation process in industry using carbon capture technology (Peppas et al.,2023)

The first recorded instance of methanol synthesis is conducted in 1923 by BASF in Germany using CO and H_2 gas with zinc based catalyst (ZnO/Cr_2O_3) at 300-400 ^oC and 30 MPa. While this process was able to produce 300 ton yearly, this process still has several disadvantages such as high cost due to extreme operating condition, low selectivity, poor activity and pollution caused by chromium in the catalyst (Liu et al., 2023). A more economical process is developed in 1966 by ICI Britain, which requires less pressure and lower temperature. This process utilized copper based catalyst ($CuO/ZnO/Al_2O_3$) with the operating condition of 5-80 MPa and 240-270 ^oC, which has higher methanol selectivity. The only disadvantage of this new process is the need of large vessel, which is why a new process is developed which is based on the ICI method with the only key difference is the operating pressure, which is operated at 10-20 MPa (Liu et al., 2023). The ICI method of methanol production utilized a fixed bed reactor, syngas as feed gas and $Cu/ZnO/Al_2O_3$ as the catalyst (Guczi et al., 2013).

In recent years, CO_2 has been added as inlet gas in methanol production aside from CO and H_2. There has been some suggestion on the role played by CO_2 such as surface structure regulator in copper based catalyst (Klier, 1982), reaction partway alteration by forming formate (Denise et al.,1982), or the main reactant with CO acting as a regenation agent to reduce CuO to Cu on the active site (Chinchen et al., 1987). The chemical reaction for methanol synthesis via syngas hydrogenation is as follow

CO Hydrogenation: $CO + H_2 \rightarrow CH_3OH$ (Liu et al., 2023).

$\Delta H = -90.5$ kJ/mol

CO_2 Hydrogenation: $CO_2 + 3H_2 \rightarrow CH_3OH + H_2O$ (Liu et al., 2023).

$\Delta H = -49.5$ kJ/mol

As the emission of CO_2 emission is increasing annually, research on the prospect of using CO_2 to produce methanol has shown an increasing trend along with the reseach of methanol synthesis. Industrially, an estimation of 90 methanol plant has a combined production rate of 110 million ton every year (Deka et al., 2022).

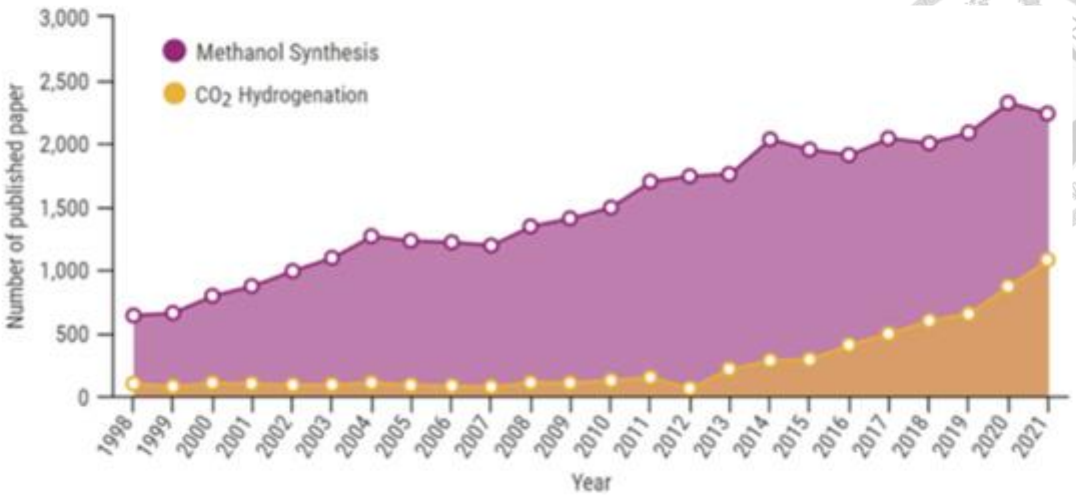

Fig. 2.9 The number of research paper on the topic of CO_2 hydrogenation and methanol synthesis over the years (Azhari et al., 2022)

While this process is shown to have a promising result, there are several drawbacks of using CO_2 as the main reactant for methanol synthesis. As seen in the reaction equation above, CO_2 hydrogenation to methanol will produce water, which will inhibit the catalyst and cause deactivation. The commercial catalyst uses Al_2O_3 as a support, mainly to increase the surface area, which is hydrophilic thus attract water to catalyst surface. As there is two known reaction pathway in CO_2 hydrogenation to methanol, there is a possibility of side reaction that will eventually reduce the methanol yield. CO_2 will activate on the active site and form intermediate function group radicals such as HCOO*, *COOH, $*CO_3$, $*HCO_3$ or *CO. These intermediate function group will then form $*CH_3O$ and desorb from the catalyst surface. The hydrogenation step has two variations: the formate pathway (involves HCOO*, the favorable pathway) and reverse water gas shift pathway (involves *COOH or *CO and will produce CO instead, the unfavorable route) (Yan et al., 2022). Lastly, the tempature of CO_2 condition is hard to control as a low operating temperature will reduce the CO_2 conversion but increase the methanol selectivity and vice versa (Yang et al., 2022).

2.3 CAMERE Reaction

As the number of research regarding CO_2 hydrogenation is steadily increasing, so does the research aimed to minimize the factors that inhibits CO_2 hydrogenation. One such method is the CAMERE (Carbon dioxide hydrogenation to form methanol via a reverse water gas shift) reaction, first reported by a German company Lurgi (Goehna & Koenig, 1994). The majority of methanol synthesis is conducted using copper based catalyst and it is reported that this type of catalyst has inferior activity in feed without CO (Joo et al., 1999). This due to the side product of pure CO_2 hydrogenation, water that will be adsorbed on the active site and eventually deactivate the catalyst. To mitigate this phenomena, an addition of CO is required to react with water and form CO_2 and H_2 which will regenerate the catalyst active site. This process can be achieved using two reactors connected in series, where the first reactor will undergo reverse water gas shift reaction, and the second reactor will produce methanol.

The operating condition for the first reactor is high temperature and ambient pressure due to the chemical equilibrium and thermodynamics behavior. The goal of the first reactor is to convert CO_2 and H_2 into CO and water. Due to water being an inhibitor for methanol synthesis catalyst, it will be removed via water absorbtion prior to entering the second reactor. Due to the reverse water gas shift, the feed of the second reactor will be $CO/CO_2/H_2$ where both CO and CO_2 will undergo hydrogenation to form methanol. The operating condition for the second reactor uses a lower temperature compared to the first reactor and high pressure.

Reverse Water Gas Shift $CO_2 + H_2 \rightarrow CO + H_2O$ Yang et al., 2022

$$\Delta H = 41.5 \text{ kJ/mol}$$

The CAMERE reaction has been tested on a laboratory scale and minipilot scale. The

doi:10.6342/NTU202403130

laboratory scale test shows that a mixture of carbon gas (CO_2 and CO) will have a better methanol yield compared to an inlet gas with only CO_2 or CO as the carbon gas, as see in Fig 2.10. As a reference, the value of A that used by Lurgi for the MegaMethanol technology is 0.26 (Wurzel, 2006).

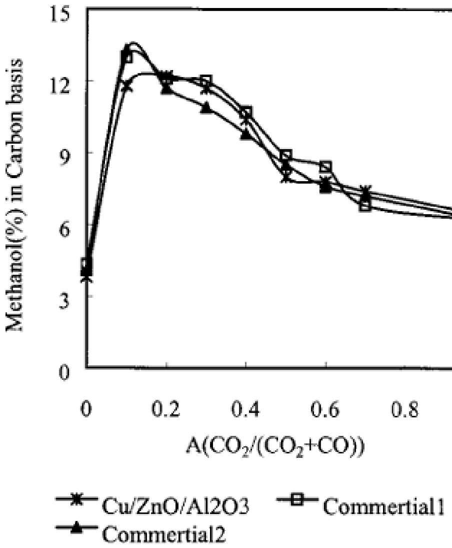

Fig. 2.10 Methanol yields per pass depending on the A value. Reaction conditions: 523 K, 27.2 atm, GHSV of 19 200, H_2 / (CO_2 + CO) =3 (Joo et al., 1999)

For the minipilot, the reverse water gas shift reactor is aligned serially with the methanol synthesis reactor. In addition, the downstream of each reactor is recycled to the reactors and water is removed from the outlet prior to being recycled. The result shows that there is a lower recycle is lower compared to conventional methanol synthesis process. The capital cost is also reduced compared to commercial process due to the absence of reformer but higher operatorional cost due to operation of two reactors. The comparison of the commercial and CAMERE reaction is presented in Table 2.1. As the methanol systhesis process with recycle feed for CAMERE reaction requires less feed gas to synthesize more methanol and exhibits a higher CO_2 conversion, CAMERE reaction is an optimal option for methanol synthesis.

Table 2.1 Comparison of the CAMERE process with the direct CO2 hydrogenation (Joo et al., 1999)

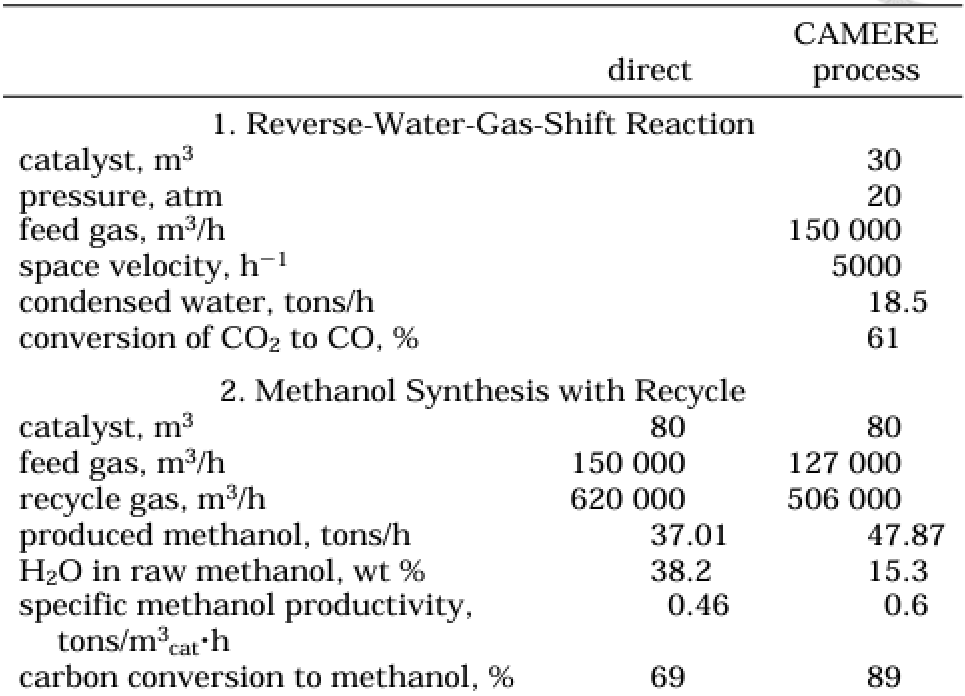

	direct	CAMERE process
1. Reverse-Water-Gas-Shift Reaction		
catalyst, m^3		30
pressure, atm		20
feed gas, m^3/h		150 000
space velocity, h^{-1}		5000
condensed water, tons/h		18.5
conversion of CO_2 to CO, %		61
2. Methanol Synthesis with Recycle		
catalyst, m^3	80	80
feed gas, m^3/h	150 000	127 000
recycle gas, m^3/h	620 000	506 000
produced methanol, tons/h	37.01	47.87
H_2O in raw methanol, wt %	38.2	15.3
specific methanol productivity, tons/m^3_{cat}·h	0.46	0.6
carbon conversion to methanol, %	69	89

2.4 Catalyst Material

To ensure maximum catalytic activity, the suitable material is required to ensure a high catalytic activity. One of the most common material that is used as the active site for methanol synthesis is copper. Copper has exhibited a high activity for CO_2 hydrogenation to methanol at a lower temperature, cheap, multiple oxidation states (Cu^0, Cu^I, Cu^{II}), stable under oxygen environment, strong metal-support interaction, H_2 dissociation property, high surface area and small particle size compared to nickel, rhuthenium and galium (Murthy et al., 2021). The most commonly used promoters for copper based catalyst are ZnO, ZrO_2, and Al_2O_3, which can function to modify the surface of Cu and increasing the catalytic activity for methanol synthesis.

ZnO is a metal commonly used in copper-based catalyst due to the “Cu-Zn synergy” effect that will promote the activity of CO_2 hydrogenation to methanol. DFT study of this

Cu-Zn metal support interaction is conducted to study the effect of Zn addition for CO and CO_2 addition as seen in Fig 2.11.

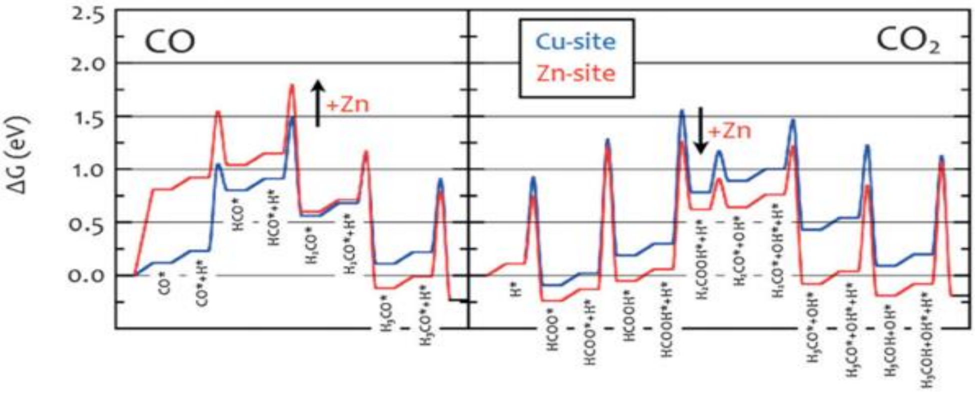

Fig. 2.11 DFT calculation of CO and CO_2 hydrogenation for Cu site and Zn site (Studt et al., 2015)

From the figure above, it is shown that Zn will stabilize the oxygen binding sites of the catalyst during CO_2 hydrogenation, boosting the catalytic activity. However, for CO hydrogenation, the intermediate pathway will bind C atoms and will be hindered by Zn. As such, Cu site will be active for CO hydrogenation but became slower on CO_2 hydrogenation due to surface coverage by formate. For CO/CO_2 mixture, the synergy of Cu and Zn can be utilized to compensate the extreme ends of the two active sites' reaction mechanism as demonstated in Fig 2.12.

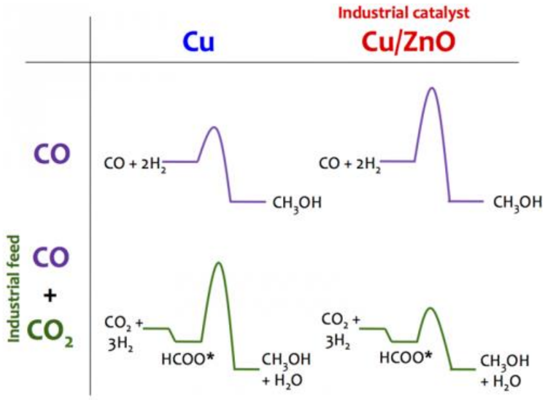

Fig. 2.12 Schemcatic diagram of activation energy of CO/CO_2 using Cu or Cu/ZnO based catalyst (Studt et al., 2015)

doi:10.6342/NTU202403130

Al_2O_3 is often added to copper based catalyst due to its high surface area and thermal stability (Li et al., 2020). The combination of Cu/ZnO/Al_2O_3 as the commercial catalyst for CO_2 hydrogenation to methanol since 1966, but it still has some disadvantages. The main issue of Al_2O_3 is its hydrophilic property that will cause catalyst deactivation. Some alternatives for Al_2O_3 has been proposed such as ZrO_2 (Todaro et al., 2022). ZrO_2 also boost higher thermal stability, stronger interaction with copper and hydrogen storage capacity (Wang et al., 2019).

Other elements has also been incorporated as a new promoter to boost reaction activity for copper based catalyst such as Mo, W, Cr, La, Ce, Nd and Pr. The effect of Mo, W, and Cr was tested on CO_2 hydrogenation to methanol under the condition of 30 bar pressure, 240 ^{o}C, Gas feed (CO_2/H_2/N_2) : 23.5:64.5:12 and GHSV 2400 mL/g_{cat} h (Wang et al., 2019). The catalytic activity compared to catalyst without additional promoter is seen in Fig 2.13.

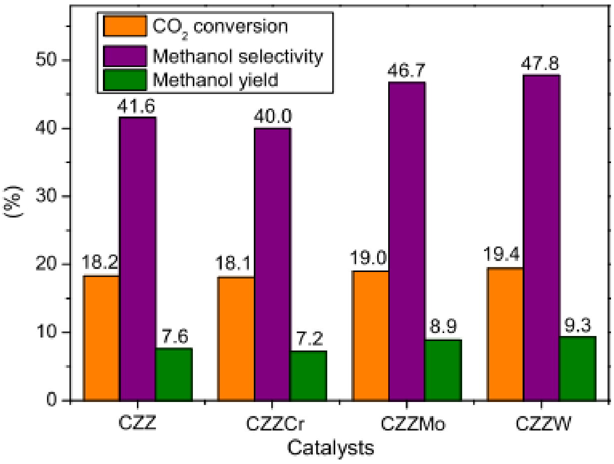

Fig. 2.13 Hydrogenation performance of CZZ based catalyst (Wang et al., 2019)

The addition of Mo and W shows an improvement of catalytic performance compared to the undoped catalyst. Interestingly, Cr doped catalyst shows an inferior performance compared to the control, while some literature shows Cr can increase catalytic activity, which may occur due to the difference of catalyst composition. Some characteristic test has been conductred to determine how the catalyst component and morphology affect the performance of CO_2 hydrogenation. XRD profile of the four catalyst tested is shown in Fig 2.14.

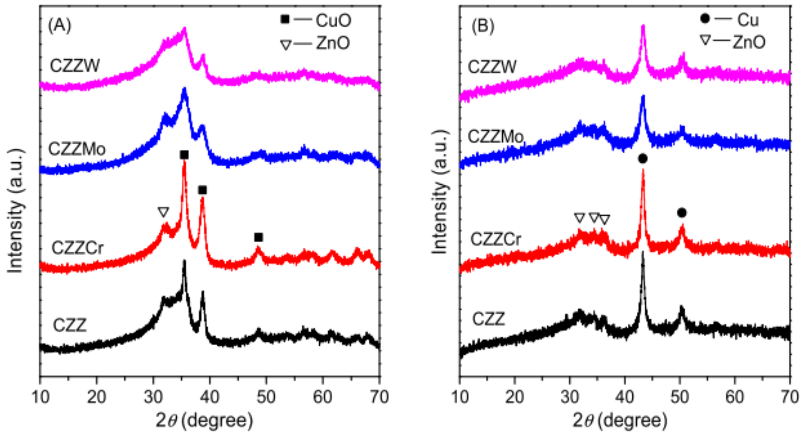

Fig. 2.14 XRD profile of (a) fresh catalyst and (b) reduced catalyst of CZZ based catalyst (Wang et al., 2019)

The addition of Mo and W broaden the XRD peak for Cu in fresh and reduced catalyst suggesting, CuO crystal inhibition. While the opposite happens on the Cr doped catalyst, where CuO crystallization promotion occurs. Furthermore all catalyst shows CuO and ZnO peak overlapping which suggest a strong interaction between Cu/Zn. Some physiochemistry characteristic, such as surface area, pore size and dispersion is presented at Table 2.2.

Table 2.2 Physicochemistry characteristic of CZZ based catalyst (Wang et al., 2019)

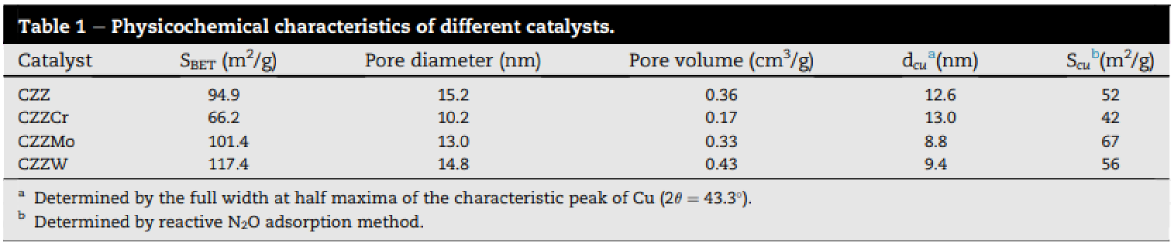

Table 1 – Physicochemical characteristics of different catalysts.

Catalyst	S_{BET} (m^2/g)	Pore diameter (nm)	Pore volume (cm^3/g)	d_{Cu} [a] (nm)	S_{Cu} [b] (m^2/g)
CZZ	94.9	15.2	0.36	12.6	52
CZZCr	66.2	10.2	0.17	13.0	42
CZZMo	101.4	13.0	0.33	8.8	67
CZZW	117.4	14.8	0.43	9.4	56

[a] Determined by the full width at half maxima of the characteristic peak of Cu ($2\theta = 43.3°$).
[b] Determined by reactive N_2O adsorption method.

From the table above, the performance is affected by the surface area, pore size and dispersion. CZZCr is shown to have the lowest parameter value which is reflected on the catalytic activity performance, compared to CZZMo and CZZW which has higher surface area and copper dispersion than CZZ. Another characteristic that is performed is CO_2-TPD (temperature programmed desorption) and H_2-TPR (temperature programmed reduction). The result is shown in Fig 2.15 and Table 2.3.

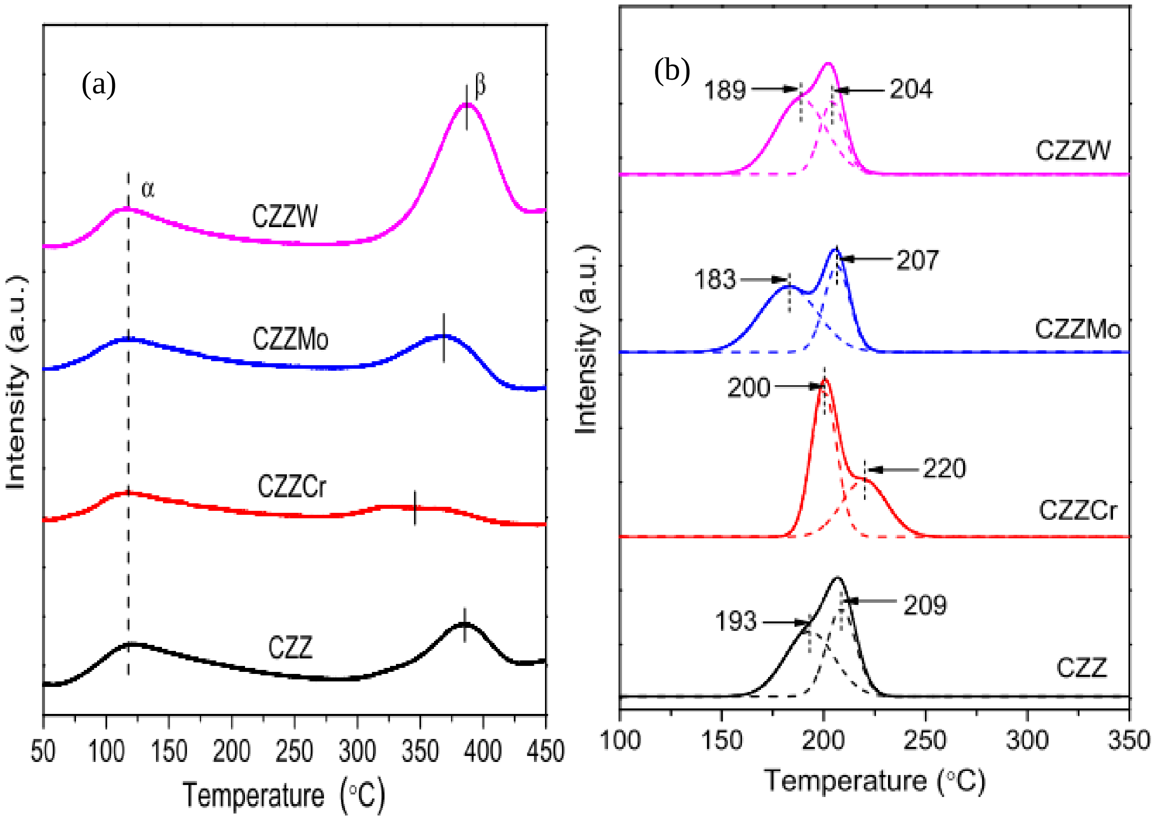

Fig. 2.15 (a) CO_2-TPD and (b) H_2-TPR result of CZZ based catalyst (Wang et al., 2019)

Table 2.3 (a) CO_2-TPD and (b) H_2-TPR summary result of CZZ based catalyst (Wang et al., 2019)

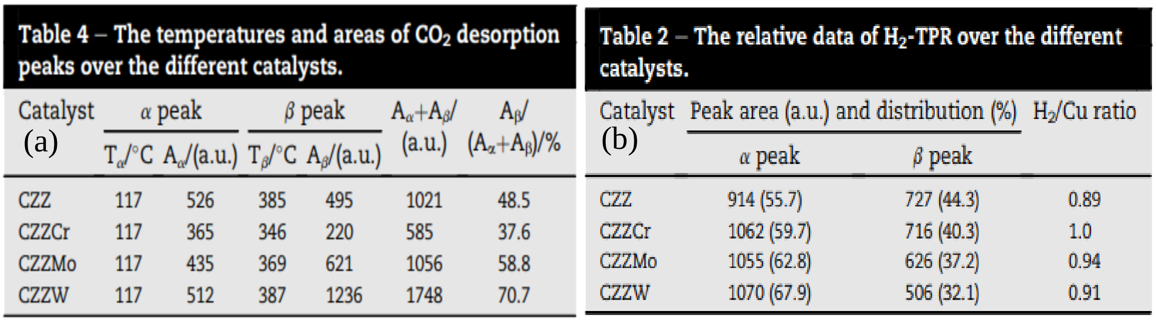

Table 4 – The temperatures and areas of CO_2 desorption peaks over the different catalysts.

Catalyst (a)	α peak		β peak		$A_\alpha+A_\beta$/(a.u.)	$A_\beta/(A_\alpha+A_\beta)$/%
	T_α/°C	A_α/(a.u.)	T_β/°C	A_β/(a.u.)		
CZZ	117	526	385	495	1021	48.5
CZZCr	117	365	346	220	585	37.6
CZZMo	117	435	369	621	1056	58.8
CZZW	117	512	387	1236	1748	70.7

Table 2 – The relative data of H_2-TPR over the different catalysts.

Catalyst (b)	Peak area (a.u.) and distribution (%)		H_2/Cu ratio
	α peak	β peak	
CZZ	914 (55.7)	727 (44.3)	0.89
CZZCr	1062 (59.7)	716 (40.3)	1.0
CZZMo	1055 (62.8)	626 (37.2)	0.94
CZZW	1070 (67.9)	506 (32.1)	0.91

There are 2 peaks that are observed in CO_2-TRP:α peak (low temperature/weak basic adsorption) and β peak (high temperature/strong basic adsorption). To determine the performance of CO_2 desorption, we need to calculate the ratio of β peak area and total peak area and it shows that the performance is CuZnZrW (CZZW)> CuZNZrMo (CZZMo) > CuZnZr (CZZ) > CuZnZrCr (CZZCr) which aligns with the experimental result.

There are 2 peaks that are observed in H_2-TRP:α peak (CuO dispered phase) and β peak (CuO bulk) in CZZCr the peak appears at higher temperature (larger CuO particle size) which aligns with the XRD result. The H_2/Cu ratio is close 1 in all sample, suggesting that majority of CuO is reduced. Lastly, the XPS result to observe the element surface valence, as seen in Fig 2.16 and Table 2.4.

doi:10.6342/NTU202403130

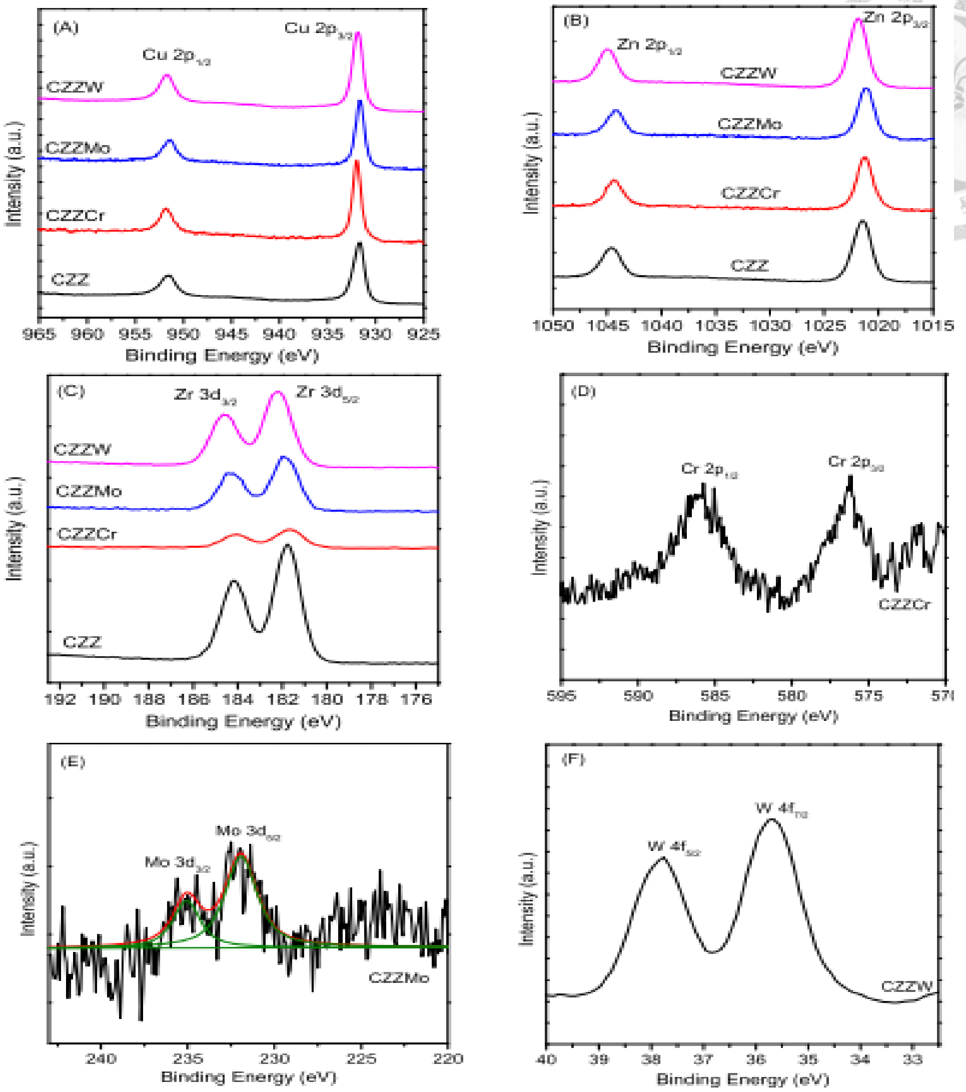

Fig. 2.16 XPS figure of (a) Cu 2p (b) Zn 2 (c) Zr 3d (d) Cr 2p (e) Mo 3d and (f) W 4f

Table 2.4 XPS summary of (a) Cu 2p (b) Zn 2 (c) Zr 3d (d) Cr 2p (e) Mo 3d and (f) W 4f

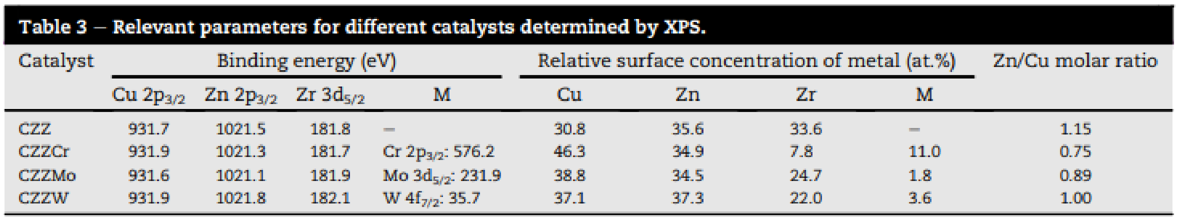

Table 3 – Relevant parameters for different catalysts determined by XPS.

Catalyst	Binding energy (eV)				Relative surface concentration of metal (at.%)				Zn/Cu molar ratio
	Cu $2p_{3/2}$	Zn $2p_{3/2}$	Zr $3d_{5/2}$	M	Cu	Zn	Zr	M	
CZZ	931.7	1021.5	181.8	–	30.8	35.6	33.6	–	1.15
CZZCr	931.9	1021.3	181.7	Cr $2p_{3/2}$: 576.2	46.3	34.9	7.8	11.0	0.75
CZZMo	931.6	1021.1	181.9	Mo $3d_{5/2}$: 231.9	38.8	34.5	24.7	1.8	0.89
CZZW	931.9	1021.8	182.1	W $4f_{7/2}$: 35.7	37.1	37.3	22.0	3.6	1.00

The XPS result shows the electron state of each component in a CZZ catalyst. The most noticeable difference is the amount of Zr^{4+} in each sample. While not stated it could be due to electron transfer from Zr^{4+} to M^{n+} (more transfer happen on CZZCr). In most literature, the formation of methanol is often attributed to the Zn/Cu ratio of the catalyst, with higher value encourage more methanol formation via the formate route.

Other research has utilized different promoter for CZZ based catalyst such as La, Ce, Nd and Pr. In several literatures, La_2O_3, a rare earth element, has been shown to improve the surface property of methanol synthesis catalyst (Ban et al., 2014). The catalytic test is conducted with 1 gram of catalyst at 30 bar pressure, 210-250 ^oC temperature and gas feed composition of CO_2 and H_2 at 1:3. The catalyst characterization conducted are XRD, XPS and H_2-TPR. The catalytic test is conducted with different temperature and space time yield is presented on Fig 2.17 and Table 2.5.

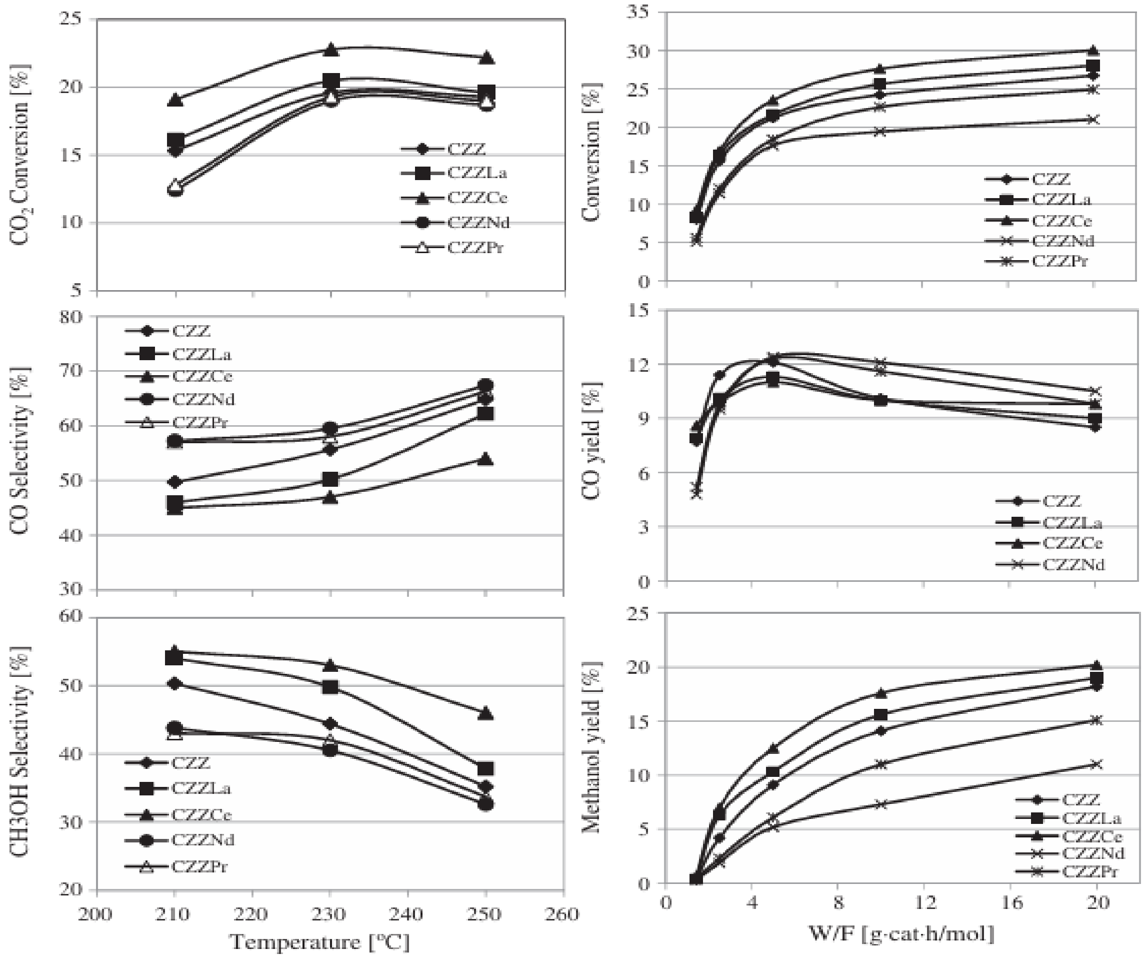

Fig. 2.17 The effect of temperature and W/F (weight/volumetric flow rate) on methanol sythesis (Ban et al., 2014)

Table 2.5 The CO_2 conversion, methanol selectivity and methanol production (Ban et al., 2014)

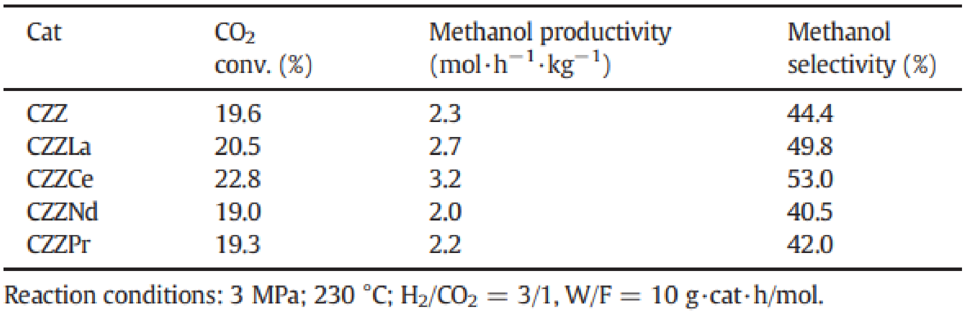

Cat	CO_2 conv. (%)	Methanol productivity ($mol \cdot h^{-1} \cdot kg^{-1}$)	Methanol selectivity (%)
CZZ	19.6	2.3	44.4
CZZLa	20.5	2.7	49.8
CZZCe	22.8	3.2	53.0
CZZNd	19.0	2.0	40.5
CZZPr	19.3	2.2	42.0

Reaction conditions: 3 MPa; 230 °C; $H_2/CO_2 = 3/1$, W/F = 10 g·cat·h/mol.

As shown above, the CO_2 conversion will increase with temperature and reach the maximum value at 230 ^oC and the methanol selectivity will decrease with temperature due to the decreasing amount of CO produced as CO production is elevated at higher temperature as such the optimal operating temperature is 230 ^oC. The effect of space time yield is also studied and is used to study the reaction route of methanol synthesis. With short contact time, methanol synthesis is not as significant as CO synthesis, suggesting that short term catalytic test will produce more CO but will steadily produced more methanol with more contact time. The increasing amount of methanol synthesis also indicates there are two parallel routes for methanol synthesis which is direct CO_2 hydrogenation and CO hydrogenation. CZZCe shows the best catalytic performace out of all CZZ based catalyst in this experiment. We can also observe the XRD peak to study the crystallinity of the catalyst, as seen in Fig 2.18.

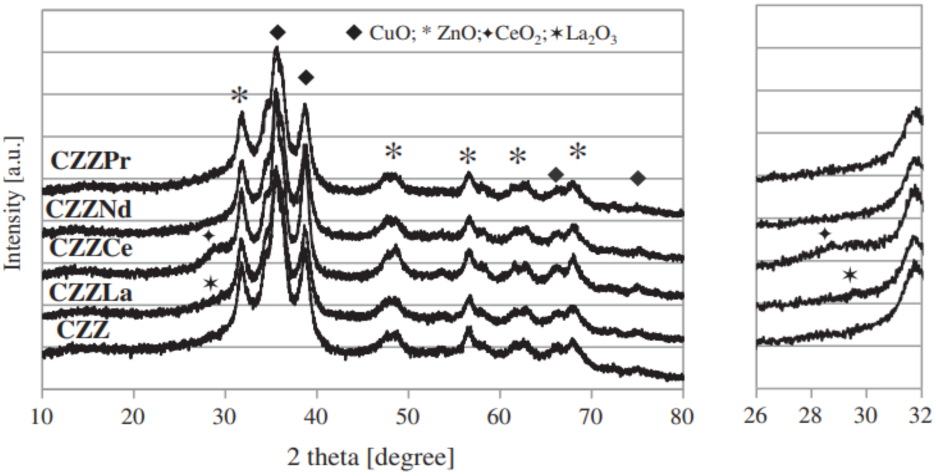

Fig. 2.18 XRD profile of CZZ based catalyst (Ban et al., 2014)

The XRD profile shows a poor cystalinity of CuO in all catalyst along with some overlaying ZnO peaks which suggest a strong interaction of CuO and ZnO. However, ZrO_2 peak is not noticeable due to the small quantity or fine dispersion of ZrO_2. There is a small peak of La_2O_3 and CeO_2 detected in XRD, indicating a presence of these metal oxide crystal at the calcination temperature of 400 ^{o}C, which is not observed for Nd and Pr catalyst, suggesting an amorphous structure (Ban et al., 2014). Next, the XPS profile of Cu 2p is shown in Fig 2.19.

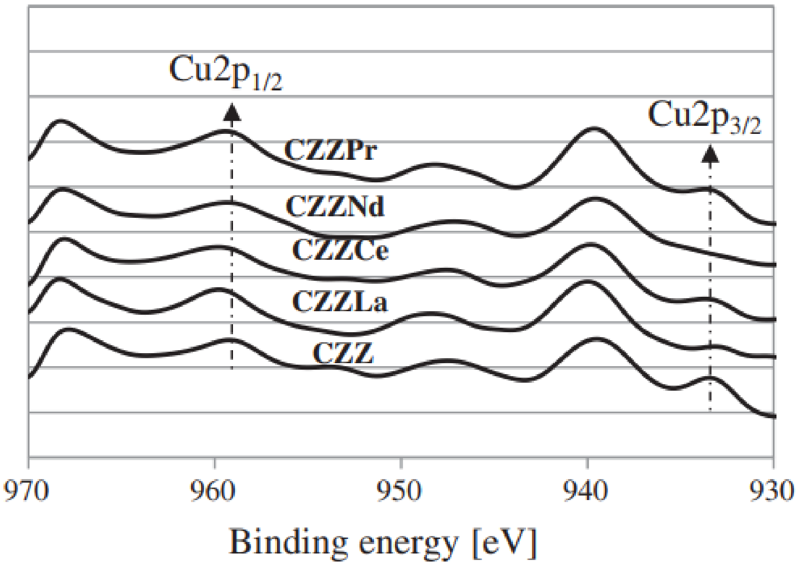

Fig. 2.19 XPS profile of CZZ based catalyst (Ban et al., 2014)

XPS of Cu 2p$_{3/2}$ is present at 933.6 eV indicating a presence of CuO and 940 eV peak correspondent to Cu^{2+}. There is a lack of peak at 932 eV which is a sign of negligible amount of Cu^0 and Cu^+. CZZLa and CZZPr demostraste a shift at CuO peak with could occur due to metal interaction with copper and is absent in CZZCe and CZZNd. Lastly, H_2-TPR is observed at Fig 2.20.

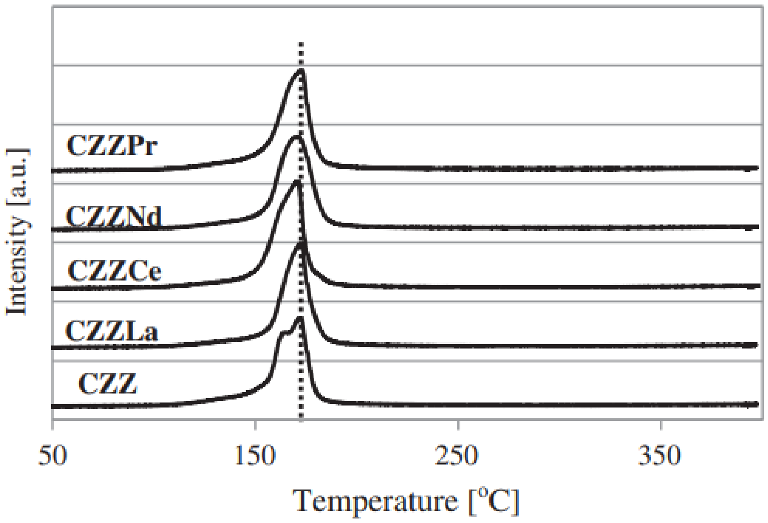

Fig. 2.20 H_2-TPR of CZZ based catalyst (Ban et al., 2014)

H_2-TPR is used to determine the reducibility of a material under hydrogen envirionment. The CZZ peak shows two obvious peak which corresponds to α peak (CuO dispered phase) and β peak (CuO bulk). The doped catalyst mostly shows a more uniform peak with CZZCe and CZZLa having lower temperature peak thus promote Cu reduction more. This also align with the catalytic performance test, where CZZLa and CZZCe shows a better result than CZZ.

CO_2 hydrogenation gained a lot of traction due to the collective goal of reducing carbon emission and minimizing the effect of climate change, as such research on CO hydrogenation catalyst is done not as much as CO_2 hydrogenation in terms of quantity. One research conducted on CO hydrogenation utilized on copper and ceria as the catalyst material (Shen et al., 2005). The aim is to synthesize a catalyst with a similar or higher activity for methanol synthesis compared to palladium ceria based catalyst due to the

doi:10.6342/NTU202403130

enormous amount of palladium required which is not economically feasible. Copper ceria based catalyst with different copper loading is tested with 0.5 grams of catalyst at 195 ºC and 20 bar, with the result being shown at Table 2.6.

Table 2.6 Catalytic activity of copper-ceria catalyst compared to commercial catalyst (Shen et al., 2005)

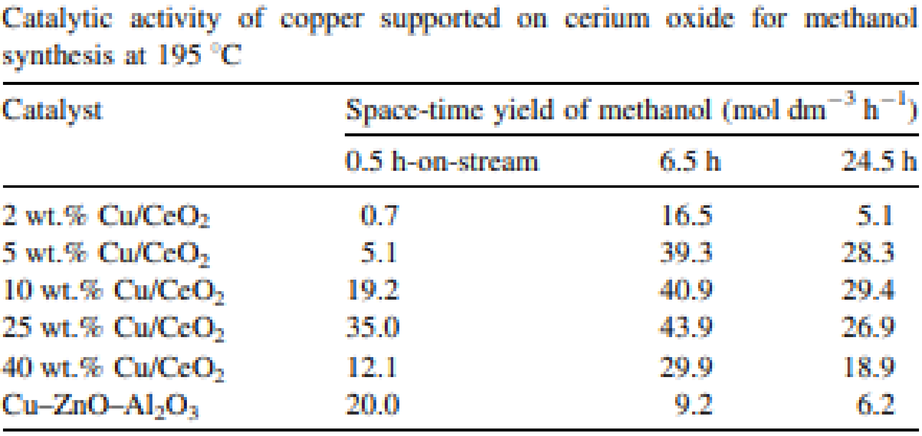

Catalytic activity of copper supported on cerium oxide for methanol synthesis at 195 °C

Catalyst	Space-time yield of methanol (mol dm^{-3} h^{-1})		
	0.5 h-on-stream	6.5 h	24.5 h
2 wt.% Cu/CeO$_2$	0.7	16.5	5.1
5 wt.% Cu/CeO$_2$	5.1	39.3	28.3
10 wt.% Cu/CeO$_2$	19.2	40.9	29.4
25 wt.% Cu/CeO$_2$	35.0	43.9	26.9
40 wt.% Cu/CeO$_2$	12.1	29.9	18.9
Cu–ZnO–Al$_2$O$_3$	20.0	9.2	6.2

At copper loading of 5+%, Cu/CeO$_2$ shows a superior STY$_{MeOH}$ compared to the commercial Cu/ZnO/Al$_2$O$_3$ catalyst, with 10% Cu/CeO$_2$ showing the best result for long duration reaction while 25% Cu/CeO$_2$ showing the best result for short term duration reaction. The performance of 10% Cu/CeO$_2$ compared to commercial catalyst over time is shown in Fig 2.21.

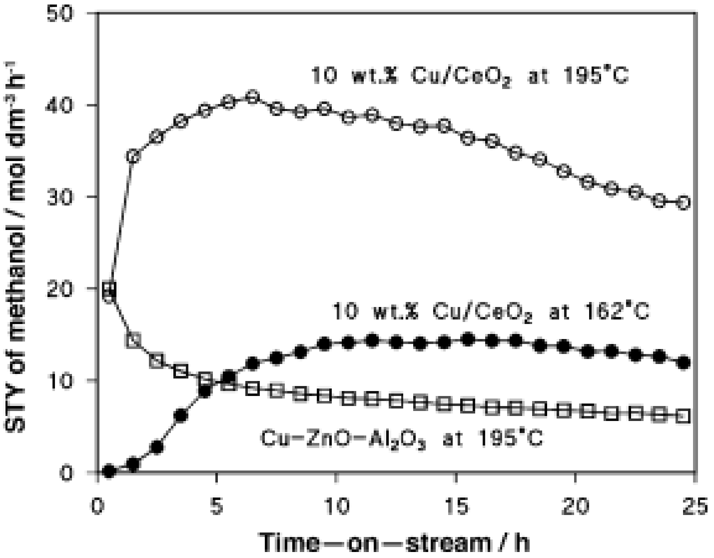

Fig. 2.21 Methanol synthesis from CO hydrogenation with 10% Cu/CeO_2 at 2.0 MPa compared to commercial catalyst (Shen et al., 2005)

10% Cu/CeO_2 catalyst even shows a better result at a lower temperature compared to the commercial catalyst. XRD profile of fresh and reduced catalyst is shown in Fig 2.22.

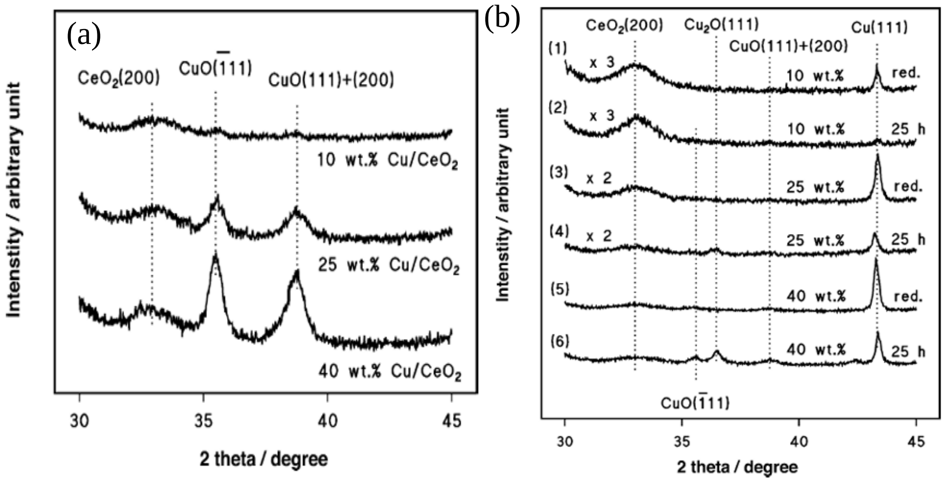

Fig. 2.22 XRD profile of (a) fresh catalyst and (b) reduced catalyst (Shen at al., 2005)

In the fresh catalyst, at small copper loading there is an absent of CeO_2 compared to the ones with higher copper content. Using the XRD plot the average CeO_2 crystal size is around 4 nm and appears at the 28.6^o which correspondent to CeO_2 (111) and the average CuO crystal size is 14 nm which appears at 35.5^o. In the reduced profile, Cu is noticeable reduced and there is a crystal size growth for Cu (14 nm to 32 nm) and Ce (4 nm to 14 nm). Lastly the H_2-TPR profile is shown in Fig 2.23.

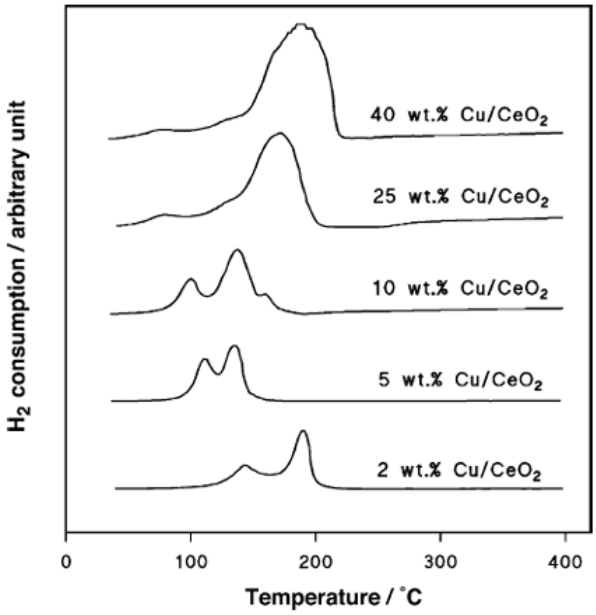

Fig. 2.23 H_2-TPR profile of copper-ceria based catalyst (Shen et al., 2005)

The H_2-TPR result shows that 10% Cu/CeO_2 shows peak at lower temperature compared to 2% and 5% Cu/CeO_2 profile, showing that 10% Cu/CeO_2 is more readily reduced compared to the latter two. In comparison the 25% and 40% has small peaks present at 60-100 ^{o}C and the largest peak at 140-200 ^{o}C.

For reverse water gas shift, one material that has been tested to enhance the performance is iron. Iron is known to form a strong metal interaction with CeO_2, a material that has been known to possess high oxygen vacancy. This characteristic is adventagous for copper based catalyst as sintering is a major drawback for copper based catalyst (Lin et al., 2019). FeO_x acts as a stabilizing promoter that prevents catalyst aggregation at reverse gas shift condition (high termperature and H_2 rich environment). The performance of Cu/FeO_x/CeO_2 catalyst with different composition is presented in Fig 2.24.

doi:10.6342/NTU202403130

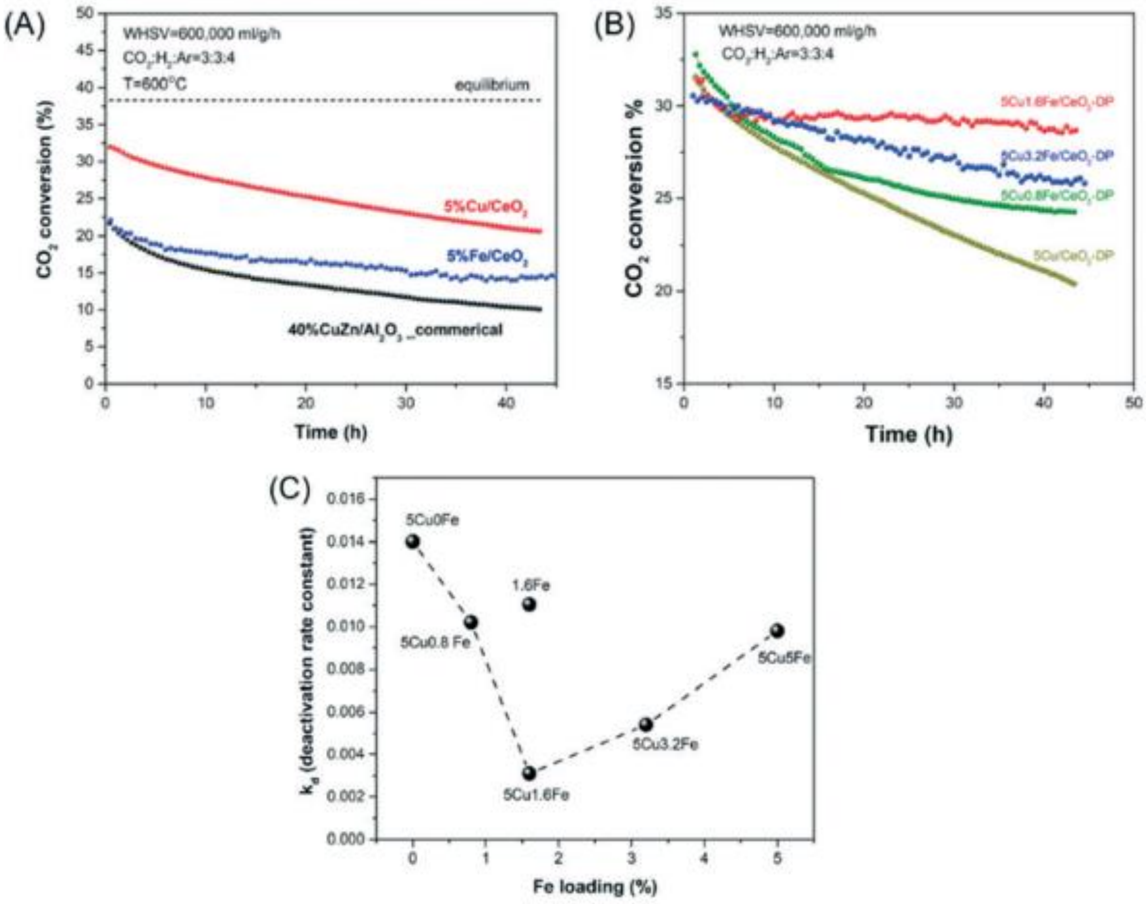

Fig. 2.24 Performace of (a) Cu or Fe doped ceria catalyst compared to commercial catalyst (b) different composition of Cu/FeO$_x$/CeO$_2$ catalyst and (c) deactiviation rate compared to Fe loading (Lin et al., 2019)

From Fig 2.24 above, it is shown that Cu/CeO$_2$ and commercial catalyst will begin to deactivate at a faster rate, while Fe/CeO$_2$ shows a better stability compared to the previous two catalyst, and a superior performance compared to commercial catalyst. Further test is comducted on different ratio of Cu/FeO$_x$/CeO$_2$ catalyst, which shows that 5Cu1.6Fe/CeO$_2$ catalyst has the best performance and stability, making it the optimal ratio for reverse water gas shift reaction. The crystallinity profile is shown in Fig 2.25.

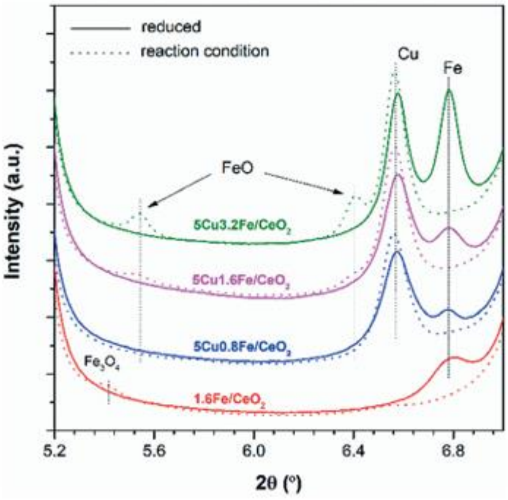

Fig. 2.25 XRD profile of reduced and used catalyst (Lin et al., 2019)

From the XRD profile it is shown that Fe will transform into FeO$_x$ once beinh subjected to reaction condition, while Cu will remain in its metallic form, concluding that these two are the active sites for revese water gas shift reaction. However, high Fe content will result in FeO aggregration which resulted in a lower performance as lower Fe content tends to have smaller FeO nano particle size that will promote the reaction (Lin et al., 2019). Lastly, the XPS of Cu and Fe is shown in Fig 2.26.

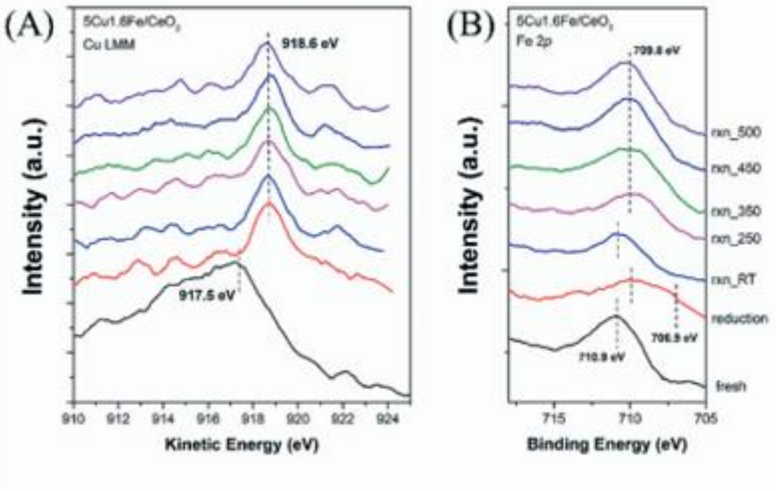

Fig. 2.26 The XPS profile of (a) Cu LMM and (b) Fe 2p (Lin et al., 2019)

The reduced catalyst shows a copper peak at 918.6 eV, a peak that indicates metallic copper. A used catalyst shows no shift in peak which confirms the XRD profile of Cu

doi:10.6342/NTU202403130

being the active site of the catalyst and is not oxidized in a reaction condition. Fe 2p XPS shows that the reduced sample contains Fe^0 (706.9 eV) and FeO (709.8 eV). After the catalyst undergoes reverse water gas shift, the catalyst is oxidized at room temperature as seen in the shift from Fe^0 to Fe^{3+}, while at elevated temperature Fe^{3+} undergoes reduction to FeO$_x$ that supports the XRD profile (Lin et al., 2019).

The last material that is used as a support for the catalyst material is a hexagonal boron nitride (hBN). Structurally, boron nitride has similarity with the structure of graphite but has the color white instead of black which is the reason boron nitride is more well known as white graphite (Jedrzejczak-Silicka et al., 2018). hBN is form from boron and nitrogen atoms alternating between each other in a hexagonal shape bonded by van der Waals force, akin to graphite where boron and nitrogen atoms are instead carbon atoms. The structure of hBN and graphite is seen in Fig 2.27.

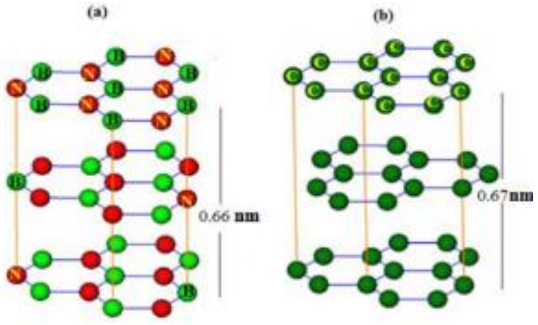

Fig. 2.27 Crsytal structure of (a) hBN and (b) graphite (Monajjemi, 2017)

There are several traits of hBN that could be adventagous as a catalyst support such as thermal stability and hydrophobicity (Jedrzejczak-Silicka et al., 2018). The usage of hBN as a catalyst support has been researched for VOC incienation using Pt based catalyst (Wu et al., 2001). By substituting γ-Al$_2$O$_3$ to hBN the stability of Pt catalyst is dramatically increase, exhibiting no deactivation for three cycles and no metal sintering is present due to the thermal stabily property of hBN up to 800^{o}C in air atmosphere (Wu et al., 2001) , as seen in Fig 2.28

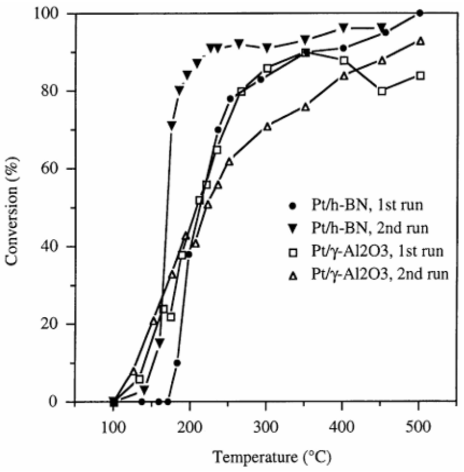

Fig. 2.28 Performance of Pt/ γ-Al_2O_3 and Pt/hBN for 2 cycles of reaction at 100-500 °C (Wu et al., 2001)

2.5 Hummers Method

While hBN has been shown to be a decent support for catalyst, one of the major disadvantages is the difficulty to disperse hBN in a liquid solution, such as water (Jedrzejczak-Silicka et al., 2018). As high dispersion is a crucial factor for a manufacture of fuctional macroscopic material, several methods has been studied to increase the dispersion of hBN. Exfoliation is generally a required to achieve the desired dispersion as the layered hBN structure will be reduced to a single layer sheet structure, easing the dispersion (Martínez-Jiménez et al., 2023). Several methods of exfoliation is compared in Fig 2.29.

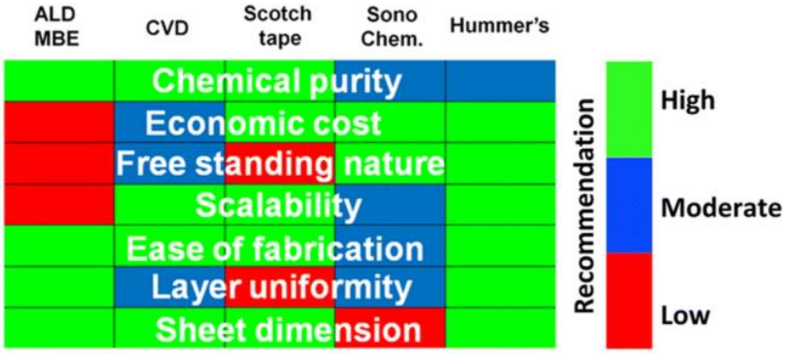

	ALD MBE	CVD	Scotch tape	Sono Chem.	Hummer's
Chemical purity	🟩	🟩	🟩	🟦	🟦
Economic cost	🟥	🟦	🟩	🟩	🟩
Free standing nature	🟥	🟦	🟥	🟩	🟩
Scalability	🟥	🟩	🟩	🟦	🟩
Ease of fabrication	🟩	🟩	🟩	🟦	🟩
Layer uniformity	🟩	🟦	🟥	🟦	🟩
Sheet dimension	🟩	🟩	🟩	🟥	🟩

Recommendation
🟩 High
🟦 Moderate
🟥 Low

Fig. 2.29 Comparison of various variables of hBN or graphane exfoliation (Sahu et al., 2021)

doi:10.6342/NTU202403130

As seen from the figure above, Hummer's method offers the most advantageous for hBN or graphane exfoliation. Hummer's method is first developed by William S. Hummer in the 1958 to produce graphite oxide as the predeccesing method, the Staudenmeier Hoffman-Hamdi method as said method is inefficient (requireding ten portions of $KClO_3$ for one portion of graphite) and prone to explosion (operating temperature above 98 ^{o}C) (Hummer and Offeman, 1958). In Hummer's method, one portion of graphite is mixed with concentrated sulfuric acid, sodium nitrate and three portions of $KMnO_4$ being operated at below 45 ^{o}C.

While it is safer than its predecessor, this process still produces NO_x gas that is toxic. An improved version of Hummer's method is proposed by eliminating the need to use $NaNO_3$ and uses 9:1 ratio of sulfuric acid and phosphoric acid (Marcano et al., 2010). The graphite oxide synthesized using the improved Hummer's method exhibits less defects in basal plane, more ozidized graphite, more organized structure and generally a high performance material. The Hummer's method has further been optimized to reduce the exfoliation duration from 12 hours to 3 hours and reagent used for the reaction by eliminating the need of phosphoric acid and the washing agents. A comparison of the improved Hummer's method and optimized Hummer's method is seen in Fig 2.30.

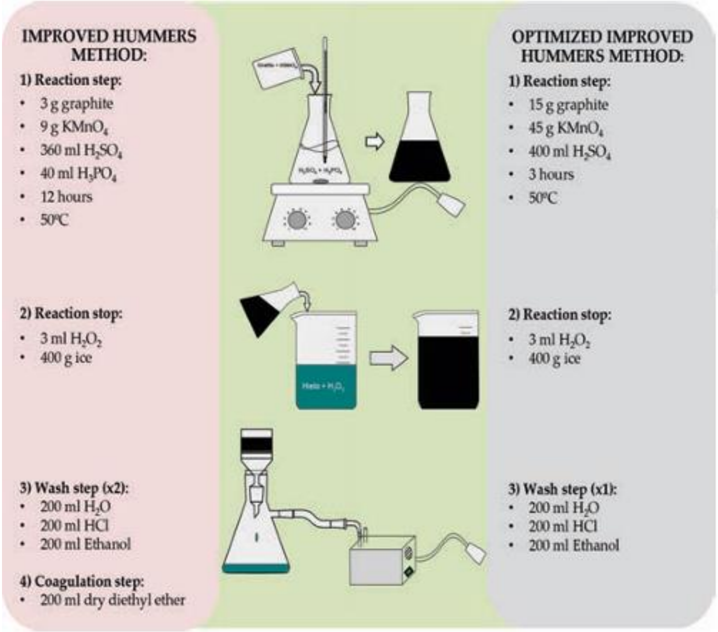

Fig. 2.30 Comparison of improved Hummer's method and optimized Hummer's method (López et al., 2016)

The result of these two procedures is compared in Table 2.7.

Table 2.7 Comparison of graphite and graphite oxide synthesized with improved Hummer's method and optimized Hummer's

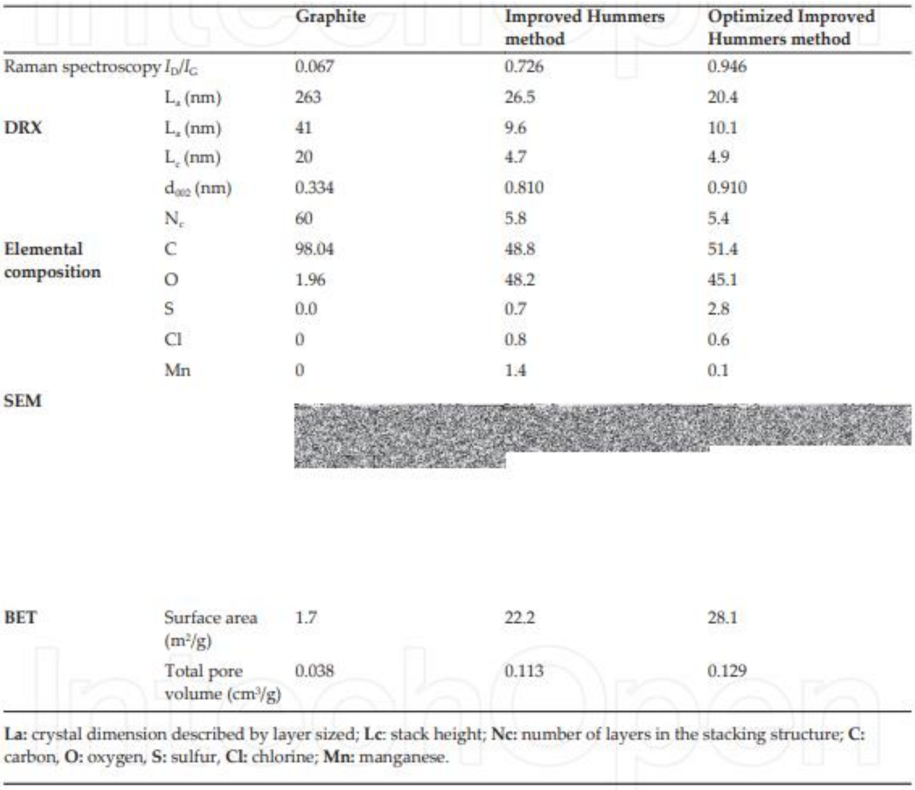

		Graphite	**Improved Hummers method**	**Optimized Improved Hummers method**
Raman spectroscopy	I_D/I_G	0.067	0.726	0.946
	L_a (nm)	263	26.5	20.4
DRX	L_a (nm)	41	9.6	10.1
	L_c (nm)	20	4.7	4.9
	d_{002} (nm)	0.334	0.810	0.910
	N_c	60	5.8	5.4
Elemental composition	C	98.04	48.8	51.4
	O	1.96	48.2	45.1
	S	0.0	0.7	2.8
	Cl	0	0.8	0.6
	Mn	0	1.4	0.1
SEM				
BET	Surface area (m^2/g)	1.7	22.2	28.1
	Total pore volume (cm^3/g)	0.038	0.113	0.129

La: crystal dimension described by layer sized; **Lc:** stack height; **Nc:** number of layers in the stacking structure; **C:** carbon, **O:** oxygen, **S:** sulfur, **Cl:** chlorine; **Mn:** manganese.

doi:10.6342/NTU202403130

The Raman spectroscopy result shows that the ratio of I_D/I_G (the ratio of d-band and g-band intesitiy) is increased considerably after reaction and the highest value is exhibited on the optimized improved Hummer's method, showing a greater structural disorder in the network and smaller sp^2 cluster. The crystal dimension also decrease significantly aligning with higher structural disorder along with fewer layered structure. Comparison of the the two Hummer's method shows a similar atomic ratio of C, O, S, Cl and Mn. Lastly, the BET result shows that the optimized Hummer's method exhibits a larger surface area with less reaction time and reagent. The reaction that occurs during Hummer's method is as follow.

1. $2\ H_2SO_{4\ (l)} + 2\ KMnO_{4\ (s)} \rightarrow Mn_2O_{7\ (aq)} + H_2O_{(l)} + 2\ KHSO_{4\ (aq)}$
2. $3\ Mn_2O_{7\ (aq)} \rightarrow 6\ MnO_{2\ (s)} + 3\ O_{2\ (g)} + O_{3\ (g)}$
3. $2\ Mn_2O_{7\ (aq)} + 2\ H_2O_{2\ (l)} + 4\ H_2SO_{4\ (l)} \rightarrow 4\ MnSO_{4\ (aq)} + 6\ H_2O_{\ (l)} + 2\ O_3 + 3\ O_2$
4. $MnO_{2\ (s)} + H_2SO_{4\ (l)} + H_2O_{2\ (l)} \rightarrow 2\ H_2O_{\ (l)} + MnSO_{4\ (aq)} + O_{2\ (g)}$

Reaction 1 occurs as soon as the $KMnO_4$ is added to the concentrated sulfuric acid, as the solution will turn green, indicating the presence of Mn_2O_7. Reaction 2 is the decomposition of Mn_2O_7 which usually occur at 35-45 ^oC (an explosion will occur at around 55 ^oC) (Brauer, 1965). Finally, the reaction is stopped using hydrogen peroxide to transform Mn_2O_7 and MnO_2 into $MnSO_4$, both reaction happens simultaneously (Chen et al., 2022). As Hummer's method will also cause the exfoliated material to have –OH bond, it will make the material slightly more miscible in water as such the hydrophobicity will be in between pure hBN and catalyst without hBN loading (Hu, 2023).

doi:10.6342/NTU202403130

CHAPTER III

EXPERIMENTAL PROCEDURE

3.1 Materials and Apparatus

3.1.1 Material for Catalyst Synthesis

Table 3.1 List of Material used for catalyst synthesis

Name	Supplier	Other Specification
$Cu(NO_3)_2.3H_2O$	Thermo Scientific	Purity: 99%
$Zn(NO_3)_2.6H_2O$	Sigma Aldrich	Purity: 98%
$ZrO(NO_3)_2.xH_2O$	Sigma Aldrich	Purity: 99%
$La(NO_3)_2.6H_2O$	Janssen Chimica	Purity: 98+ %
$Ce(NO_3)_3.6H_2O$	Thermo Scientific	Purity: 99.5%
$NaWO_4.2H_2O$	Alfa Aesar	Purity: 99%
$NaMoO_4.2H_2O$	Alfa Aesar	Purity: 98%
Na_2CO_3	Fisher Scientfic	Purity: 99.5%
hBN	U-Materials	
H_2SO_4	Honeywell	95-97%
NaOH	Honeywell	100%
H_2O_2	Honeywell	30%
$KMnO_4$	Thermo Scientific	
$Fe(NO_3)_3.9H_2O$	JT Baker	98%
DI water	-	-
Ice	-	-
pH 4.01 buffer solution	Rocker Scientific	Composition: $C_8H_5KO_4$

doi:10.6342/NTU202403130

Tabel 3.1 List of Material used for catalyst synthesis (cont.)

Name	Supplier	Other Specification
pH 7 buffer solution	Rocker Scientific	Composition: KH_2PO_4,Na_2HPO_4
pH 10.01 buffer solution	Rocker Scientific	Composition: $NaHCO_3$
Copper based methanol synthesis catalyst	Alfa Aesar	Pellets: 5.4 mm × 3.6 mm

3.1.2 Apparatus for catalyst synthesis

Table 3.2 List of apparatus used for catalyst synthesis

Name	Supplier	Other Specification
Beaker glasses	TOF, Yeasten	Volume: 50 mL, 100 mL, 150 mL, 250 mL, 500 mL, 1000 mL
Magnetic stirrer with heater	DLAB	Model: 8030106110 MS-H-Pro+
Thermocouple	DLAB	Type K
Centrifuge	Hermle LabortechIK	Model: Z206A
pH paper	ADVANTEC	pH range: 0-14
pH meter	Jenco Instrument	Model: 6173
pH electrode	Jenco Instrument	Model:GB-700
Vacuum filtration system	Synthware	Includes glass funnel, clamp, and joint flask
Filter paper	Whatman	Pore size: 11 µm, Diameter: 47 mm

Table 3.2 List of apparatus used for catalyst synthesis (cont.)

Name	Supplier	Other Specification
Aspirator	Newlab Instrument	Model: AS-3
Oven	Deng Yang Instruments	Model: DH400
Pestle and mortar	BIPEE	4.65 × 3.9 × 1.42 inch
Muffle oven	Kindleuro Company	-

3.1.3 Apparatus for Gas Calibration and Analysis

Table 3.3 List of apparatus for gas calibration and analysis

Name	Supplier	Other Specification
Volumetric flask	LMS	Volume: 100 mL
Micro pipette	AHN biotechnologie	Model: pipet4u pro 1000 µL
Gas syringe	Trajan Scientific	Volume: 1 mL
Liquid syringe	Agilent	Volume: 10 µL
Gas chromatography	Agilent	Model: 8860GC system Column: Porapak Q 80/100 2m

3.1.4 Apparatus for Catalytic Test

Table 3.4 List of apparatus for catalytic test

Name	Supplier	Other Specification
Metal reactor	-	Quantity: 3 Material: Stainless Steel 316 Length: 30 cm, Diameter: 0.5 inch
Furnace	Kindleuro	Quantity: 2
Quartz wool	-	-
Heating tape	Omega	Model: STH051-060, Quantity: 2
Thermocouple	Kindleuro	Quantity: 2, Type K
Temperature contorller	Macro Fortunate	Quantity:2, Model: TC-10A
Mass flow controller	Brooks Instrument	Model: 5850 series H_2: 100 sccm, CO_2: 100 sccm, N_2: 1000 sccm
Molecular sieve 3A	Alfa Aeser	1-2 mm bead
$CaCl_2$	JT Baker	Purity: 96%

3.1.5 Gas Used

Table 3.5 List of gas used

Name	Supplier	Other Specification
Hydrogen	Fung Ming Gas	-
Air	Fung Ming Gas	-
Nitrogen	Fung Ming Gas	Purity: 99.9995%
Helium	Fung Ming Gas	Purity: 99.9995%
Carbon Dioxide	San Fu Gas	Purity: 99.9995%
Carbon Monoxide	Fung Ming Gas	Purity: 99.9995%
Carbon Monoxide	San Fu Gas	Purity: 3000 ppm/He

3.1.6 Analysis Instrument

Table 3.6 List of analysis instrument used

Analysis	Supplier	Other Specification
XRD	SmartLab	Model: Rigalu SmartLab SE
SEM	FEI Company	Model: Nova NanoSEM 230
BET	Micromeritics	Model: ASAP2020
FTIR	Perkin Elmer	Model: Spectrum 100
XPS	Thermo Scientific	Theta Probe

3.2 Experimental Setup

The experimental setup that is used for catalytic test is shown in Fig 3.1. For the one reactor system, the inlet gas will enter mass flow controller to regulate the flow rate before entering the reactor. Reactor is heated with a furnace to ensure the optimal operating temperature. A pressure gauge is located near the outlet of the reactor to adjust the pressure of the system, which is controlled using a needle valve. The outlet gas is then flowed outdoors or to a gas chromatography machine to measure the concentration of outlet gas. The experimental setup for the two reactor system is overall similar to the single reactor system with the exception of using multiple reactors. The first reactor will undergo reverse water gas shift reaction with high temperature followed by water adsorbtion midway before entering the second reactor with lower operating temperature than the first reactor. The pressure is controlled with a back pressure valve to enable a higher operating pressure for the system.

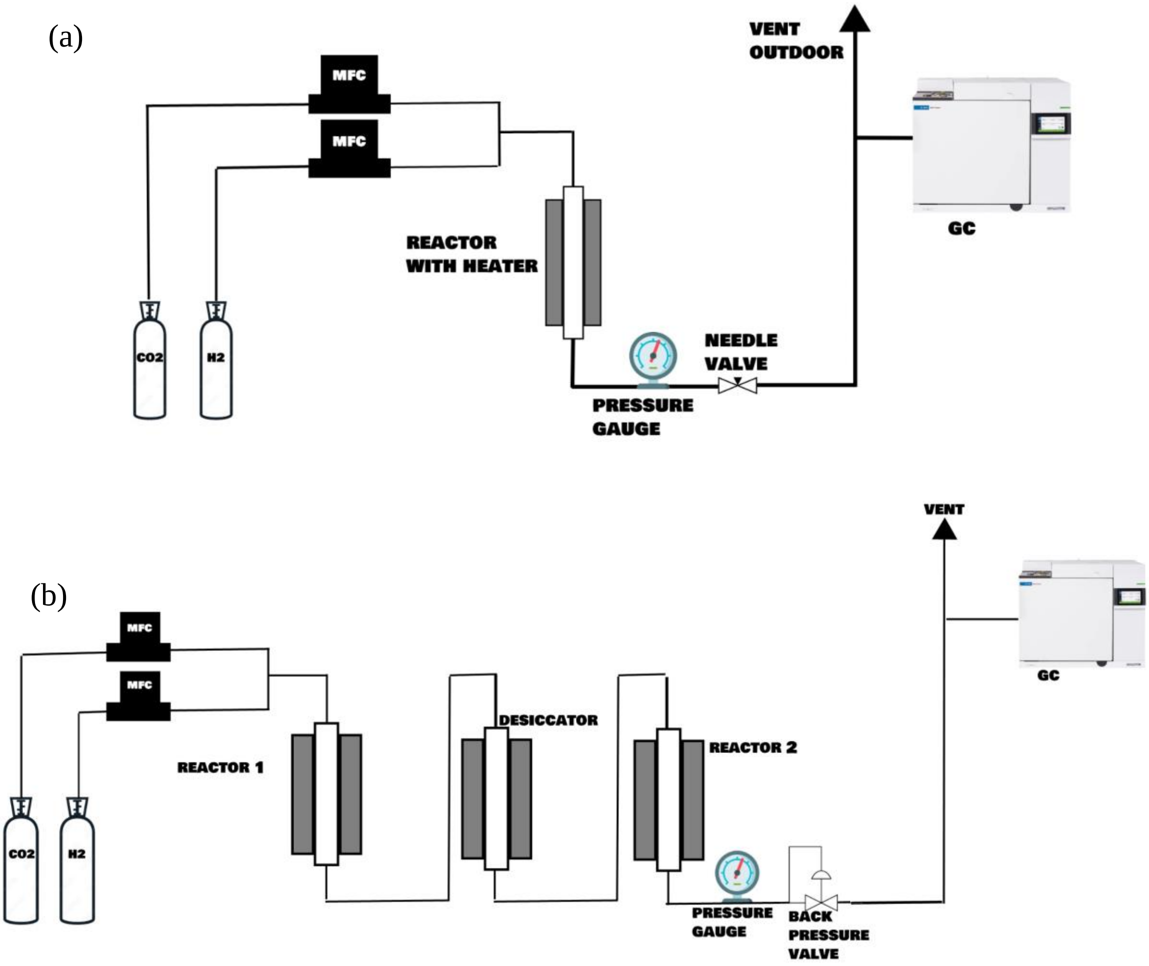

Fig. 3.1 Experimental setup for the (a) single reactor system and (b) two reactor system

3.3 Experimental Procedure

3.3.1 Improved Modified Hummers Method Procedure

The flowchart of the improved modified Hummer’s method is illustrated at Fig 3.2. The improved modified hummer’s method is used to exfoliate the hBN to make it more miscible in water for catalyst synthesis. First, around 1 g of hBN is mixed with 60 mL of concentrated H_2SO_4 inside a beaker. Next, around 3 g of $KMnO_4$ is poured inside the solution and heated at 40^oC for 6 hours. After 6 hours the solution is then tranfered to an ice bath and around 100 mL of 30% H_2O_2 is poured into the solution. To filter the solution, initially centrifugation is used at 2000 rpm for 25 minutes to remove excess liquid before being neutralized with NaOH until the solution’s pH reach 7. The neutralized sample is then filtered using vacuum filtration and wash with DI water around 5 times. Lastly, the sample is dried in a 60^oC oven at least overnight.

doi:10.6342/NTU202403130

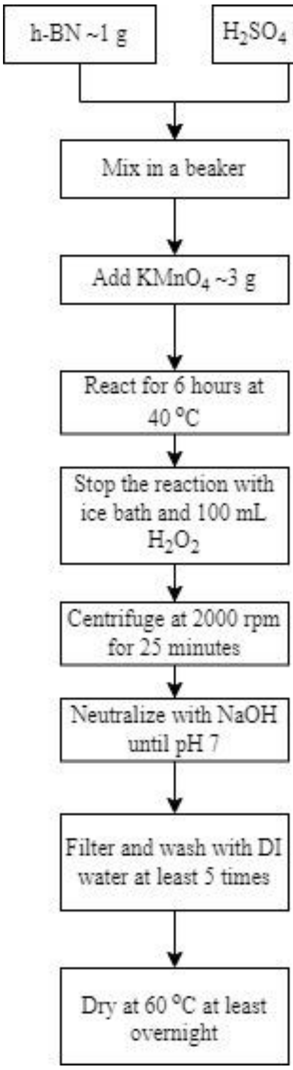

Fig. 3.2 Expertimental procedure for exfoliation of hBN by Improved Modified Hummers method

3.3.2 Catalyst Synthesis Method (without Fe)

The catalyst synthesis method for non-Fe catalyst is shown in Fig 3.3. To synthesize the catalyst, coprecipitation is used. First, hBN that has been exfoliated is mixed with metal salt in accordance to the desired ratio of the metal in 100 mL of DI water and stirred overnight. Next, the salt and hBN mixture is precipitated with Na_2CO_3 until the pH reachs 7. The sample is then aged for 2 hours at 65°C before being filtered and washed with DI water around 5 times. The filtered sample is then dried at a 60°C oven overnight before being calcined at 400°C for 4 hours with a ramping rate of 2°C/min.

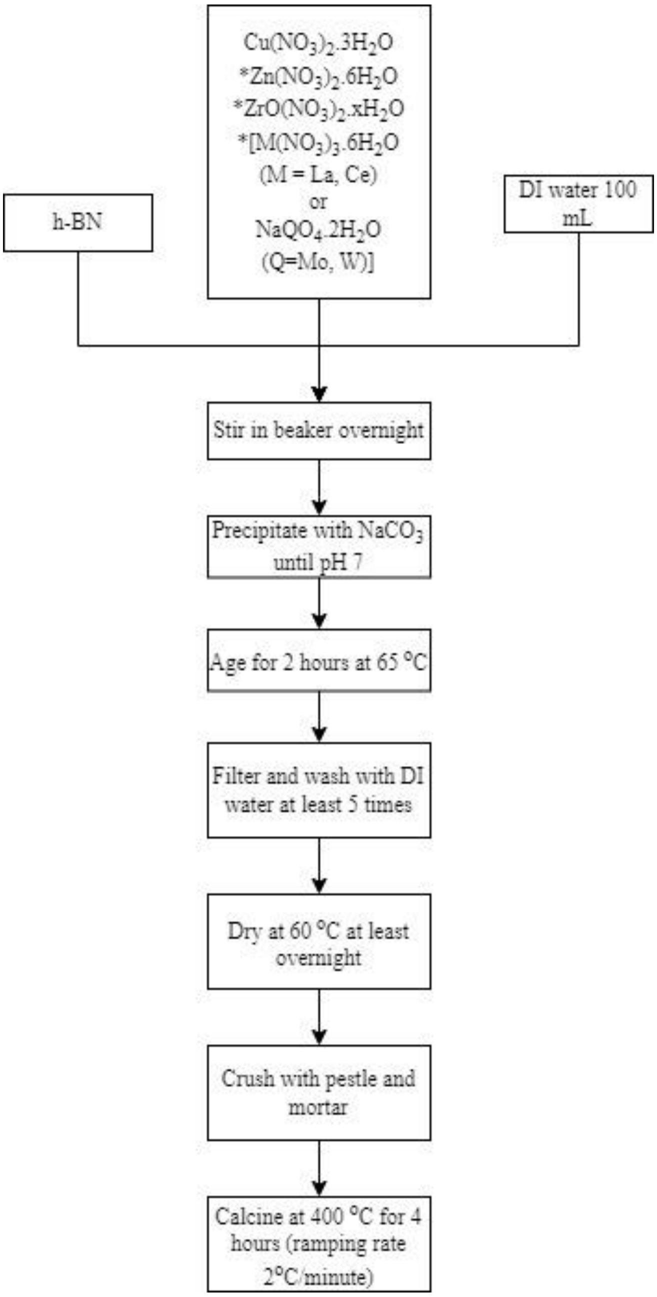

Fig. 3.3 Experimental procedure of catalyst synthesis method (without Fe)

Note:

1. The ratio of metal is Cu : Zn : Zr :M or Q = 6 : 3 : (1-y) : y; [M = La, Ce; Q = Mo, W] with the value of y is 0 or 0.25. The catalyst naming is (XX)CZZ(M or Q)(_hBN) with XX denoting the amount of metal loading.
2. For Cu/Ce catalyst the ratio is 1:3 with the naming system of (40)CC(_hBN)
3. *denotes optional (depends on the catalyst is synthesized)

3.3.3 Catalyst Synthesis Method (with Fe)

Fig 3.4 shows the synthesize method for catalyst with Fe is similar to the synthesis method for catalyst without Fe with 2 major differences. Firstly, instead of pH 7, the catalyst is coprecipitated at pH 9. Second, the calcination condition differs with the iron based catalyst being calcined at 700°C for 4 hours at ramping rate of 10°C/min. The catalyst naming is (40)CFC(_hBN).

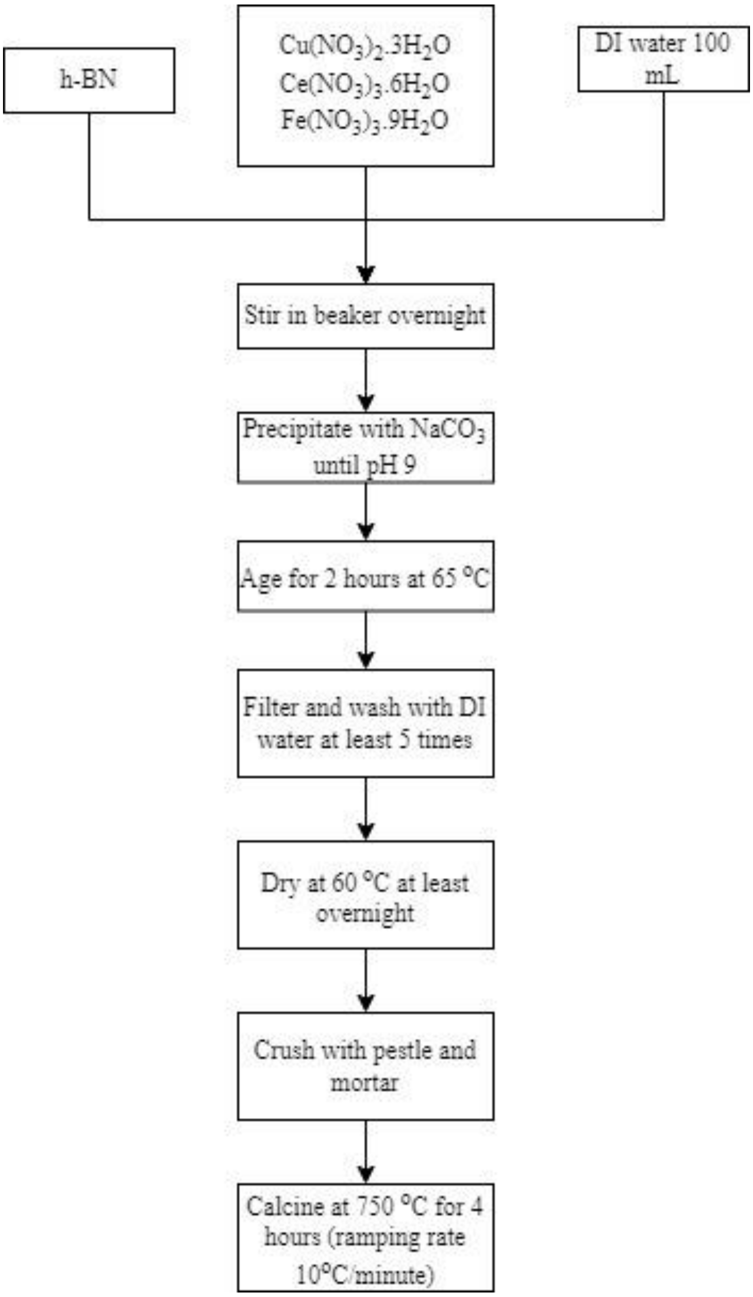

Fig. 3.4 Experimental procedure of catalyst synthesis method (with Fe)

3.3.4 Catalytic Performance Evaluation (CO_2 hydrogenation to Methanol)

Fig 3.5 shows the flowchart of catalytic performance evaluation CO_2 hydrogenation to methanol. Initially inert quartz is inserted inside a stainless steel tube reactor before being filled with 0.5 g of catalyst and additional inert quartz to act as a buffer to ensure the catalyst stays in place during reaction. The sample is the reduced with pure H_2 gas at 350^{o}C for 1 hour. The catalytic activity is then tested at 230^{o}C at 1 bar for 1 hour and raised the pressure at 10 bar and tested for 2 hours.

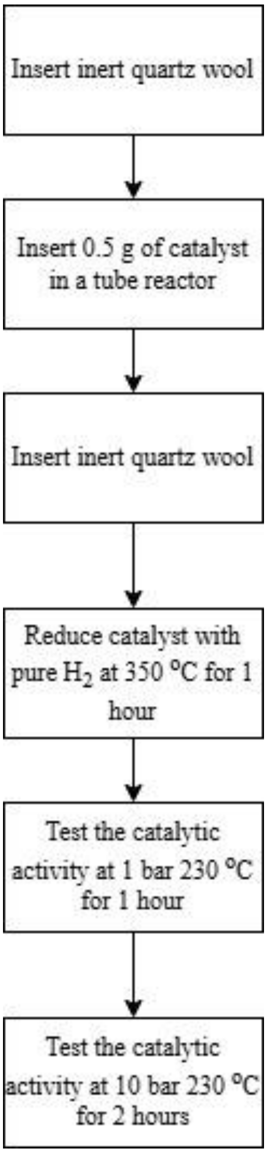

Fig. 3.5 Experimental procedure of CO_2 hydrogenation to methanol test

Note: The flow rate used is 100 sccm with a flow ratio of CO_2/H_2 1:4

3.3.5 Catalytic Performance Evaluation (CO hydrogenation to Methanol)

Fig 3.6 shows the schematic prodecure of CO hydrogenation to methanol catalytic performance evaluation. Similar to CO_2 hydrogenation, the overall process for CO hydrogenation to methanol has the same procedure for the catalyst loading, reduction and catalytic testing. The only difference is the flow rate of the gas used (CO_2 hydrogenation is done with 20 sccm of CO_2 and 80 sccm of H_2 while CO hydrogenation is done with 25 sccm of CO and 75 sccm of H_2).

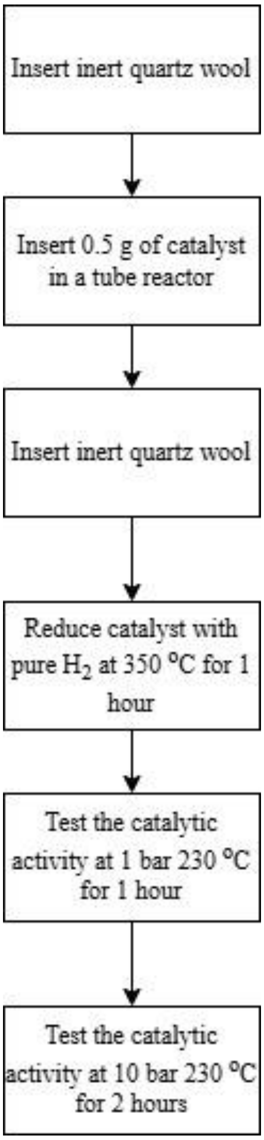

Fig. 3.6 Experimental procedure of CO hydrogenation to methanol test

Note: The flow rate used is 100 sccm with a flow ratio of CO/H_2 1:3

3.3.6 Catalytic Performance Evaluation (Reverse Water Gas Shift Reaction)

Fig 3.7 shows the schematic prodecure of reverse water gas shift (RWGS) catalytic performance evaluation. The RWGS reaction's catalytic test procedure is similar to CO_2 hydrogenation and CO hydrogenation with the key difference being the condition of the catalytic test. As RWGS is an endothermic reaction that is not affected by pressure, the catalytic activity testing is done at 350^{o}C and 1 bar for 2 hours. The flow rate is kept similar with CO_2 hydrogenation

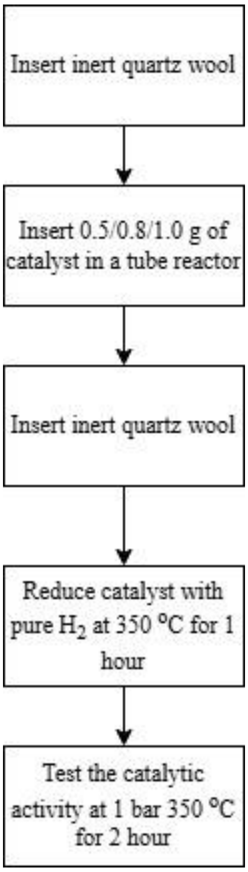

Fig. 3.7 Experimental procedure of Reverse Water Gas Shift reaction

Note: The flow rate used is 100 sccm with a flow ratio of CO_2/H_2 1:4

3.3.7 Catalytic Performance Evaluation (CAMERE Reaction)

Fig 3.8 shows the catalytic performance evaluation of 1 reactor CAMERE reaction. The CAMERE reaction will first be tested with one reactor (with a condition mimicking the second reactor of the two reactior system) to test the catalyst loading and type for the second reactor in the two reactors system. After the catalyst is loaded and reduced with H_2, the catalyst is tested in methanol synthesis condition (230°C and 10 bar).

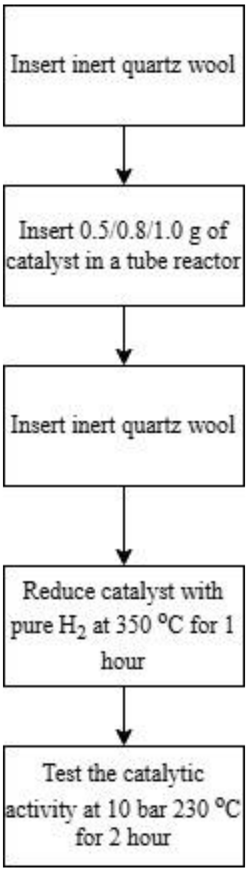

Fig. 3.8 Experimental procedure of CAMERE Reaction (1 reactor)

Note: The flow rate used is 106 sccm with a flow ratio of $CO/CO_2/H_2$ 16:10/80. This ratio of gas is used to simulate the condition of the second reactor where the CO_2 conversion after RWGS reaches 50%. The flow of CO is higher compared to CO_2 is due to a malfunction of the mass flow controller for CO as operating it below 16 sccm will cause the gas to not flow.

Fig 3.9 showed catalytic performance evaluation of CAMERE reaction. The reaction is done with two system reactor with a dessicant for water removal midway. For the 1st reactor, 0.5g of catalyst is loaded and reduced with H_2 at 350°C while the second reactor is loaded with 0.8 g of catalyst with same reduction condition. The dessicator is loaded with 5g of dessicant and kept at room temperature throughout the entire catalytic test.

doi:10.6342/NTU202403130

After the reduction process, the first reactor's temperature is raised to 500^{o}C and the second reactor's temperature is reduced to 230^{o}C. All the reaction is tested at elevated pressure (10 bar and 30 bar) for 2 hours.

Fig. 3.9 Experimental procedure of CAMERE Reaction (2 reactor)

Note: The flow rate used is 100 sccm with a flow ratio of CO_2/H_2 is 20/80

(*) marks additional testing step that is conducted if required

Lastly, Fig 3.10 shows the flowchart of the reactor in series catalytic performance test. The process is similar to the CAMERE reaction with the exception of the temperature of the first reactor which is 230 ^{o}C instead of 500 ^{o}C.

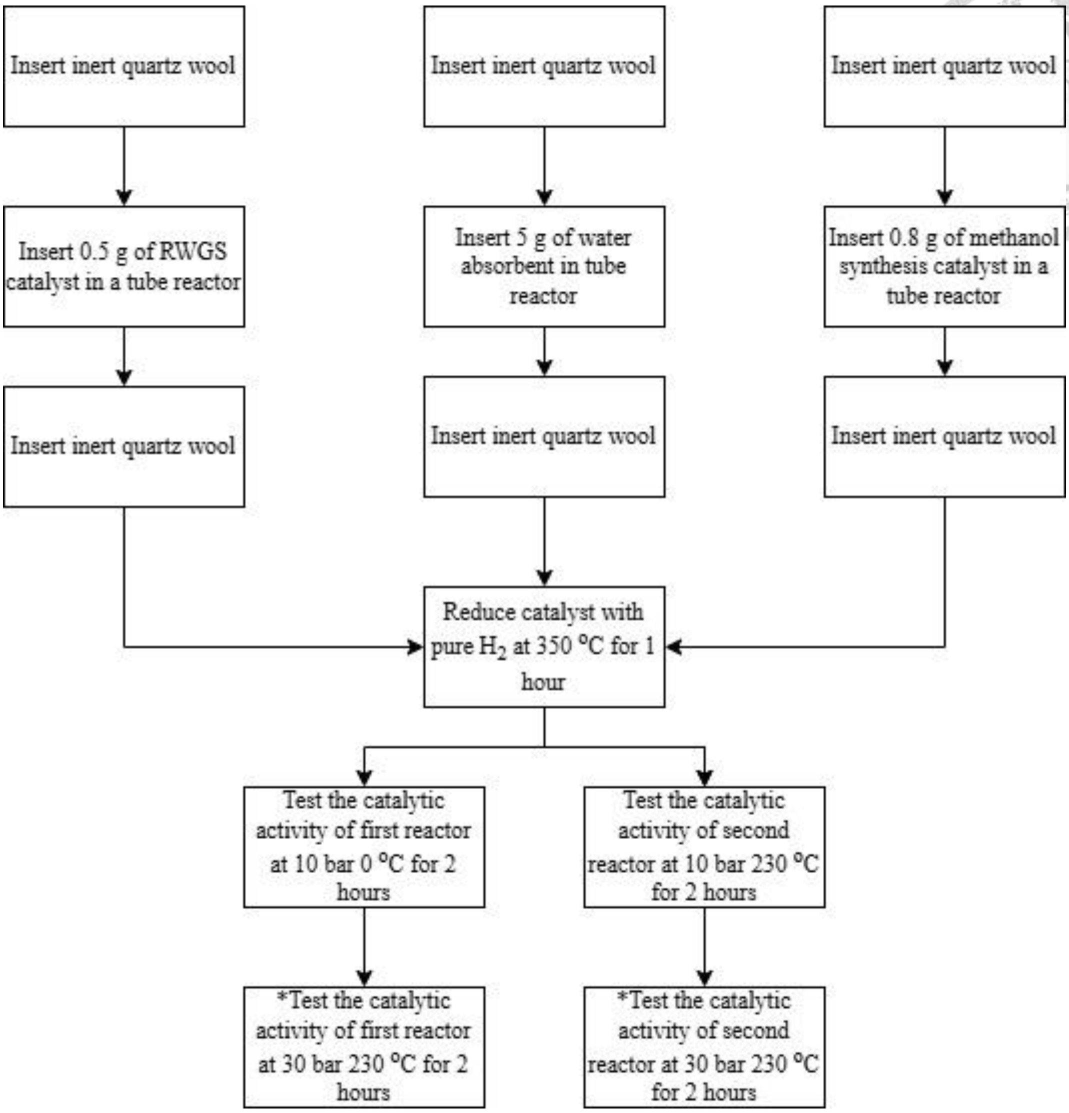

Fig. 3.10 Experimental procedure CO_2 hydrogenation the methanol with 2 reactor in series

Note: The flow rate used is 100 sccm with a flow ratio of CO_2/H_2 is 20/80

(*) marks additional testing step that is conducted if required

3.4 Catalyst Characteristic Analysis

3.4.1 XRD

XRD schematic figure is presented in Fig 3.11. XRD (X-ray Diffraction) is an analysis method that can be utilized to identify a specific materials, specifically the crystalline structures that is present inside. Constructive diffraction of X-ray is expelled, which will make contact with the surface of the sample. This X-ray wave will eventually came into contact with the electrons from the sample’s crystal, resuting in a characteristic X-ray spectrum, which will then be detected by a detector and converted to the concentration of a sample’s constituent components (Bunaciu, 2015).

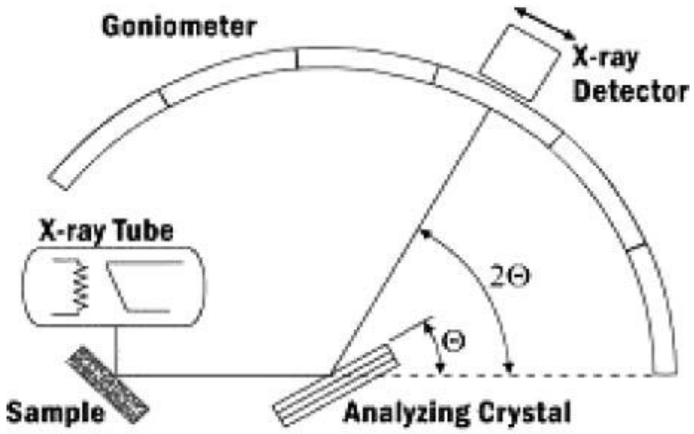

Fig. 3.11 Schematic figure of XRD apparatus (Bunaciu, 2015)

Rigaku Smartlab SE is used for XRD analysis. The X-ray source comes from Cu K α with the wavelength of 1.5148 Å, operating voltage of 20 kV and operating current of 20 mA. The sample of around 0.5g is first prepared on a quartz plate and pressed it as flat as possible, The sample is analysed at the range of $2\theta=10^o-80^o$ with 0.01^o scan step and 20^o/minute for overall scan and $2\theta=25^o-30^o$ with 0.01^o scan step and 1^o/min scan rate.

3.4.2 FTIR

FTIR schematic figure is shown in Fig 3.12. FTIR (Fourier Transform Infrared) is an analysis method that is utilized to observe the functional group that is present in a material surface using infrared radiation. The functional group is observed by measuring the amount of infrared radiation absorbed by the functional bond that is present in a material at a certain wavelength. To ensure the analysis of functional group is possible, the molecule must be IR active (has dipole moment) where the IR radiation will interact with covalent bond presents in the material and oscilate the bonds which will cause a shift in dipole moment. Different bond will have a absortion at a different IR frequency as every bond has a specific natural vibration frequency that will not be affected by other bonds (Khan et al., 2018).

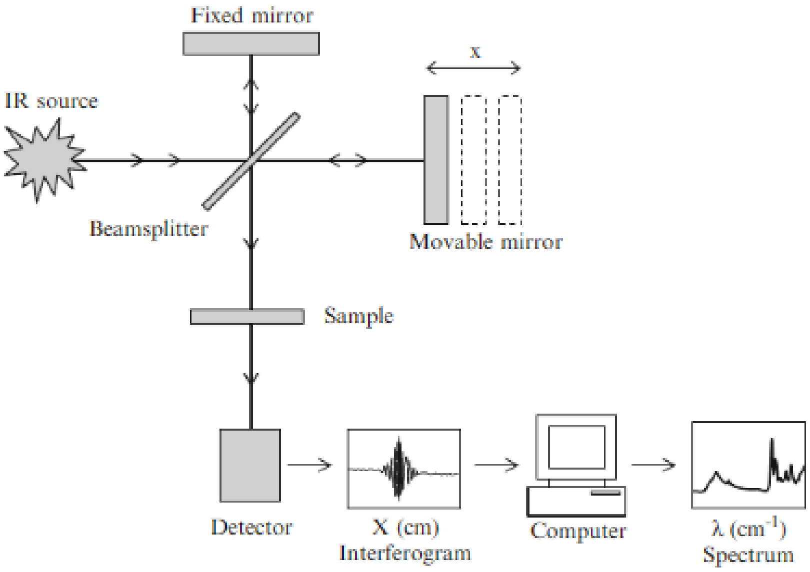

Fig. 3.12 Scematic diagram of FTIR (Ojeda and Dittrich, 2012)

The FTIR is tested using The Spectrum 100 model from Perkin Elmer. The sample is being prepared by using 2 mg of sample mixed with 200 mg of KBr and around 50% of the sample is being pressed as a pellet before being tested in the machine. The sample is tested at the wavelength range of 450-4000 cm^{-1}.

3.4.3 SEM

A scematic diagram of SEM is presented in Fig 3.13. SEM (Scanning Electron Microscope) is an analysis method that can be utilized to observe the microscopic structure of a sample, with a higher magnification compared to conventional microscope. SEM uses high energy (approximately 10^6 e^-V) electron beam, which is then aimed on a speciment’s surface with lens to enhance the sample’s surface morfology. The signal of interaction between the sample surface and electron fired is then detected with a detector close to the sample. This signal can then be viewed in a display screen attacted to the microscope/computer (Mohammed, 2019). Prior to testing, around 2 mg of sample is attacted to a carbon tape coated with platinum particle at vacuum condition for around 10 minutes. The SEM utilized 5kV electron beam energy at a working distance of 8 mm.

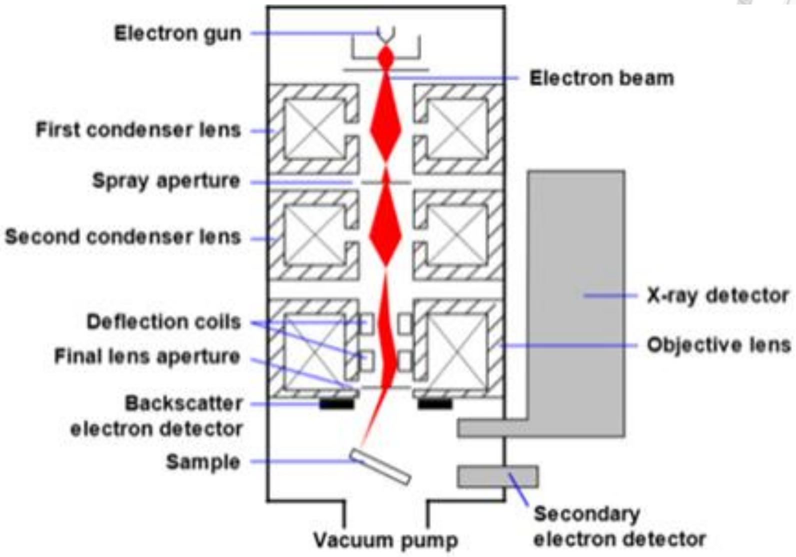

Fig. 3.13 Schemactic figure of SEM apperatus (Abdullah & Muhammed, 2019)

3.4.4 EDS

An early schematic figure is EDS is shown in Fig 3.14. EDS (Energy Dispersive X-Ray Spectroscopy) is an analysis method than can be utilized to identify element composition that is present in a specimen. EDS is commonly paired with SEM as the working principal is similar, where electron is ejected and the signal of the emitted electron and sample surface will be detected and displayed for analysis. The major difference is a detector that is responsible divide different chemical element’s x-ray characteristic into energy spectrums, enabling EDS to quantify and quantify the constitiuent of the sample. As EDS is attacted to SEM, the sample preparation method is similar to the sample preparation of SEM as stated in chapter 3.3.3.

doi:10.6342/NTU202403130

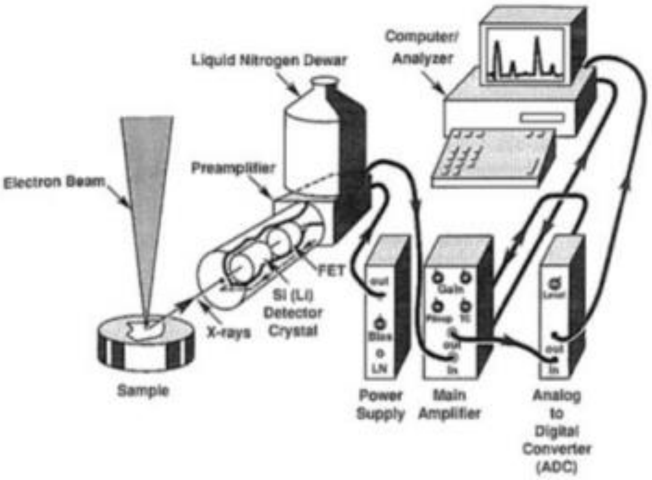

Fig. 3.14 Schematic figure of EDS apparatus (Goldstein, 2003)

3.4.5 BET

The BET (Brunauer–Emmett–Teller) method is a method commonly employed to measure a porous sample’s surface area. This method is first published by Stephen Brunauer, Paul Hugh Emmett, and Edward Teller in 1938, where physioadsorption of gas on a multilayer solid surface. The measurement of surface area is being conducted using an inert gas (i.e nitrogen) with specific pressure that will fill the pores within the speciment. Nitrogen gas is injected into the sample until every single pores is filled, where the surface area of a sample is proporsional to the amount of gas adsorbed. The equation used for BET has its basis from Langmuir isotherms adsorption where the eqaution used are as follow (Galarneu, et al., 2018) :

$$\frac{1}{\mathrm{v}[\left(\frac{\mathrm{p_0}}{\mathrm{p}}\right)-1]}=\frac{\mathrm{c}-1}{\mathrm{v_m c}}\left(\frac{\mathrm{p}}{\mathrm{p_0}}\right)+\frac{1}{\mathrm{v_m c}} \tag{1}$$

$$\mathrm{S_{total}}=\frac{\mathrm{v_m Ns}}{\mathrm{V}} \tag{2}$$

$$\mathrm{S_{BET}}=\frac{\mathrm{S_{total}}}{\mathrm{m_{adsorbent}}} \tag{3}$$

A schematic diagram of the BET method is presented at Fig 3.15.

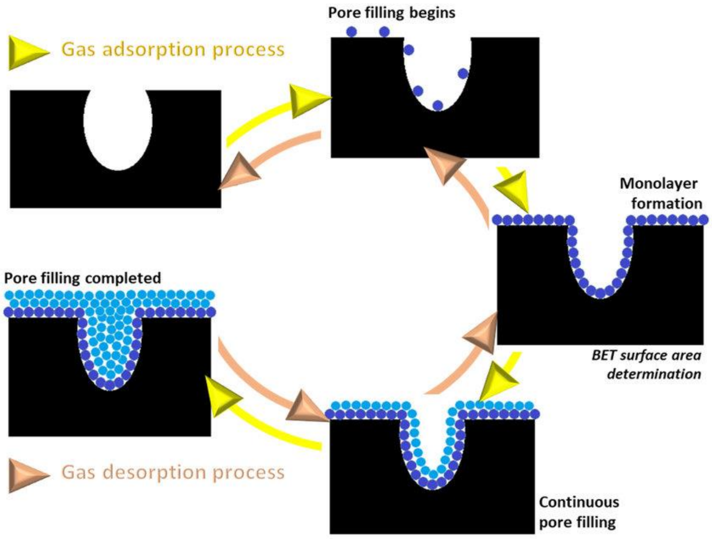

Fig. 3.15 Schematic diagram of BET method (Mohtar, et al., 2021)

The BET sample powder is delived to the staff of the instrument with a degas condition of 100^{o}C to remove the water vapor from the sample.

3.4.6 GC

The schematic diagram of GC is presented in Fig 3.16. GC (Gas chromatography) is an analytical method that is commonly used to quantify and qualify volatile compound in gas phase. To analyse, first, the sample gas is injected at the head of the column with a specific volume. The column of a GC also employs carrier gases, inert gases such as nitrogen, helium, and argon, which serves to carry sample within the colomn. The samples will then be separated into the constituent compound, which is done by the separation column and column oven. Lastly, detectors such as TCD (Thermal Conductivity Detecter), which is used to analyse lighther compounds such as water, air, hydrogen, carbon monoxide, and FID (Flame Ionization Detector), which is used to detect organic compounds such as alcohol (Kitson, et al., 1996), inside a GC will quantify the gas sample as it is removed along with the carrier gas (Kaur and Sharm, 2018).

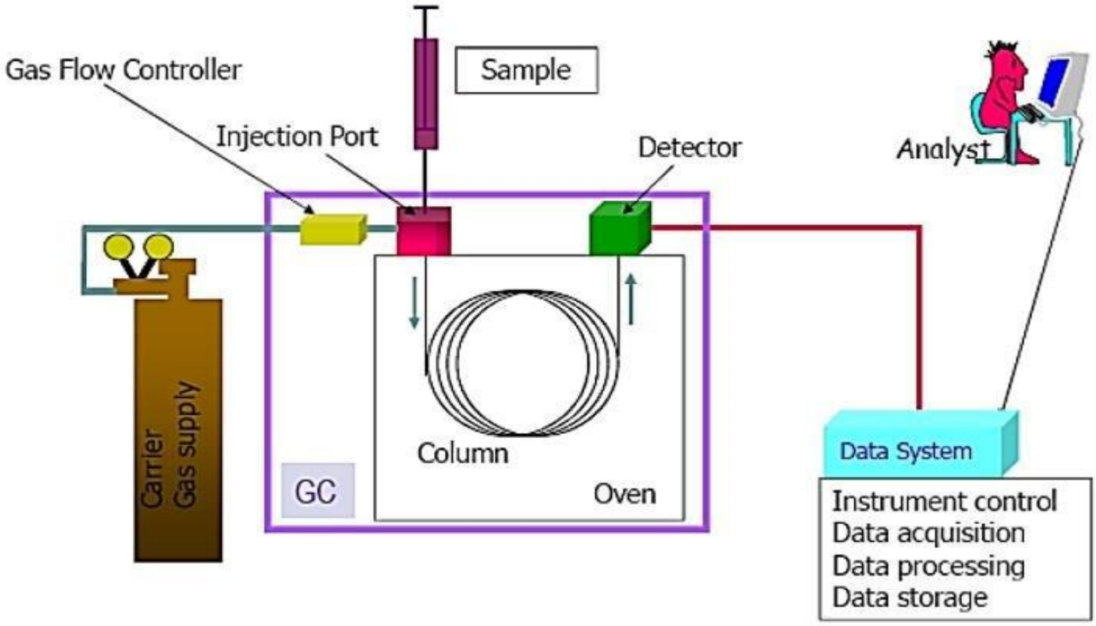

Fig. 3.16 Schematic diagram of GC (Obeidat, 2021)

The GC equipment is Agilent 8860 with two types of detector, TCD (for measuring H_2, CO and CO_2) and FID (for measuring methanol). The sample is injected to the GC at the TCD and FID detector with a retention time of 6 minutes and 3 minutes of post treatment. For the catalyst reduction process, the sample injection is done at the 10 minute and 1 hour mark while the catalytic outlet gas analysis is done every 30 minutes.

The specification for TCD column is as follow:

1. Carrier gas: He (99.9995%)
2. Column flow: 20 mL/min
3. Reference flow: 30 mL/min
4. He makeup flow: 2 mL/min
5. Packed column: Porapok Q80/100 2 m
6. Injection temperature: 150^{o}C
7. TCD temperature: 140^{o}C
8. Oven program: keep at 40^{o}C for 1 minute, heat from 40^{o}C to 200^{o}C with a ramping rate of 40^{o}/min, keep at 200^{o}C

9. TCD electric voltage: 25 µV

The specification for FID column is as follow:

1. Carrier gas: He (99.9995%)
2. Column flow: 2.6 mL/min
3. Air flow: 400 mL/min
4. H_2 flow: 30 mL/min
5. N_2 makeup flow: 25 mL/min
6. Packed column: HP-Innowax 19091N-1131
7. Injection temperature: 220^{o}C
8. FID temperature: 250^{o}C
9. Oven program: keep at 40^{o}C for 1 minute, heat from 40^{o}C to 200^{o}C with a ramping rate of 40^o/min, keep at 200^{o}C
10. High pressure six-ways valve: G3527A Pneumatic Control Module, Agilent Technologies

3.4.7 XPS

A schematic diagram of XPS is presented in Fig 3.17. XPS (X-ray Photoelectron Spectoscopy) is an analytical method used to observ the chemical state of components in the surface area of a material. As surface analysis is a crucial factor for many aspect of such as adsorption, corrosion, and adhesion as these factors depends on the interaction of surface components (Krishna & Philip, 2022). The surfave defect as the surface is broken periodically into one dimension that will lead to structural, electronic state and valance change will assist the understanding of surface characteristic. Furthermore, the number of atoms in the surface is far fewer compared to the bulk, which makes it highly reactive chemically.

doi:10.6342/NTU202403130

The analysis of XPS has been utilized in corrosion, catalyst, nanomaterial and electronics. Several parameters that can be tested using XPS are chemical composition, surface functionalization, adsorbate, layer thickness and particle size of nanomaterial (Krishna & Philip, 2022). The analyte is observed using X-rays and the energy level from the surface materials is recorded from the photo electrons ejected, measuring the kinerics energy. The sample is delivered to the instrument staff for analysis.

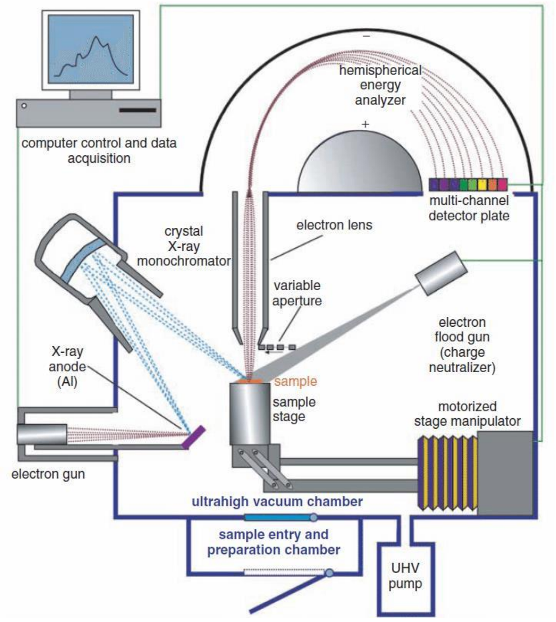

Fig. 3.17 Schematic diagram of XPS (Sowinska et al., 2014)

3.4.8 H_2-TPR and CO_2-TPD

H_2-TPR (Temperature Programmed Reduction) and CO_2-TPD (Temperature Programmed Desorption) are methods that is used to observe the behavior of catalyst with a certain gas. Fig 3.18 shows a schematic diagram of H_2-TPR. In H_2-TPR, the catalyst is flowed with a mixture of H_2 and Ar under linear heating rate to observe the reducibility of the catalyst under hydrogen condition (Zhu et al., 2020). Fig 3.19 shows a schematic diagram of CO_2-TPD. In principal, a small amount of catalyst is flowed with inert gas (usually He or Ar) before being switched with the reaction gas and heated with a linear heating rate (Ishii & Kyotani, 2016). For CO_2-TPD, the sample is initially flowed with heated He (typically ranges from 400°C to 800°C) gas carrier and cooled down (around 50°C) before being switched to CO_2 at linearly increased heating rate. CO_2-TPD is commonly used to analyse the basicity of a catalyst by observing the adsorption behavior of the material (Kelpel & Hunger, 2005).

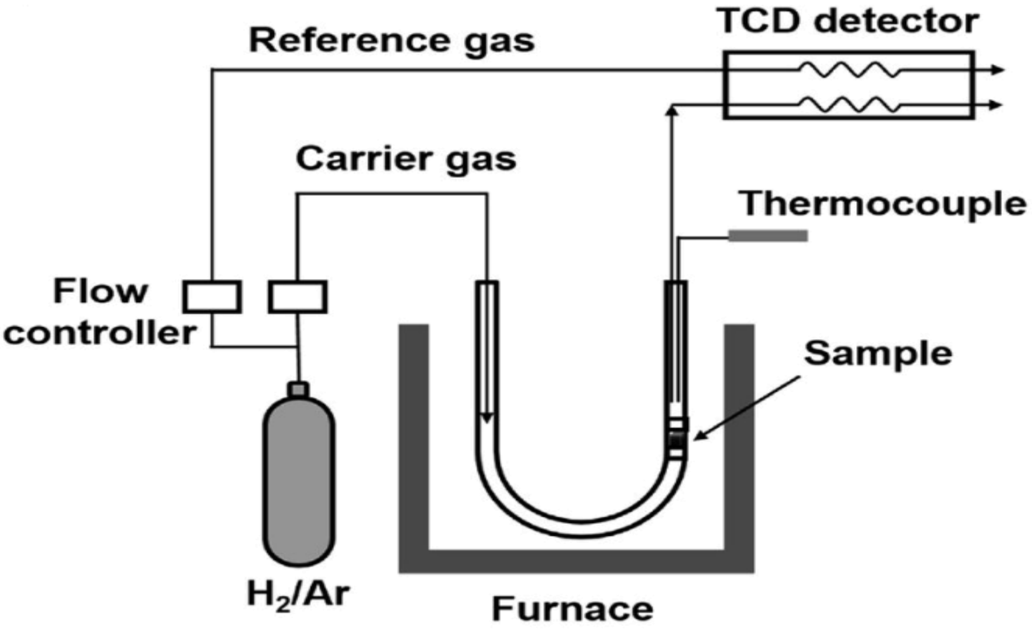

Fig. 3.18 Schematic diagram of H_2-TPR (Liu et al., 2016)

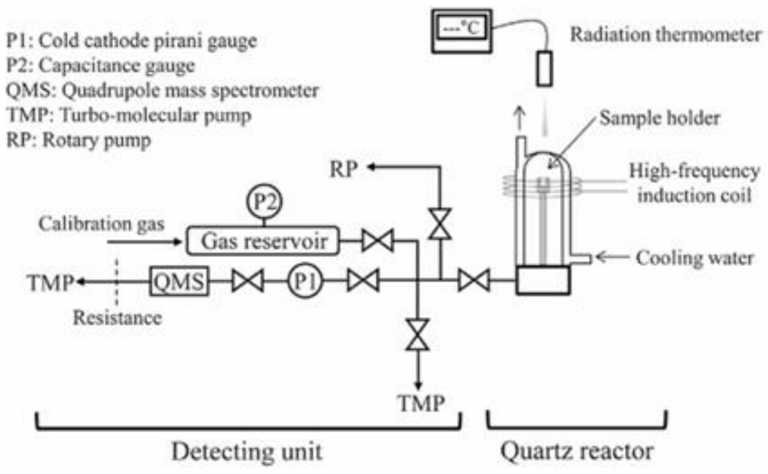

Fig. 3.19 Schematic diagram of CO_2-TPD (Ishii & Kyotani, 2016)

Table 3.7 shows the analysis procedure used in CO_2-TPD and H_2-TPR. The amount of catalyst used in both process is around 50 mg.

Table 3.7 H_2-TPR and CO_2-TPD operating procedure

Step	Procedure of	Gas	Holding Time (min)	Target temp. (°C) (ramping rate)
1	Pretreatment	Ar	60	600 (10°C/min)
2	H_2-TPR	Ar	--	50
3	H_2-TPR	5% H_2/Ar	10	600 (10°C/min)
4	H_2-TPR	Ar	--	50
5	CO_2-TPD	CO_2	30	50
6	CO_2-TPD	He	10	50
7	CO_2-TPD	He	10	600(10°C/min)

3.5 Equation Used and Data Processing

Tabel 3.8 shows the equation used to calculate the selectivity of methanol or carbon monoxide, conversion of CO_2 and space time yield of methanol or carbon monoxide. All catalytic test data analysis is conducted using Microsoft Excel 2013. Equilibrium result is calculated using Aspen Plus v10.

Table 3.8 Equation used for this research

Parameter	Equation	
CO_2 conversion	$\mathrm{X_{CO_2}} = \frac{[\mathrm{CO_2\ in}] - [\mathrm{CO_2\ out}]}{[\mathrm{CO_2\ in}]} \times 100\%$	3-1
Methanol Selectivity	$\mathrm{Y_{MeOH}} = \frac{[\mathrm{MeOH\ out}]}{[\mathrm{CO\ out}] + [\mathrm{MeOH\ out}]} \times 100\%$	3-2
CO Selectivity	$\mathrm{Y_{CO}} = \frac{[\mathrm{MeOH\ out}]}{[\mathrm{CO\ out}] + [\mathrm{MeOH\ out}]} \times 100\%$	3-3

Table 3.8 Equation used for this research (cont.)

Parameter	Equation	
Methanol Space Time Yield	$STY_{MeOH}\ [mg/g_{cat}.h] = \frac{Y_{MeOH} \times X_{CO_2} \times MW_{MeOH} \times F_{CO_2}}{m_{cat} \times 10000}$	3-4
CO Space Time Yield	$ST_{CO}\ [mg/g_{cat}.h] = \frac{Y_{CO} \times X_{CO_2} \times MW_{CO} \times F_{CO_2}}{m_{cat} \times 10000}$	3-5
CO Conversion	$X_{CO} = \frac{[\text{CO in}] - [\text{CO out}]}{[\text{CO in}]} \times 100\%$	3-6

F_i denotes the molar flow rate of compound i in mmol/hour.

In addition, XRD, FTIR, XPS, CO_2-TPD and H_2-TPR data is processed using OriginLab 2018. Curve fitting for H_2-TPR is processed using PeakFit v4.12.

3.6 Gas Calibration with Gas Chromatography

3.6.1 H_2 Calibration

H_2 calibration is done using a 99.9999% purity H_2. 5 different volumes of H_2 are injected to the TCD detector of the GC. 0.1 mL, 0.3 mL, 0.5 mL, 0.8 mL and 1 mL of H_2 is used to calibrate the H_2 concentration. Each volume is injected twice to ensure the consistency of the calibration and the average value each reading is used to determine the average area of GC reading.

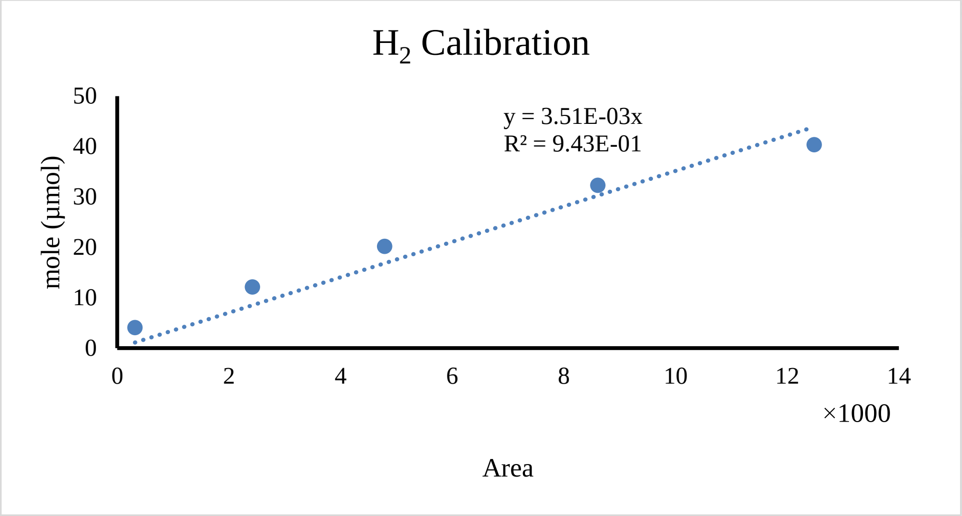

Fig. 3.20 H_2 calibration curve

The regression result shows a great colleration of 0.943 and the H_2 calibration equation is

H_2 concentration = $3.51 \times 10^{-3} \times$ H_2 GC area (3-7)

3.6.2 CO Calibration

CO calibration is done using a 0.3% purity mixture of CO/He. 5 different volumes of CO are injected to the TCD detector of the GC. 0.1 mL, 0.3 mL, 0.5 mL, 0.8 mL and 1 mL of CO is used to calibrate the CO concentration. Each volume is injected twice to ensure the consistency of the calibration and the average value each reading is used to determine the average area of GC reading.

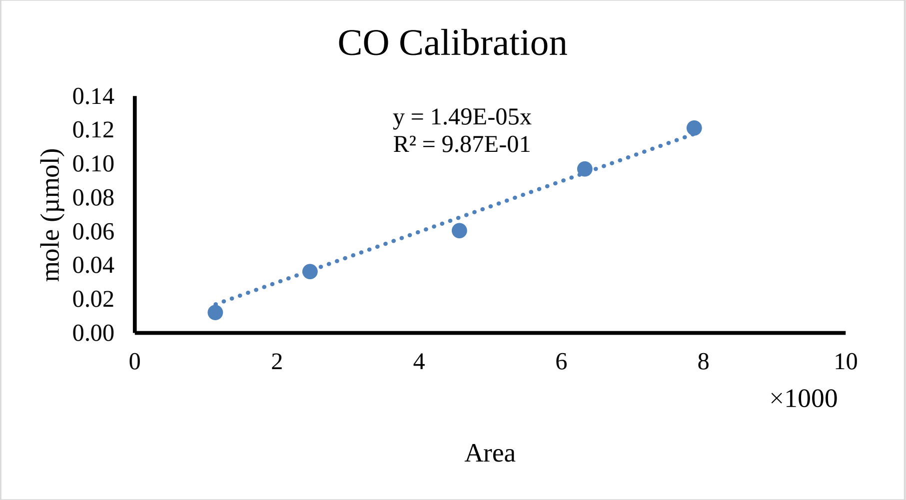

Fig. 3.21 CO calibration curve

doi:10.6342/NTU202403130

The regression result shows a great colleration of 0.987 and the CO calibration equation is

$$\text{CO concentration} = 1.49 \times 10^{-5} \times \text{CO GC area} \tag{3-8}$$

3.6.3 CO_2 Calibration

CO_2 calibration is done using a 99.9999% purity CO_2. 5 different volumes of CO_2 are injected to the TCD detector of the GC. 0.1 mL, 0.3 mL, 0.5 mL, 0.8 mL and 1 mL of CO_2 is used to calibrate the CO_2 concentration. Each volume is injected twice to ensure the consistency of the calibration and the average value each reading is used to determine the average area of GC reading.

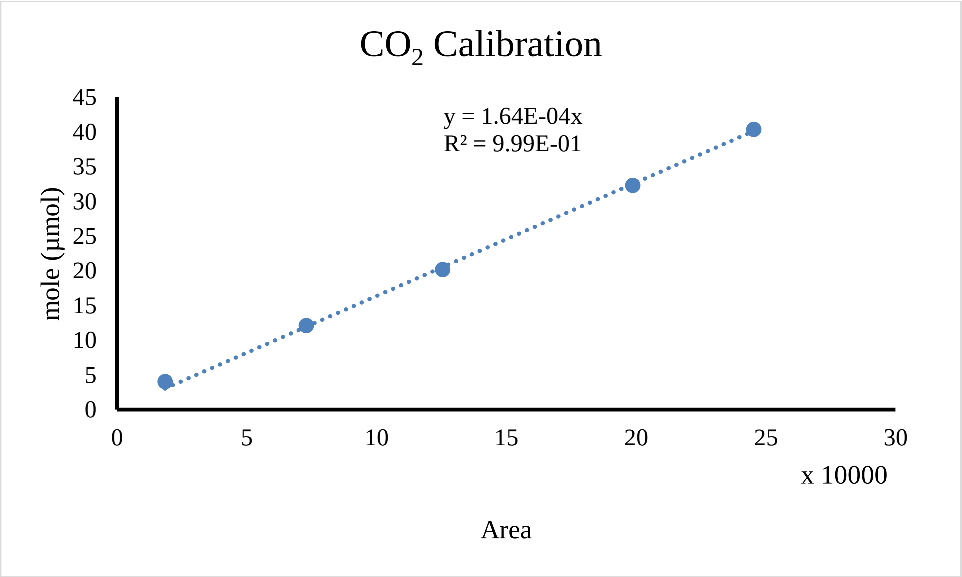

Fig. 3.22 CO_2 calibration curve

The regression result shows a great colleration of 0.999 and the CO calibration equation is

$$CO_2 \text{ concentration} = 1.64 \times 10^{-4} \times CO_2 \text{ GC area} \tag{3-9}$$

3.6.4 Methanol Calibration

Methanol calibration line is measured by using a standard solution of 1000 ppm methanol. 5 different volumes of methanol are injected to the FID detector of the GC. 1 μL, 2 μL, 3 μL, 4 μL and 5 μL of methanol is used to calibrate the methanol concentration. Each volume is injected twice to ensure the consistency of the calibration and the average value each reading is used to determine the average area of GC reading.

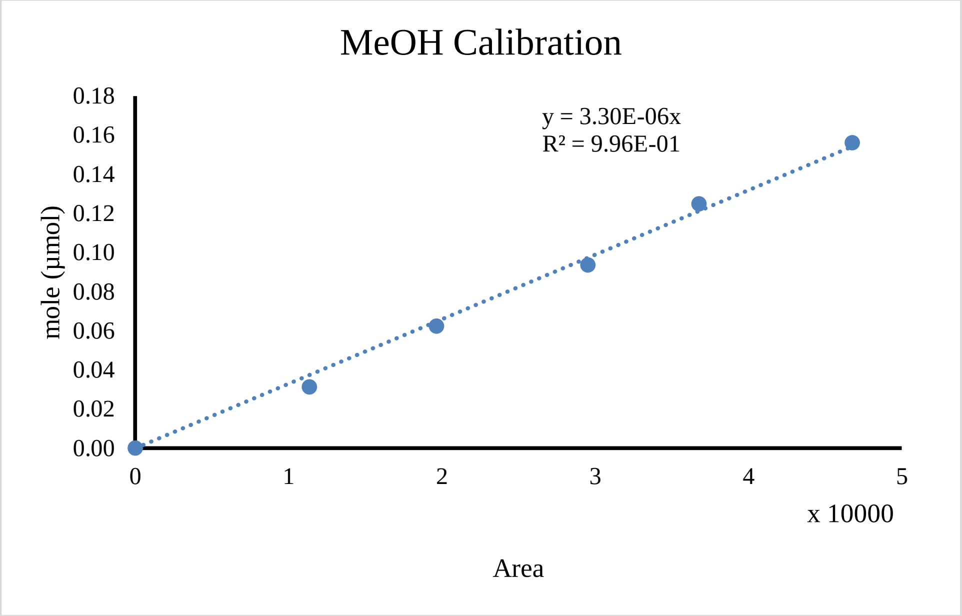

Fig. 3.23 Methanol calibration curve

The regression result shows a great colleration of 0.996 and the CO calibration equation is

$$\text{MeOH concentration} = 3.30 \times 10^{-6} \times \text{MeOH GC area} \quad (3\text{-}10)$$

doi:10.6342/NTU202403130

CHAPTER IV

RESULT AND DISCUSSION

4.1 Catalyst Characteristic Test

The catalyst characteristic test is done to determine the relation between the physicochemistry, morphology, crystalinity and surface characteristic of catalyst to the performance of catalyst.

4.1.1 XRD Result

The comparison of different metal loading (30%, 40%, and 100%) on CZZ catalyst is shown in Fig 4.1. It is shown that all samples has a visible peak of CuO can be clearly seen at 2θ = 35.5°, 38.7° and 48.7° and peak of ZnO at 2θ = 30.8°, 34.3°, and 35.3°. The sample with the least amount of metal loaded (30CZZ-hBN) shows the least intense CuO and ZnO peak in the XRD result. In samples loaded with hBN, the peak of hBN can be observed at 2θ = 26.7°, 41.6°, and 55.1°. The largest hBN peak appears at 26.7° which corresponds to the (200) crystal structure of hBN. Zirconia oxide could not be detected in XRD as calcination at 400°C will cause the zirconia to exhibit an amorphous phase which is undetectable in XRD.

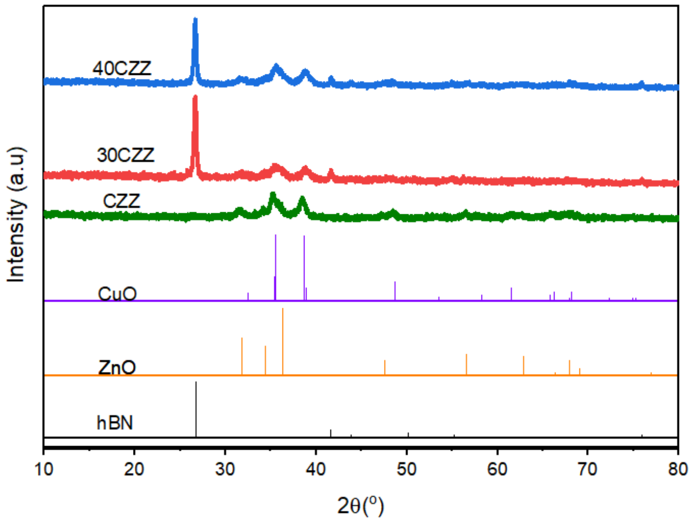

Fig. 4.1 XRD profile of different weight% of CZZ catalyst with hBN support

doi:10.6342/NTU202403130

The comparison of CZZ based catalyst with different metal loading is observed below in Fig 4.2. All samples display a visible peak of CuO at $2\theta = 35.5^o$, 38.7^o and 48.7^o, peak of ZnO at $2\theta = 30.8^o$, 34.3^o, and 35.3^o, and of hBN at $2\theta = 26.7^o$, 41.6^o, and 55.1^o. The largest hBN peak appears at 26.7^o which corresponds to the (200) crystal structure of hBN. Similar to CZZ based catalyst, the zirconia oxide is in the amorphous phase as all CZZ catalyst are calcined at the same temperature, as such is not detected by XRD. Furthermore, all CZZ based catalyst has a metal loading of Cu : Zn : Zr : X (X = La, Ce, Mo, W) at 6 :3 :0.75 :0.25, which makes the promoter hard to be detected due to the small amount of the element present in the sample (after being loaded with hBN the amount of promoter is around 1% of the entire catalyst) or a well dispered promoter.

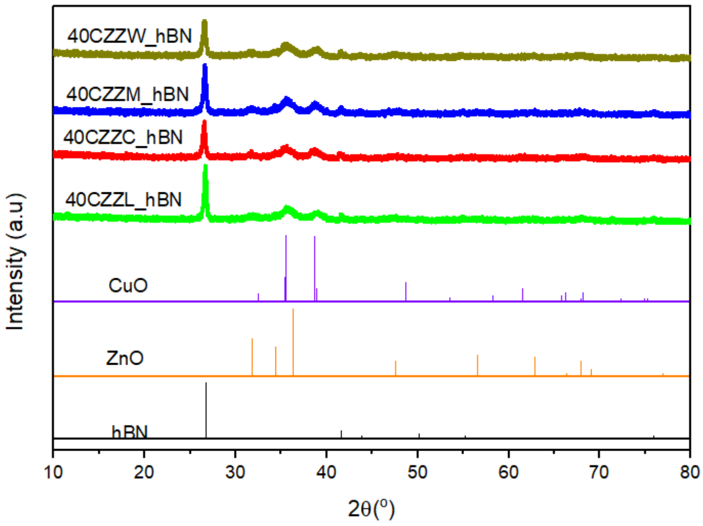

Fig. 4.2 XRD profile of 40CZZX_hBN catalyst (X=La, Ce, Mo, W)

The different crystalinity of catalyst with and without hBN loading before and after reaction is shown below in Fig 4.3. Comparison of the crystal structure of CZZC and 40CZZC_hBN is made before reaction and after being tested for reverse water gas shift and CO_2 hydrogenation to methanol in both samples. The sample without hBN loading shows an obvious peak of Cu at $2\theta = 43.5^o$, 50.5^o, and 74.7^o after undergoing reaction while this peak is notably absent in used sample with hBN. This indicates that the sample hBN utilized the active site of the catalyst more than the sample without hBN as some Cu still remains and didn’t react to become CuO during reaction.

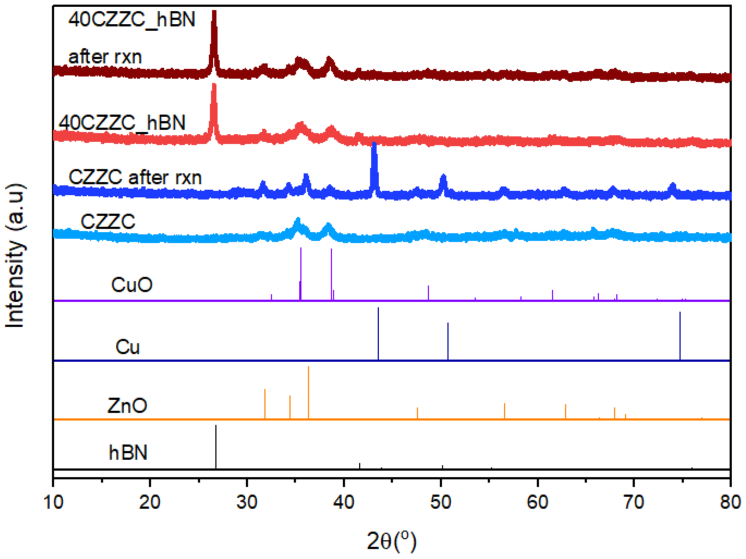

Fig. 4.3 XRD profile of CZZC and 40CZZC_hBN before and after reaction

As seen in Fig 4.4, CC based catalyst has a composition of Cu : Ce = 1 :3, the most dominant peak is CeO at $2\theta = 28.6^{o}$, 47.5^{o}, and 56.3^{o} while the CuO peak is not visible due to the small quantity, as such another analysis method (XPS) is also used to confirm the presense of Cu. For CC sample, after reaction, Cu signal appears at $2\theta = 43.5^{o}$, 50.5^{o} and 74.7^{o}. The Cu signal is not noticeable in samples loaded with hBN before and after reaction due to the copper amount being lower that the sample without hBN.

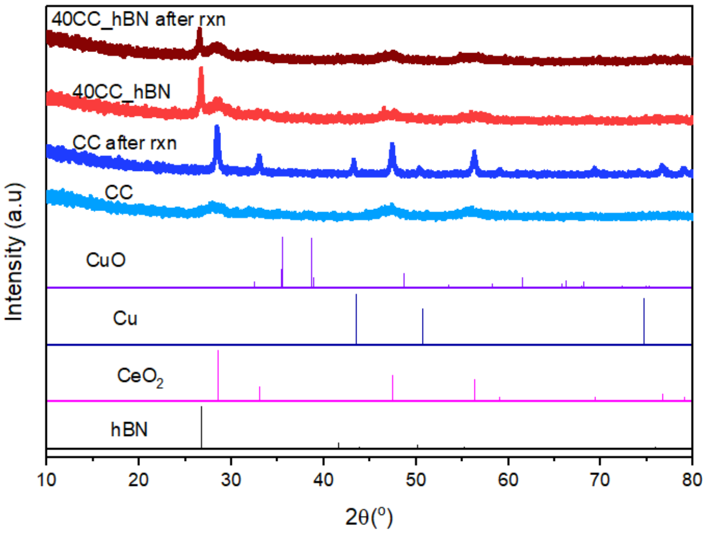

Fig. 4.4 XRD profile of CC and 40CC_hBN before and after reaction

In Fig 4.5, the metal composition of CFC based catalyst is Cu : Fe : Ce = 0.75 : 0.25 : 1, as such the most noticeable peak in the XRD profile is CeO_2 along with some traces of Fe_2O_3 hematite at 2θ = 33.2°, 36.6°, and 39.3°. While there is a visible CuO peak present at CFC catalyst, this peak is not visible after reaction but Cu peak is not visible, indicating the change of crystal structure after reduction and Cu is present at only miniscule amount. The most interesting point in the profile is the noticeable reduction of (200) hBN peak in CFC sample, even though hBN composes 60% of the catalyst. As CFC is the only catalyst that is coprecipitated at pH 9 to ensure the formation of FeO_x particle, this shows that the coprecipitation pH has influence on the structure of hBN as evident by a lower intensity at 2θ = 26.7° compared to the peaks at Fig 4.1 - Fig 4.4. Due to Cu and CuO being presented in a small quantity which can't be detected by XRD, another analysis method is used to confirm the presence of Cu element in the catalyst via XPS.

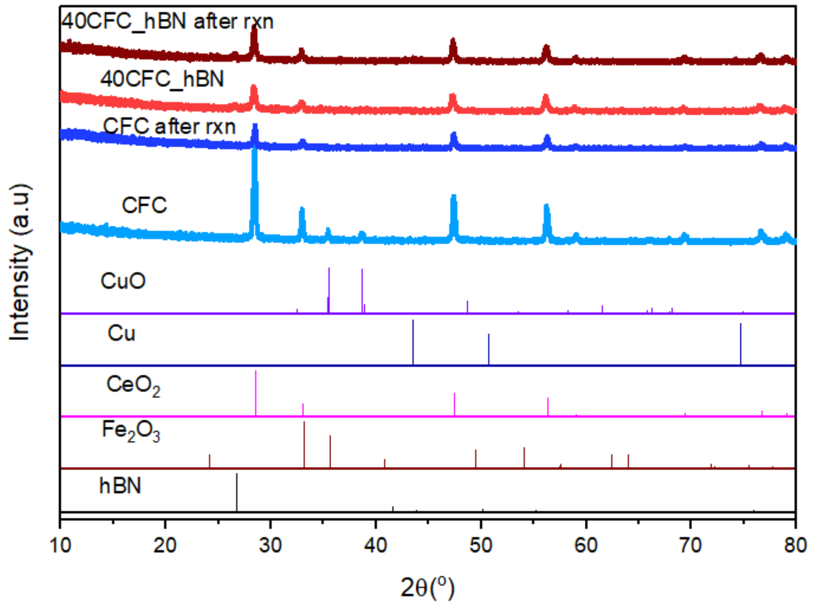

Fig. 4.5 XRD profile of CFC and 40CFC_hBN before and after reaction

Lastly, the XRD of hBN is presented below in Fig 4.6. From the overall scan in Fig 4.6 (a), there is very little difference between the fresh hBN and hBN after Hummer's method, both samples also shows an identical peak to the standard XRD peak. During the slow scan in Fig 4.6 (b), which is done from 2θ = 25° to 2θ = 30°, there appears to be a slight shift of hBN (200) peak from 26.631^o at the fresh hBN to 26.611^o at the hBN after Hummer’s method. The left shift of peak in XRD indicates lattice expansion of (200) hBN after exfoliation.

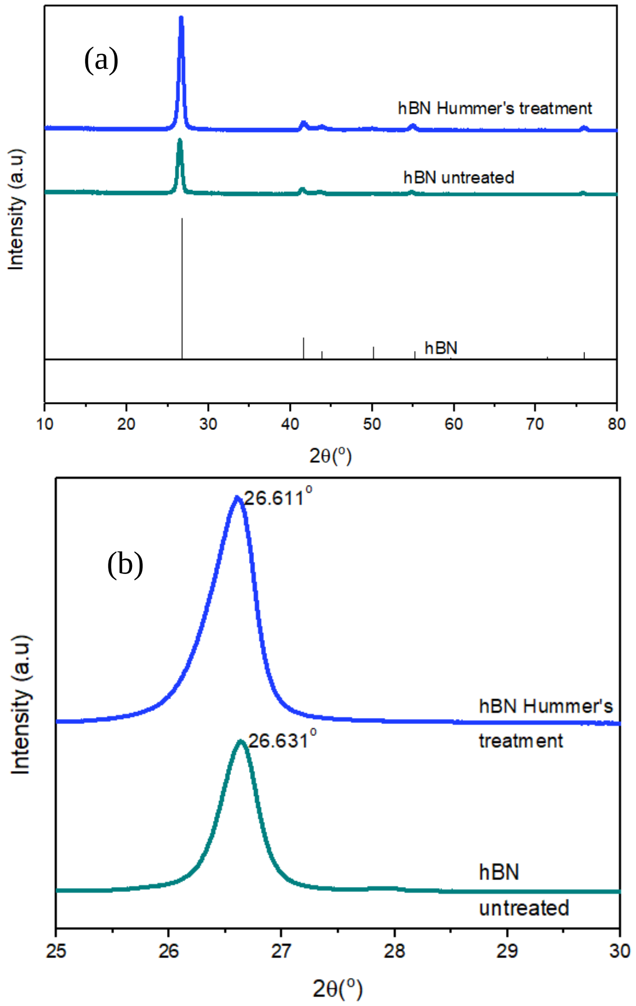

Fig. 4.6 XRD profile of (a) overall and (b) slow scan of hBN

4.1.2 FTIR Result

FTIR analysis is used to observe the functional group that is present in a material. For this research, FTIR is used to observe the bonding that is present in hBN, comparing the functional group in fresh hBN and hBN after being treated with Hummer’s method.

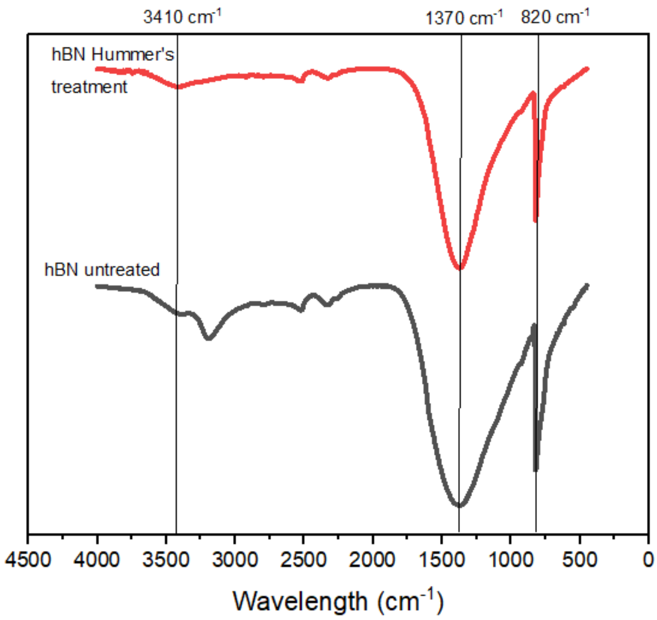

Fig. 4.7 FTIR result of fresh hBN and hBN after Hummer's method

From Fig 4.7, there is a peak at around 820 cm^{-1} and 1370 cm^{-1} which corresponds to B-N plane stretching vibration and B-N non plan stretching vibration respectively. The hBN sample treated with Hummer's method shows an additional peak at 3410 cm^{-1} which corresponds to –OH bond, suggesting that Hummer's method can also functionalize the hBN with –OH group.

4.1.3 BET Result

The BET calculated surface area of various catalyst and hBN is shown in Table 4.2. The BET result of 40% metal loading on hBN supported catalyst has larger surface area compared to 30% metal loading and 100% metal loading. Curiously, CC and CFC catalyst has a similar BER surface area with and without hBN but the catalytic performance presented in Chapter 4.2 later shows a significant difference in catalytic activity. This indicates a minor influence of BET surface area to catalytic activity, especially for non CZZ based catalyst. Lastly, hBN that is exfoliated with Hummer's method shows a significant increase in surface area compared to the untreated hBN due to layers of hBN separating after Hummer's method.

Table 4.1 BET result of various catalyst

Catalyst Name	BET Area (m^2/g)
30CZZ_hBN	46.21
40CZZ_hBN	49.16
CZZ	37.86
40CZZL_hBN	42.77
CZZC	45.92
40CZZC_hBN	48.82
40CZZM_hBN	46.26
40CZZW_hBN	46.80
CFC	3.90
40CFC_hBN	3.86
CC	49.23
40CC_hBN	49.16
hBN untreated	1.44
hBN Hummer's treatment	18.78

4.1.4 SEM Result

SEM analysis is used to observe the surface morphology of a material, including catalyst. Before a sample is observed, sample is placed on a carbon tape and pretreated with platinum coating in a vacuum chamber to ensure there is no excess electron on the catalyst surface that will interfere the image scan.

doi:10.6342/NTU202403130

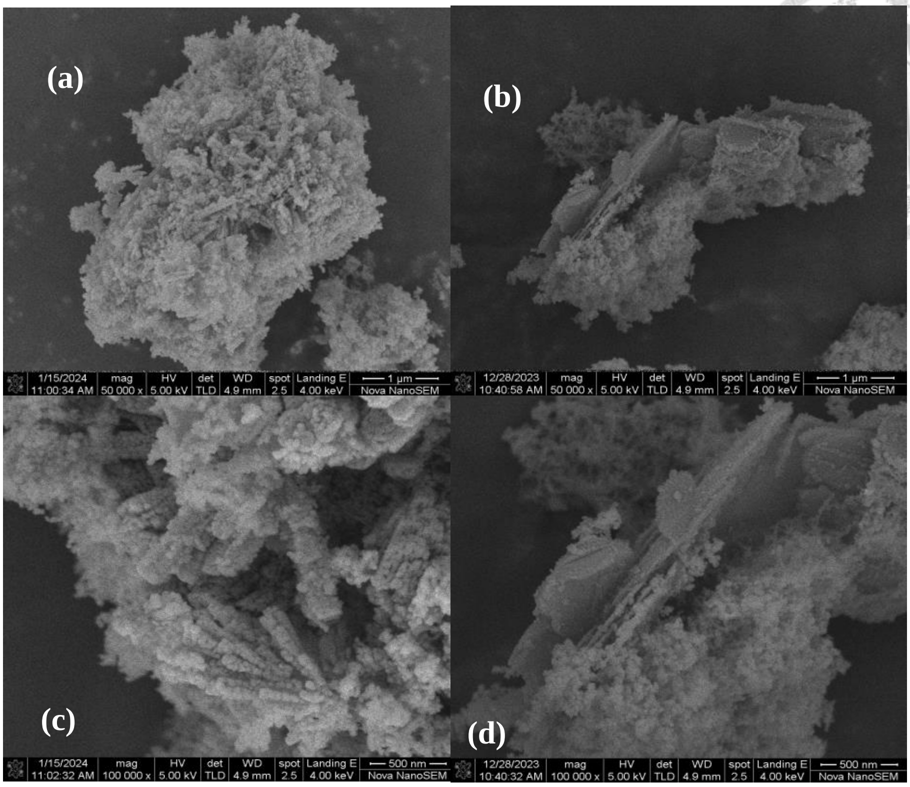

Fig. 4.8 SEM result of (a) CZZC and (b) 40CZZC_hBN with 50000 magnification and (c) CZZC and (d) 40CZZC_hBN with 100000 magnification

First, the result of catalyst with and without hBN loading is observed with SEM in Fig 4.8. CZZC catalyst (depicted in Fig 4.8 (a) and Fig 4.8 (c)) shows a cluster of metal aggragate on each other within the catalyst particle. Meanwhile in the hBN supported catalyst (depicted in Fig 4.8 (b) and Fig 4.8 (d)), the metal will stick on the hBN support, providing an additional contact area for the catalyst, supporting the result of BET result where 40CZZC_hBN has more surface area than CZZC.

Next, comparison of fresh (Fig 4.9 (a)) and post Hummer’s method (Fig 4.9 (b)) hBN morphology is observed with SEM. As Hummer’s method is done to exfoliate the hBN, effectively separating the layers to make hBN easier to disperse in water, it is hoped that hBN treated with Hummer’s method has a clearer monolayer formation compared to fresh hBN

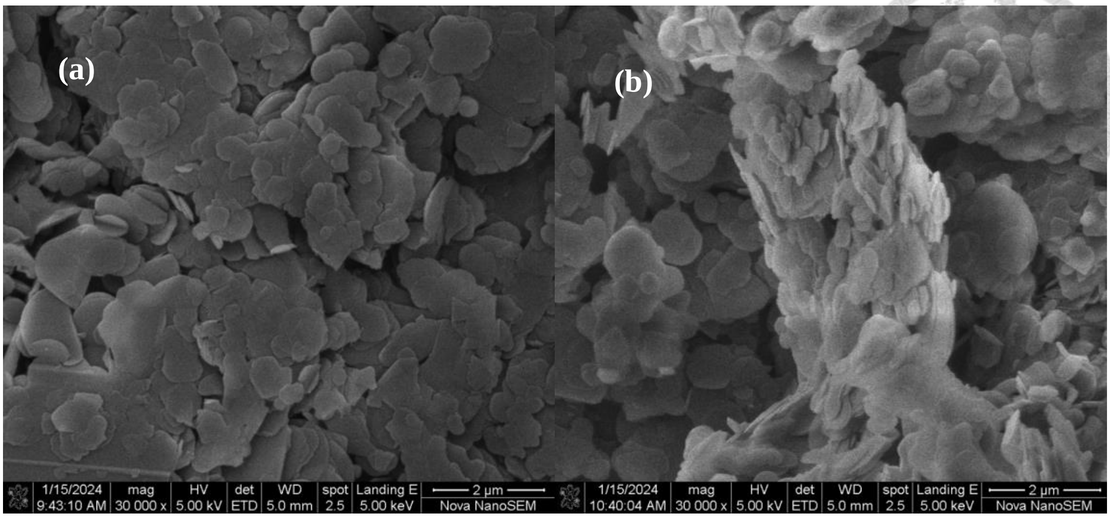

Fig. 4.9 SEM result of (a) untreated hBN and (b) post Hummer's method hBN with 30000 magnification

As seen from the figure above, hBN treated with Hummer's method shows an even clear layered structure compared to untreated hBN which shows only clusters of hBN with minimal layer separation.

4.1.5 Chemical Composiion Analysis Result

EDS analysis is used to determine the chemical compostition of a material. In this study, EDS analysis is done in conjuction with SEM as the electron beam from SEM will emit X-ray that can be used to analyze the chemical composition of a sample.

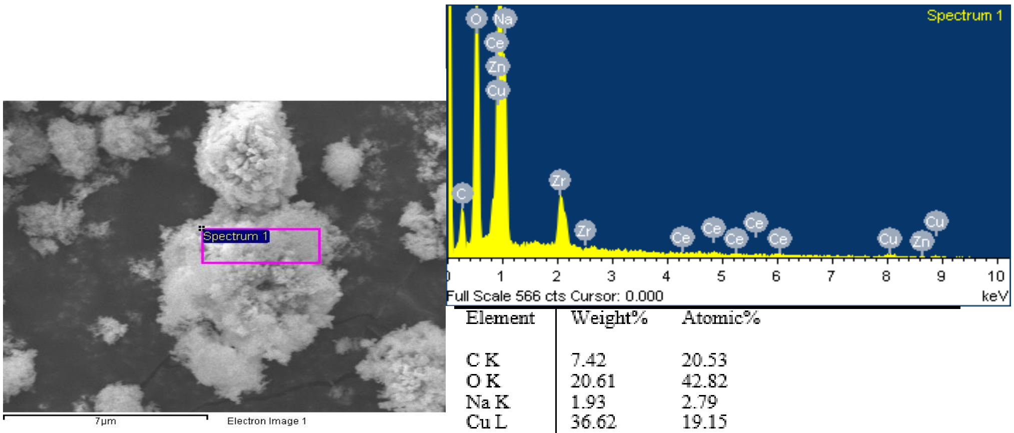

Element	Weight%	Atomic%
C K	7.42	20.53
O K	20.61	42.82
Na K	1.93	2.79
Cu L	36.62	19.15
Zn L	20.28	10.31
Zr L	10.07	3.67
Ce L	3.08	0.73
Totals	100.00	

Fig. 4.10 SEM-EDS result of CZZC

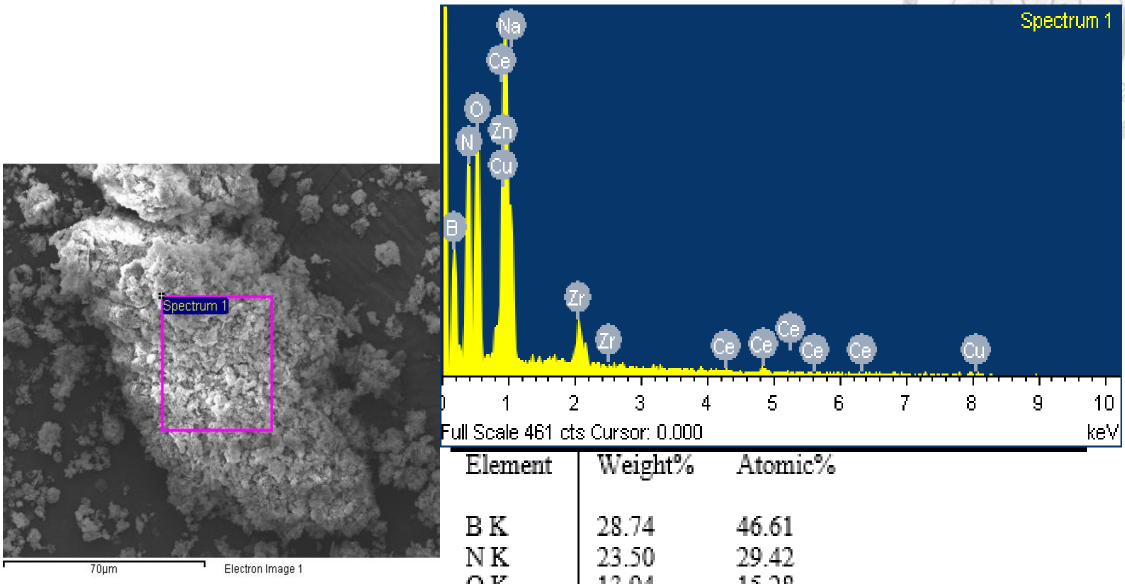

Element	Weight%	Atomic%
B K	28.74	46.61
N K	23.50	29.42
O K	13.94	15.28
Na K	0.00	0.00
Cu L	19.66	5.43
Zn L	8.57	2.30
Zr L	3.87	0.74
Ce L	1.72	0.21
Totals	100.00	

Fig. 4.11 SEM-EDS result of 40CZZC_hBN

We compare the result of EDS for CZZC based catalyst without hBN support in Fig 4.10 and with hBN support in Fig 4.11. For CZZC catalyst, there is a presence of C in the sample due to the carbon tape that is used in SEM and EDS. In addition a small presence of Na is detected due to the precipitating agent containing Na that is not cleaned during filtration. In theory, both samples has the composition of Cu:Zn:Zr:Ce of 6:3:0.75:0.25 from the preparation method.

Table 4.1 shows that metal loading detected by EDS. Cu and Zn appears to have less amount compared to Zr and Ce in all sample, which could be attributed to the metal salt precursore of Cu and Zn ($Cu(NO_3)_2.3H_2O$ and $Zn(NO_3)_2.6H_2O$) being more hygroscopic compared to $ZrO(NO_3)_2.xH_2O$ and $Ce(NO_3)_3.6H_2O$, as such the weight is easily affected by water vapor in the atmosphere. Due to this, the metal loading of the catalyst with hBN according to EDS is 33.82%, which is has a deviation from 40%. The atomic ratio of B and N has a deviation of around 15% which is caused by the EDS peak of N and O overlapping as such the quantification of N is not accurate. Furthermore, the platinum particle coating that is used for SEM-EDS shares the same peak with Zr in the catalyst, affecting the measurement of EDS.

Table 4.2 Comparison of theoretical metal loading compared to EDS result

Element	Theoretical amount	EDS amount (CZZC)	EDS amount (40CZZC_hBN)
Cu	60	52.28	58.13
Zn	30	28.95	25.34
Zr	7.5	14.38	11.44
Ce	2.5	4.40	5.09

4.1.6 XPS Result

XPS analysis is used to observe the electron configuration of a certain element in a material. As the reactions mostly occurs at the surface of the catalyst instead of the bulk, the study of surface electron configuration is important to observe the readiness for catalyst surface to undergo a chemical reaction and the phase of material present.

The survey XPS of the overall binding energy for six different catalyst is seen in Fig 4.12, the peak of C 1s, B 1s, O 1s, N 1s and Cu 2p is present in every sample. Additionally, unique promoter of each element such as Zn 2p and Zr 3d for CZZ based catalyst, La 3d for 40CZZL_hBN, Ce 3d for 40CZZC_hBN, 40CC_hBN and 40CFC_hBN, Mo 3d for 40CZZM_hBN, W 4f for 40CZZW_hBN, and Fe 2p for 40CFC_hBN

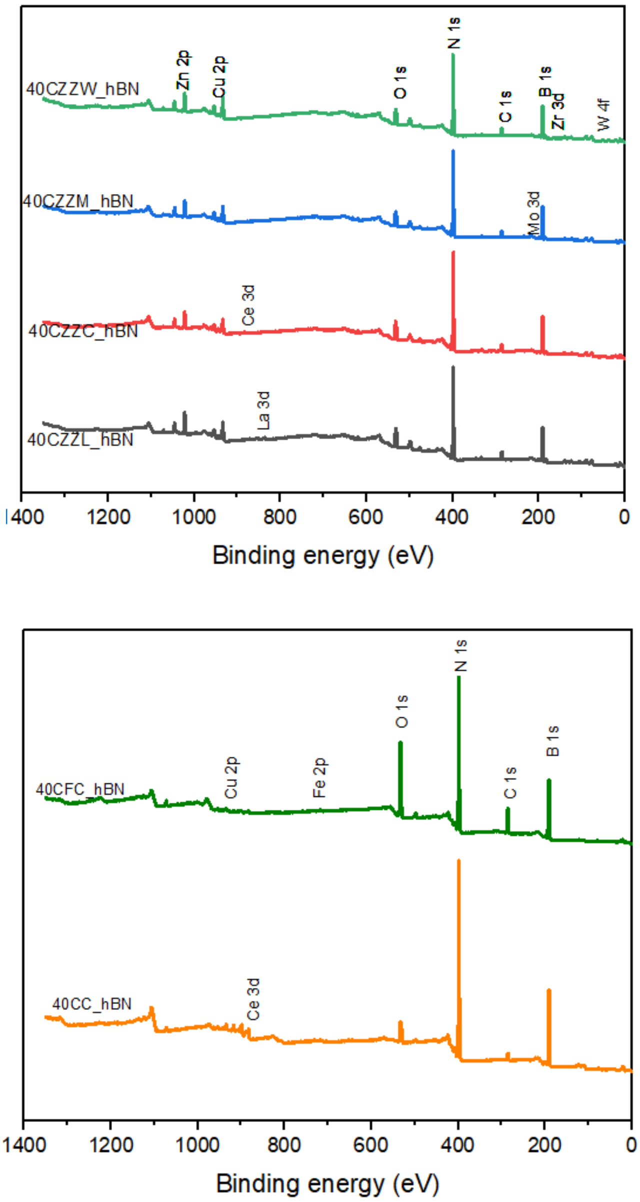

Fig. 4.12 XPS Survey scan of different catalyst

The XPS of copper in six different fresh catalyst is presented in Fig 4.13. The copper state in all catalyst corresponds to CuO which is characterized by 2 distinct peak (Cu $2p_{3/2}$ at ~933.6 eV and Cu $2p_{1/2}$ at ~953 eV) and 2 satelite peaks (the first one at ~943 eV and the second one at ~963 eV). All sample except 40CC_hBN shows a shift towards a lower energy level on the main peak ($2p_{3/2}$) compared to the reference peak (~933.6 eV), indicating all catalyst are more prone to bind with electron and improve their catalytic ability. The weak signals of 40CC_hBN and 40CFC_hBN is caused by the low CuO amount in the catalyst.

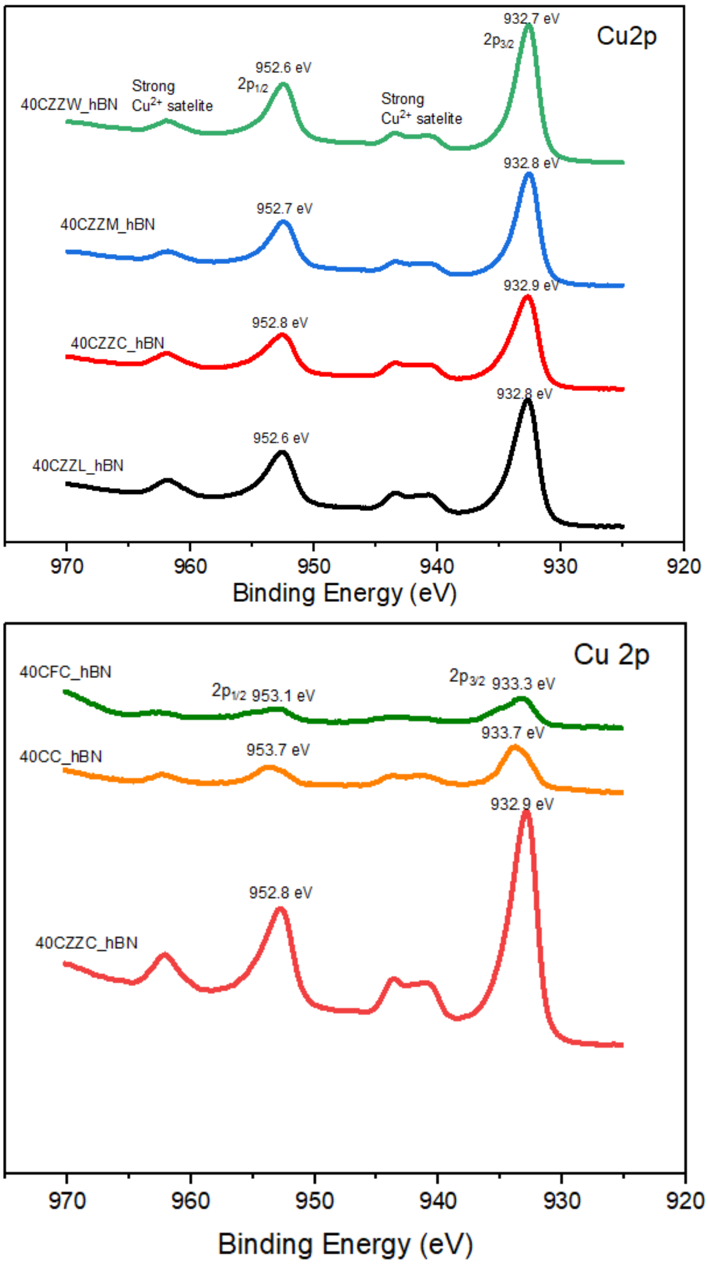

Fig. 4.13 XPS result of Cu 2p on different catalyst

As seen in Fig 4.14, Zn 2p has two distinct peak (Zn $2p_{3/2}$ at ~1022.2 eV and Zn $2p_{1/2}$ at ~1045 eV) , which corresponds to ZnO, and all samples exhibit a shift to lower binding energy compared to the main peak (Zn $2p_{3/2}$), which is similar to the trend in Cu 2p.

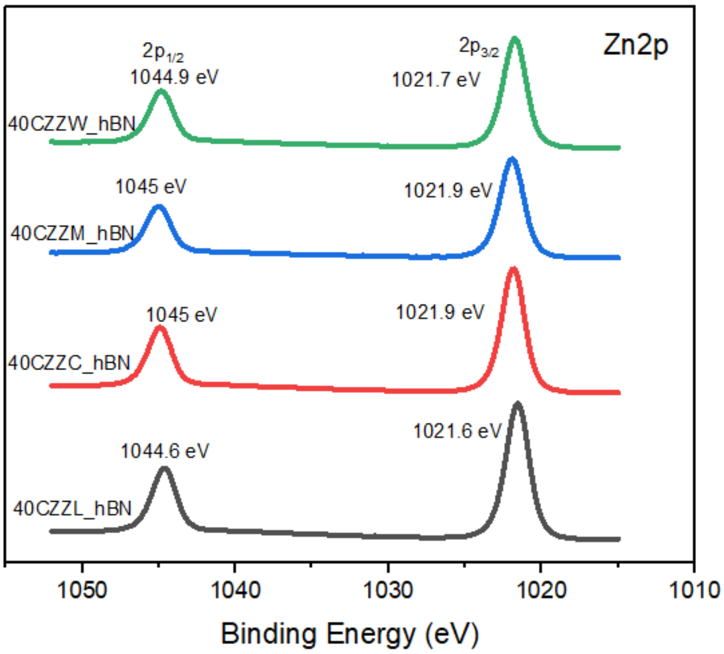

Fig. 4.14 XPS result of Zn 2p in four CZZ based catalyst

Zr 3d profile of CZZ catalyst is observed in Fig 4.15. There is 2 peaks present in Zr 3d XPS scan, Zr $3d_{5/2}$ at ~182.8 eV and Zr $3d_{3/2}$ at ~185.2 eV, and the profile of the peak corresponds to ZrO_2. All CZZ based catalyst tested demonstrated a shift to lower energy level compared to the main peak Zr $3d_{5/2}$, a similar trend to Cu and Zn.

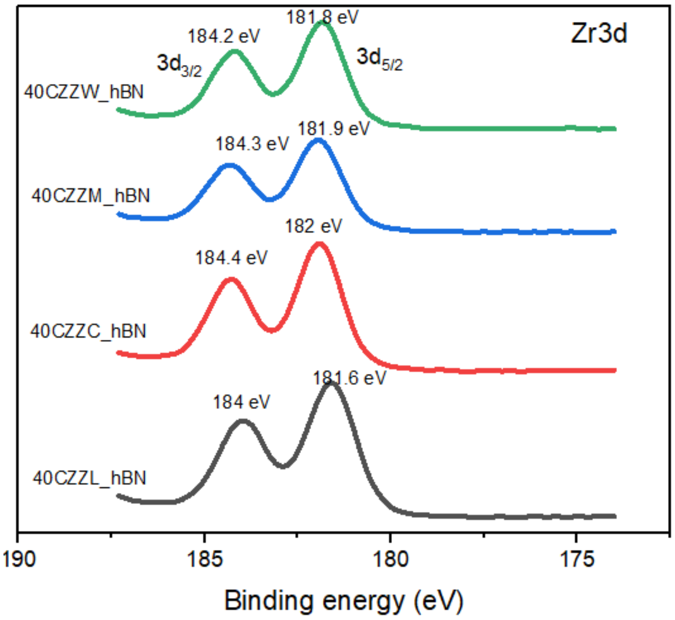

Fig. 4.15 XPS result of Zr 3d in four CZZ based catalyst

The profile of Ce 3d for three catalyst with Ce as promoter is presented in Fig 4.16. For

Ce 3d, there are 2 distinct area Ce 3d$_{5/2}$ which ranges from ~883.5 eV to ~900 eV and Ce 3d$_{3/2}$ which ranges from ~903 eV to ~ 917 eV. While 40CC_hBN and 40CFC_hBN peaks corresponds to the Ce^{4+} electron configuration, the profile of 40CZZC_hBN bears a closer resemblance to Ce^{3}, which is noticeable by the lack of peak at ~907 eV for the Ce 3d profie at 40CZZC_hBN. This might suggest zinc and zirconia doping in 40CZZC_hBN will reduce the Ce^{4} to Ce^{3+}. The presence of Ce^{3+} has been reported to occur by doping a copper based catalyst with tungsten and Ce^{3+} has been cited to increase the performance of a catalyst (Yan et al., 2022).

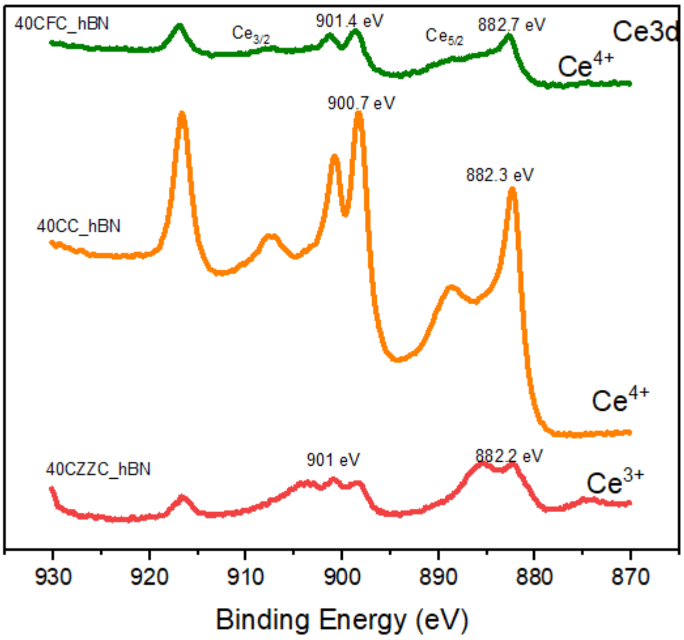

Fig. 4.16 XPS result of Ce 3d in three ceria doped catalyst

From Fig 4.17, it is noted that La 3d in Fig 4.17(a) has two peaks with multiplet spilt (La 3d$_{5/2}$ at ~836 eV and La 3d$_{3/2}$ at ~852 eV) that corresponds to the La^{3+} phase, Mo 3d in Fig 4.17 (b)) has two peaks (Mo 3d$_{5/2}$ at ~233.5 eV and Mo 3d$_{3/2}$ at ~236 eV) which is identic to MoO_3, W 4f in Fig 4.17 (c) has two peaks (W 4f$_{7/2}$ at ~35.8 eV and W 4f$_{5/2}$ at ~38 eV), which corresponds to WO_3. The XPS profile for Fe 2p in Fig 4.17 (d) only has 1 peak which appears at 717.9 eV in XPS profile (the standard peak appears at ~713.9 eV). Except for Fe, all catalyst exhibits a shift to the lower energy level compared to the reference.

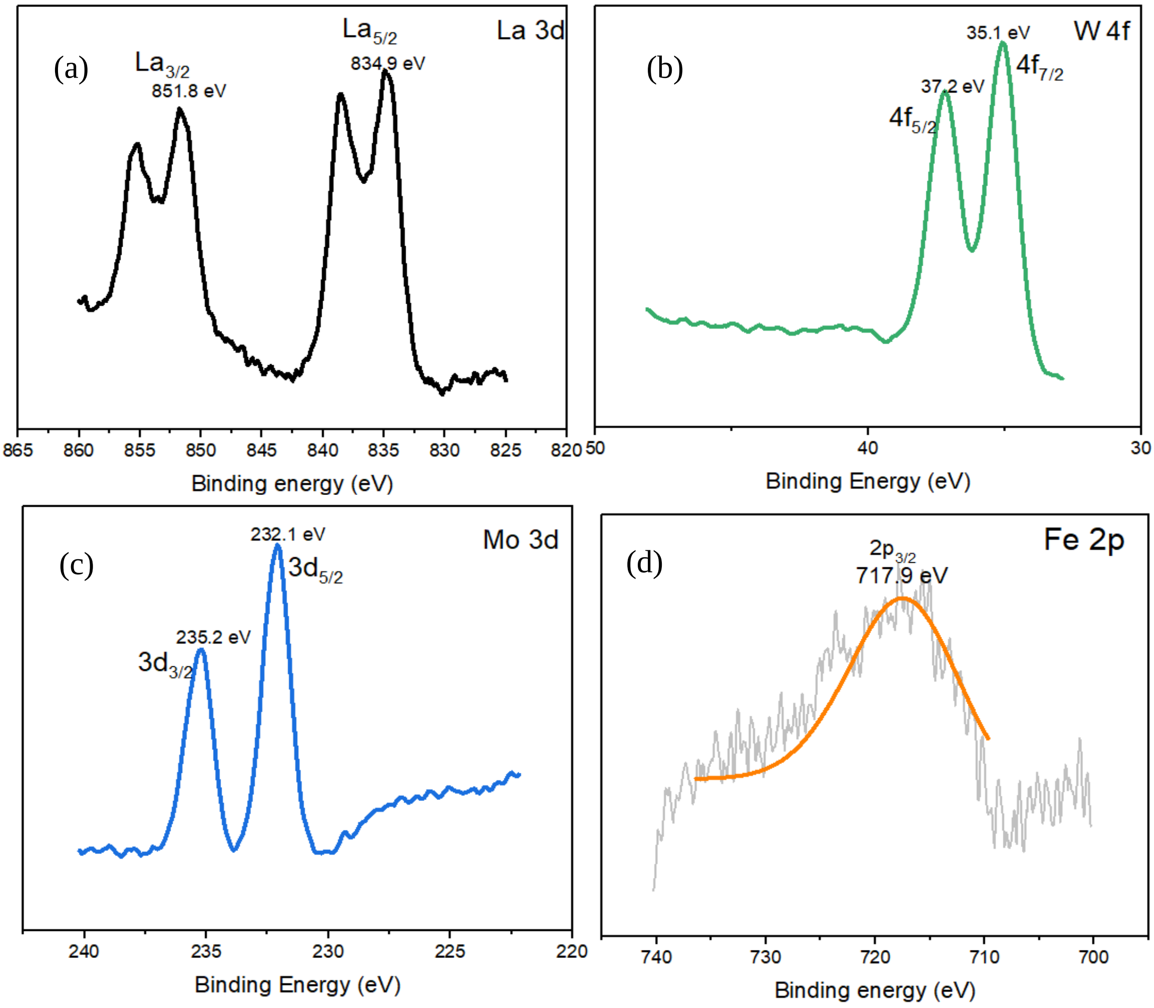

Fig. 4.17 The XPS profile of (a) La 3d in 40CZZL_hBN (b) Mo 3d in 40CZZM_hBN (c) W 4f in 40CZZW_hBN and (d) Fe 2p in 40CFC_hBN

The summary of XPS peak is presented in Table 4.3.

Table 4.3 XPS result summary

Name	Binding energy (eV)							
	Cu	Zn	Zr	La	Ce	Mo	W	Fe
	$2p_{3/2}$	$2p_{3/2}$	$3d_{5/2}$	$3d_{5/2}$	$3d_{5/2}$	$3d_{5/2}$	$4f_{7/2}$	$2p_{3/2}$
40CZZL_hBN	932.8	1021.6	181.8	834.9	-	-	-	-
40CZZC_hBN	932.9	1021.9	181.9	-	882.2	-	-	-
40CZZM_hBN	932.8	1021.9	182	-	-	232.1	-	-
40CZZW_hBN	932.7	1021.7	181.6	-	-	-	35.1	-
40CC_hBN	933.7	-	-	-	882.3	-	-	-
40CFC_hBN	933.3	-	-	-	882.7	-	-	717.9

4.1.7 H_2-TPR Result

H_2-TPR (Temperature Programmed Reduction) analysis is used to determine the reducibility of a catalyst under H_2 gas. Before the H_2-TPR analysis, the sample is pre-treated with argon gas to clean the catalyst's surface before being treated with hydrogen. After pretreatment, 5% of hydrogen mixed with argon is being supplied at the catalyst surface until it reaches 600^{o}C with a ramping rate of 10^{o}C/min. The H_2-TPR has three peaks: α (highly dispersed CuO on catalyst surface), β (CuO that interacts with other carriers on the catalyst), and γ (bulk CuO). The comparison of both catalyst in Fig 4.18 (a) along with the individual profile of 40CC_hBN in Fig 4.18 (b) and 40CZZC_hBN in Fig 4.18(c) is shown below.

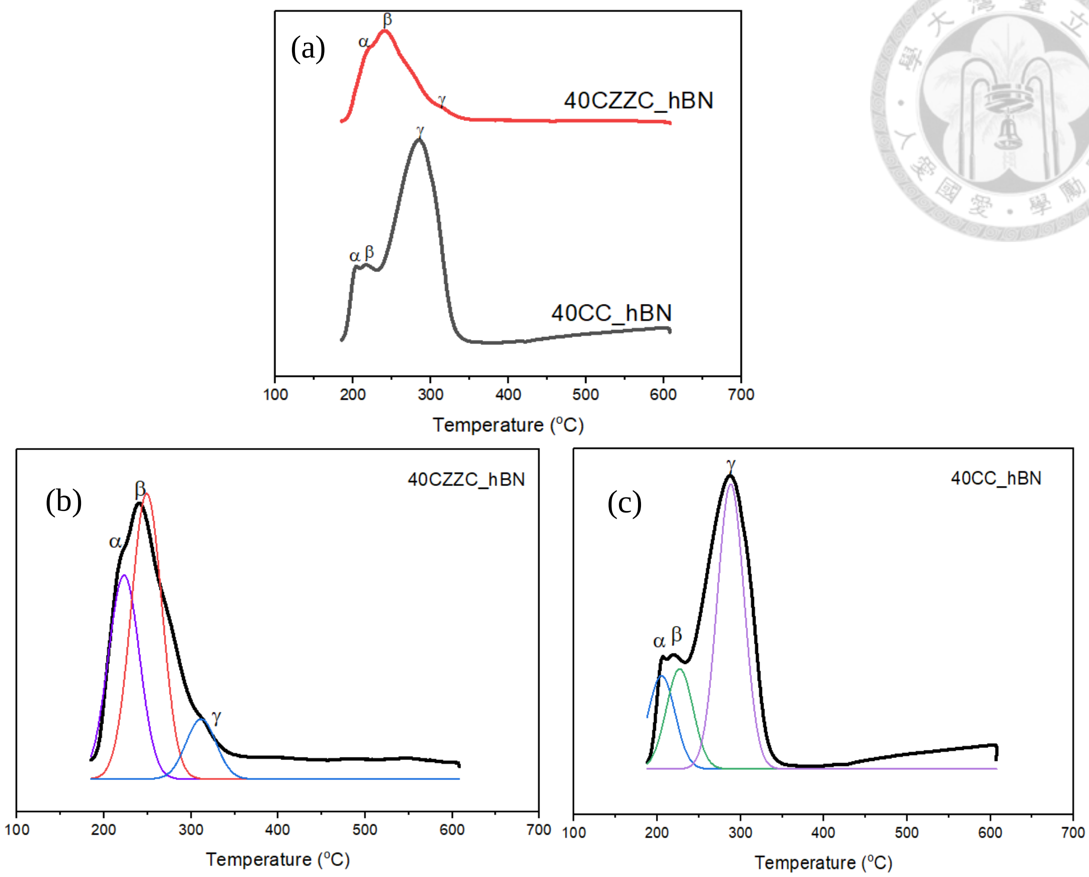

Fig. 4.18 (a) H_2-TPR of 40CC_hBN and 40CZZC_hBN, H_2-TPR with peak fitting for (b) 40CC_hBN and (c) 40CZZC_hBN

The summary of the H_2-TPR peak is presented in Table 4.4 below.

Table 4.4 Summary of H_2-TPR for 40CZZC_hBN and 40CC_hBN

Catalyst	Peak Position (°C)/%			α+β
	α	β	γ	Area %
40CZZC_hBN	220.6 (17.38)	240.4 (69.44)	347.78 (13.18)	86.82
40CC_hBN	207 (6.30)	219.8 (10.60)	287 (83.10)	16.90

As seen in Fig 4.18 and Table 4.4, The H_2-TPR result shows that 40CC_hBN has a lower peak compared to 40CZZC_hBN in all peaks. However, a majority of 40CC_hBN H_2 uptake is from the γ peak, which means the majority of H_2 reduced the bulk CuO. From the sum of α + β peak, 40CZZC_hBN has higher percentage of surface CuO compared to

CuO, which means the 40CZZC_hBN has more CuO reduced on the surface. Both catalyst will be almost fully reduced at 350°C (the reduction temperature).

4.1.8 CO_2-TPD Result

CO_2-TPD (Temperature Programmed Desorption) is used to analyse the basicity of a catalyst, particularity CO_2 hydrogenation to methanol catalyst where the adsorption of CO_2 is a vital process for methanol synthesis. After H_2-TPR analysis, the sample is directly being reacted with pure CO_2 from 50°C to 600°C with a ramping rate of 10°C. CO_2-TPD is divided into three peaks, α corresponds to weak basicity, β corresponds medium basicity, and γ corresponds strong basicity. The comparison of CO_2-TPD for 40CZZC_hBN and 40CC_hBN is presented in Fig 4.19 below.

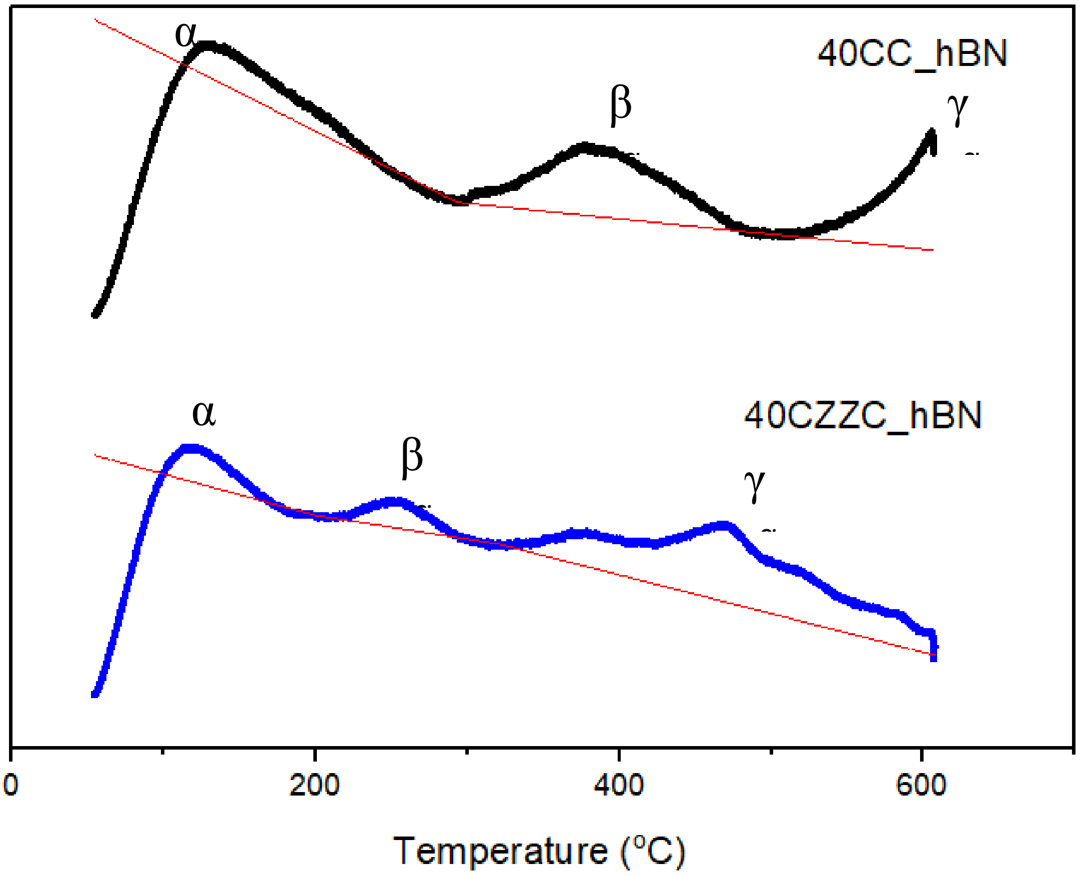

Fig. 4.19 CO_2-TPD result of (a) 40CZZC_hBN and (b) 40CC_hBN

The summary of the CO_2-TPD result for both catalyst is presented in Table 4.5 below.

doi:10.6342/NTU202403130

Table 4.5 Summary of CO_2-TPD for 40CZZC_hBN and 40CC_hBN

Catalyst	Basic Site Area (%)		
	α	β	γ
40CZZC_hBN	10.43	8.63	80.94
40CC_hBN	21.34	51.43	27.23

As shown in Fig 4.19 and Table 4.5, 40CZZC_hBN has higher amount of γ peak (80.94%) compared to α + β peaks (19.06%). In comparison, 40CC_hBN has lower amount of γ peak (27.23%) compared to α + β peaks (73.77%). This result shows that 40CZZC_hBN is more prone to react with CO_2 as it is more ready to absorb CO_2 on the catalyst surface. This shows that the addition of Zn and Zr is beneficial for methanol synthesis in terms of basicity site, aside from the increase of surface area and Ce^{3+} addition in the catalyst surface.

4.2 Catalytic Performance Evaluation

4.2.1 Metal and hBN Loading Effect (CO_2 Hydrogenation)

In this study, hBN is being used as a catalyst support to give the catalyst a more hydrophobic and themally stable property. To test the effect of hBN addition and the optimal metal-hBN loading in the catalyst, 30CZZ_hBN, 40CZZ_hBN and CZZ with no hBN addition is tested for CO_2 hydrogenation to methanol with the reaction condition 230 ^oC at 10 bar for 2 hours. From the result in Fig 4.20 below, loading a CZZ catalyst with hBN can improve the performance of methanol synthesis as shown in Fig 4.20 (a) where 30CZZ_hBN shows a better MeOH selectivity followed by CZZ and 40CZZ_hBN and Fig (b) shows that 40CZZ_hBN has the best CO_2 conversion follow by 30CZZ and CZZ having a similar result. To determine the best metal-hBN loading, the space time yield, which takes methanol selectivity in Fig 4.20 (a) and CO_2 conversion in Fig 4.20 (b)

doi:10.6342/NTU202403130

into account, is calculated using Equation 3-4. In Fig 4.20 (c), 40CZZ_hBN shows the best space time yield for methanol synthesis via CO_2 hydrogenation followed by 30CZZ_hBN and CZZ. This result also aligns with the BET from chapter 4.1.5 result where 40CZZ_hBN has the largest area and thus has more reaction-ready surface, followed by 30CZZ_hBN and CZZ. Furthermore there is a decline in 30CZZ_hBN CO_2 conversion which could indicate that the active site has been used faster that 40CZZ due to the lower metal loading.

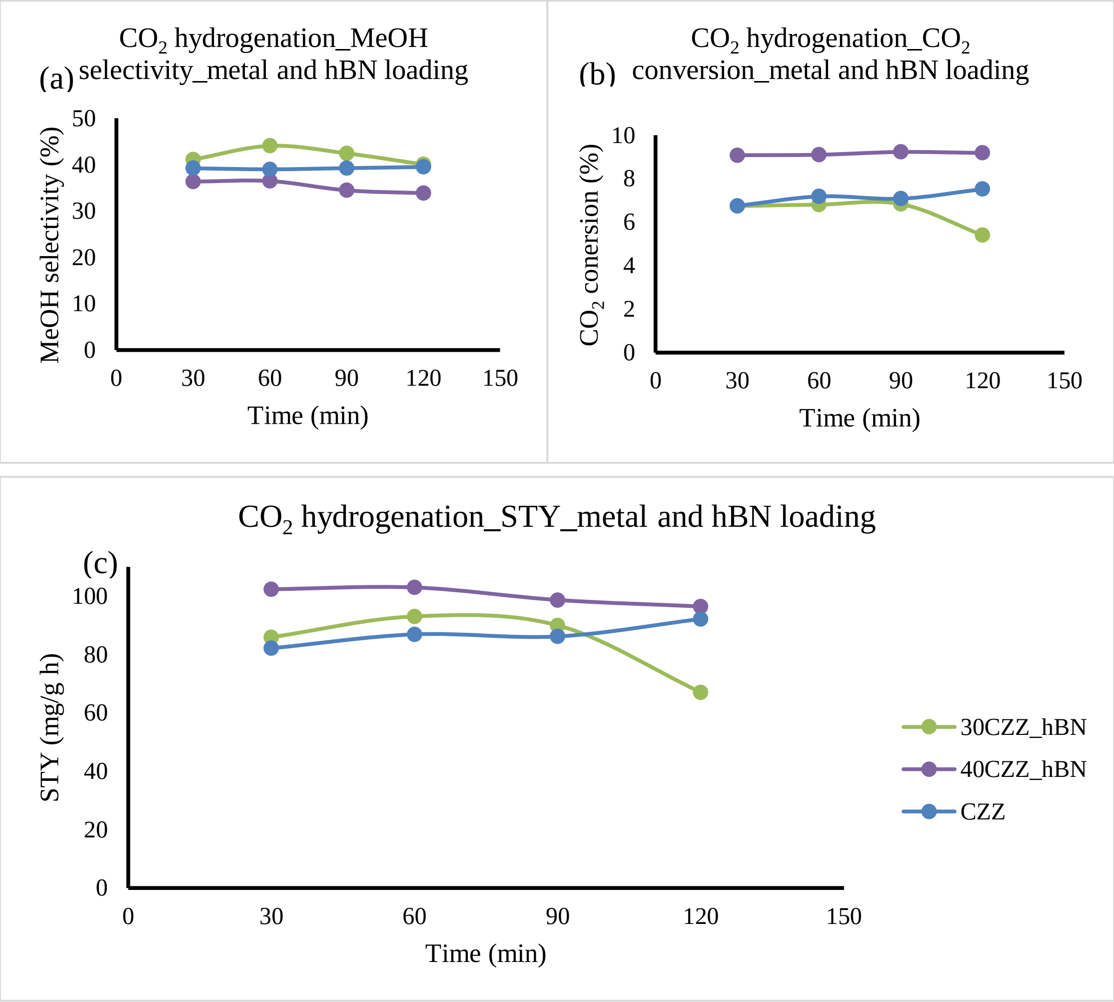

Fig. 4.20 The (a) methanol selectivity, (b) CO_2 conversion and (c) space time yield of methanol synthesis via CO_2 hydrogenation with different metal loading w/ and w/o hbN loading with operating condition of T = 230°C, P = 10 bar, CO_2/H_2 = 20/80 sccm, catalyst loading = 0.5 g, GHSV = 6131 h^{-1}

4.2.2 Temperature Effect (CO_2 Hydrogenation)

The conversion of CO_2 and the selectivity of methanol during CO_2 hydrogenation will be affected by temperature. From the thermodynamics property, CO_2 hydrogenation has a negative enthalpy which means this reaction is favorable in low temperature. As seen in Fig 4.22, at 10 bar using 40CZZ_hBN catalyst, methanol selectivity shown in Fig 4.22 (a) has a high value at low temperature but has a low conversion as shown in Fig 4.22 (b). On the other hand, increasing temperature will promote CO_2 conversion but decrease the methanol selectivity, as reverse water gas shift will start to occur at high temperature, producing more CO. The best space time yield occurs at 230 °C reaction temperature as seen in Fig 4.22 (c).

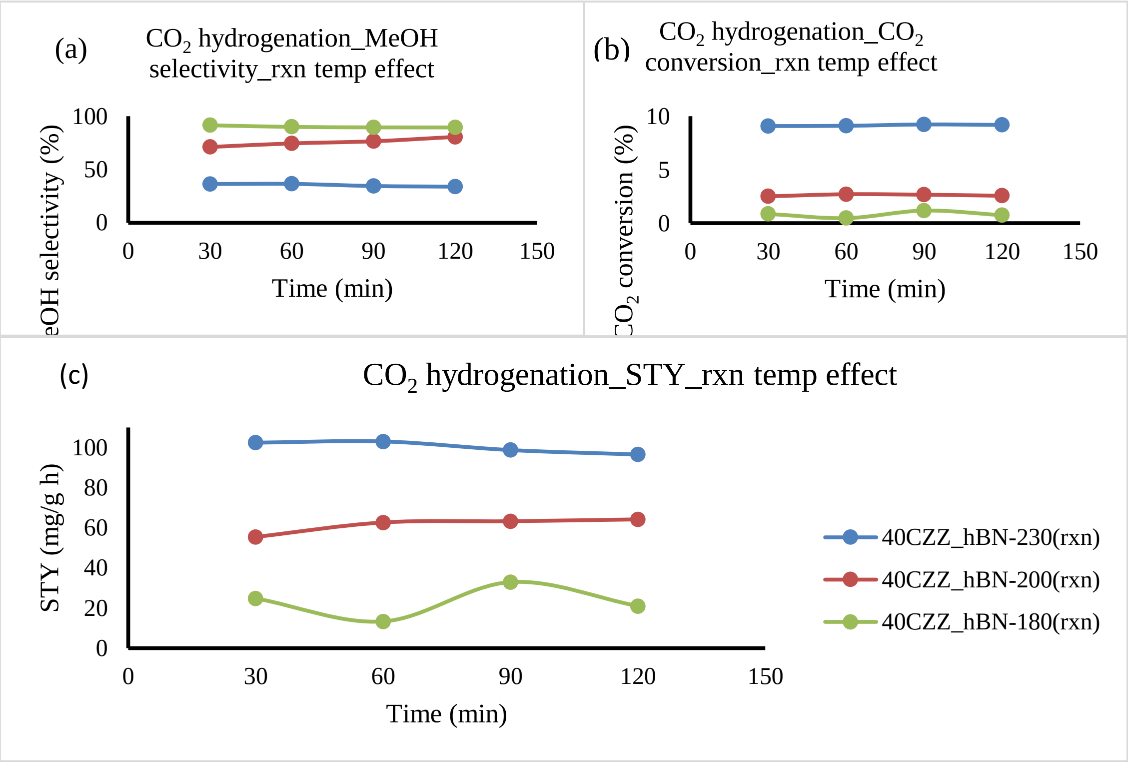

Fig. 4.21 The (a) methanol selectivity, (b) CO_2 conversion and (c) space time yield of methanol synthesis via CO_2 hydrogenation with different temperature using 40CZZ_hBN catalyst with operating condition of T = 180 °C /210°C / 230°C, P = 10 bar, CO_2/H_2 = 20/80 sccm, catalyst loading = 0.5 g, GHSV = 6131 h^{-1}

4.2.3 Promoter Effect (CO_2 Hydrogenation)

Promoter can be used to increase the performance of the catalyst by increasing a certain parameter, such as surface area, basicity, and oxygen vacancy. The result of four different promoter (La, Ce, Mo, and W) in CZZ based catalyst compared to the commercial catalyst and CZZ is presented below. As seen from the previous result, only 40% metal loading with hBN is used to compare the performance as it has a better result to catalyst without hBN loading. The operating condition for CO_2 hydrogenation 230 ^oC and 10 bar.

Fig 4.21 shows the catalytic performance evaluation with different promoter. The methanol selectivity from Fig 4.21 (a) ranked from the best to the worst is 40CZZW_hBN > 40CZZM_hBN > 40CZZL_hBN > 40CZZC_hBN > 40CZZ_hBN > commercial. Interestingly, the commercial catalyst requires more time to reach a steadier state indicating the commercial catalyst requiring more time to start to produce more methanol The CO_2 conversion shown in Fig 4.21 (b) ranked from the best to the worst is 40CZZC_hBN > commercial, 40CZZ_hBN > 40CZZL_hBN > 40CZZW_hBN >40CZZM_hBN. As the reaction time increase, 40CZZL_hBN and 40CZZM_hBN will start to convert less CO_2 due to having a lower surface area than 40CZZC_hBN and 40CZZW_hBN. Finally, the space time yield in Fig 4.21 (c) shows that 40CZZC_hBN and 40CZZW_hBN shows a better space time yield compared to the commercial copper based methanol synthesis catalyst, with 40CZZC_hBN having the highest space time yield at 140 mg/g h. This phenomena can be linked to the XPS result shows 40CZZC_hBN contains Ce^{3+} that will increase the oxygen vacancy it increases the CO_2 adsorption to the catalyst surface. As such, 40CZZC_hBN will be used as a candidate for the catalyst on the second reactor in the CAMERE reaction.

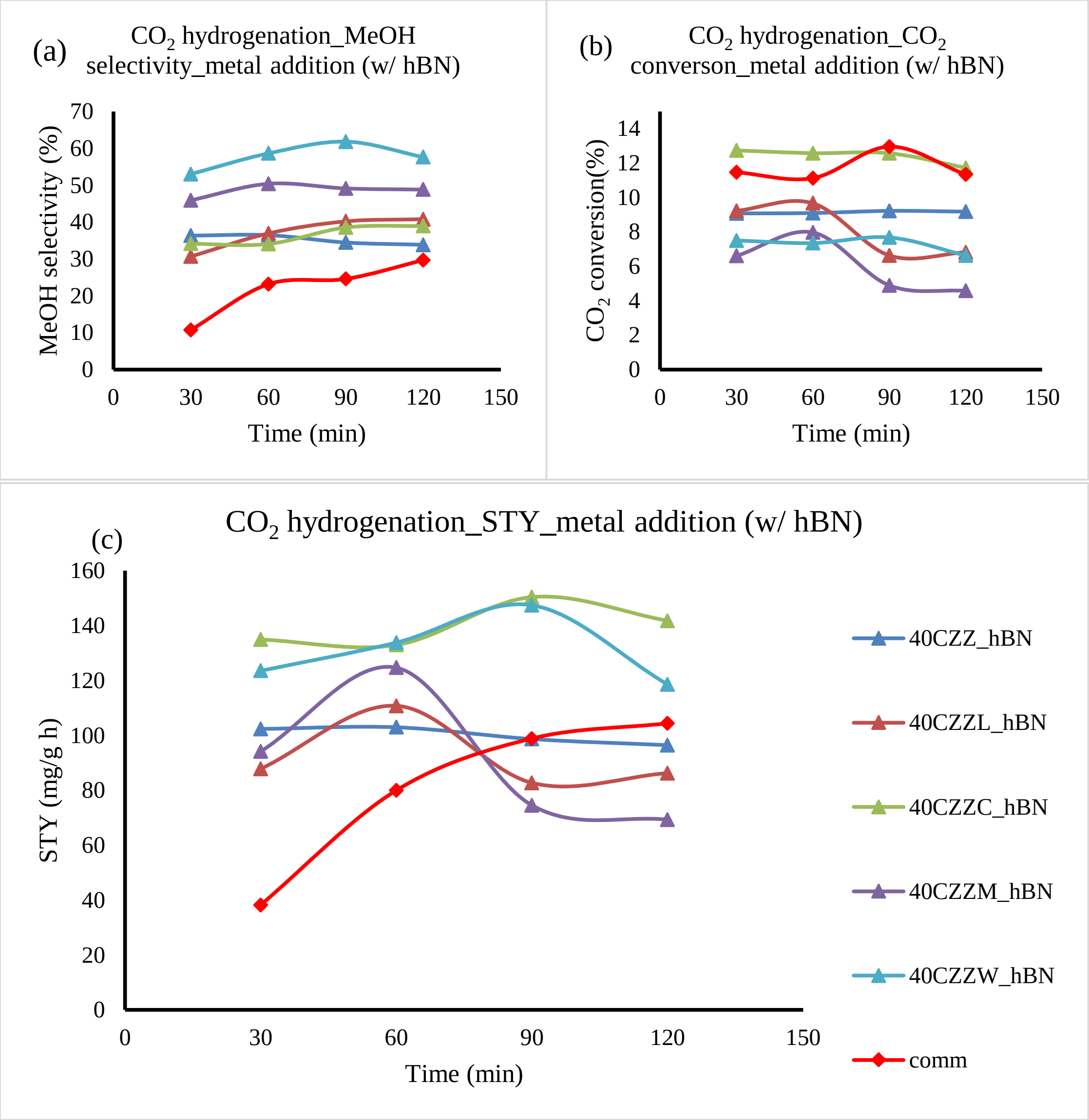

Fig. 4.22 The (a) methanol selectivity, (b) CO_2 conversion and (c) space time yield of methanol synthesis via CO_2 hydrogenation with different promoter compared to the commercial catalyst operating condition of T = 230°C, P = 10 bar, CO_2/H_2 = 20/80 sccm, catalyst loading = 0.5 g, GHSV = 6131 h^{-1}

4.2.4 Pressure Effect (CO_2 Hydrogenation)

The other important operating parameter for CO_2 hydrogenation is pressure, as shown in the chemical reaction of CO_2 hydrogenation.

CO_2 Hydrogenation: $CO_2 + 3H_2 \rightarrow CH_3OH + H_2O$ (Liu et al., 2023).

$$\Delta H = -49.5 \text{ kJ/mol}$$

According to the chemical equilibrium, increasing the pressure will shift the reaction to the side of reaction with less gas (in this case the reactant to product). As such, pressure plays an important role in increasing the methanol yield as seen from the data below. From Fig 4.23, using 0.8 g of 40CZZC_hBN catalyst at 230^{o}C, which differs in weight compared to the amount used in chapter 4.2.3 resulting in a lower GHSV, it is shown that increasing the pressure will significantly increase the methanol selectivity as presented in Fig 4.23 (a) from 52.31% at 10 bar to 77.99% at 30 bar and CO_2 conversion shown in Fig 4.23 (b) from 8.74% at 10 bar to 15.06% at 30 bar , thus increasing the space time yield from 88.26 mg/g_{cat} h at 10 bar to 227.94 mg/g_{cat} h at 30 bar as shown in Fig 4.23 (c).

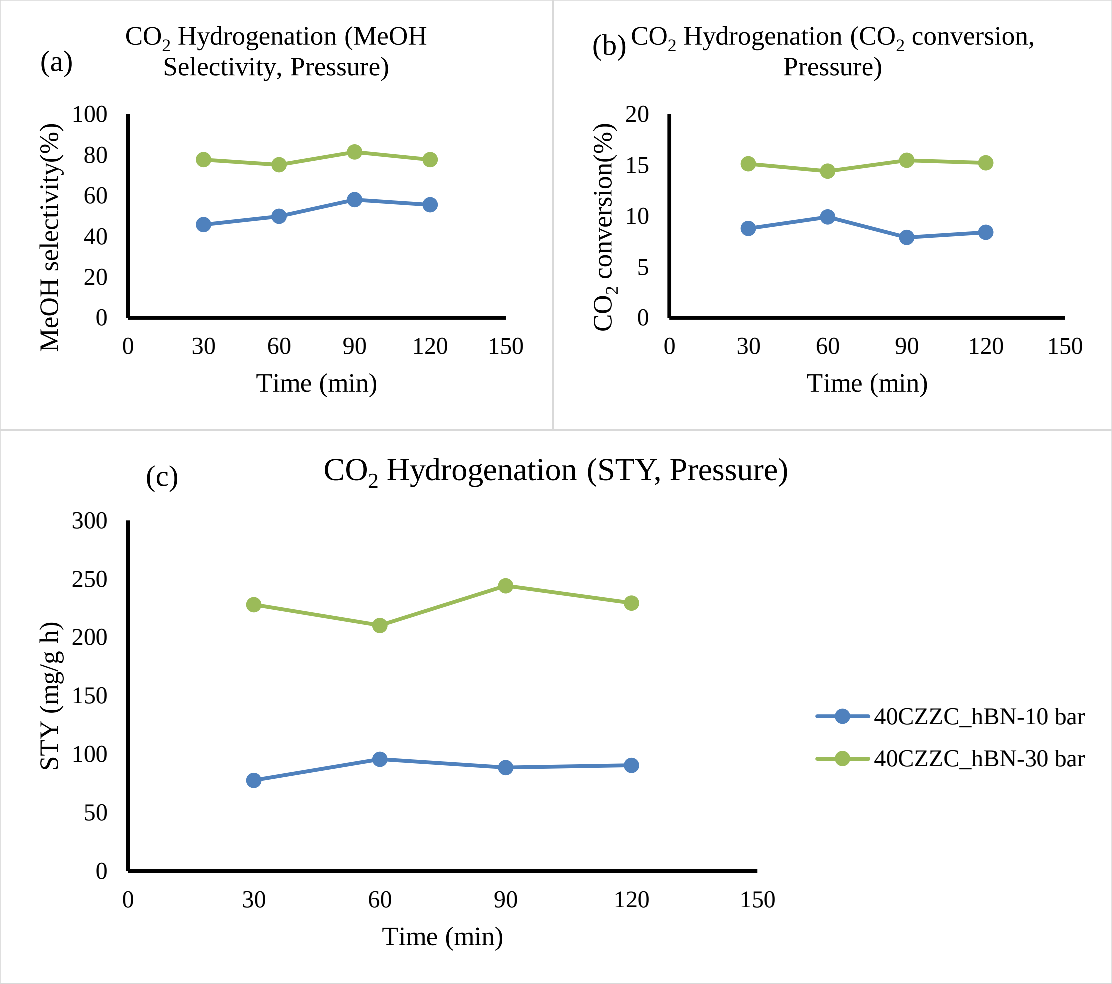

Fig. 4.23 The (a) methanol selectivity, (b) CO_2 conversion and (c) space time yield of methanol synthesis via CO_2 hydrogenation with different pressure using 40CZZC_hBN catalyst at T = 230°C, P = 10 bar and 30 bar, CO_2/H_2 = 20/80 sccm, catalyst loading = 0.8 g, GHSV = 3832 h^{-1}

4.2.5 Metal and hBN Loading Effect (CO Hydrogenation)

Fig 4.24 shows the catalytic performance effect of CO hydrogenation to methanol. CO hydrogenation is tested as it is a possible reaction that will occur in the CAMERE reaction. Same with CO_2 hydrogenation, the effect of hBN addition is also studied to see if it will enhance the methanol production in CO hydrogenation. Only 40% metal loading is tested against a catalyst without any additional hBN, with the reaction condition at

230°C and 10 bar pressure. The result shows a similar trend with CO_2 hydrogenation, where the catalyst with hBN shows a better performance compared to catalyst without hBN. The conversion of CO, as shown in Fig 4.24 (a), shows a significant improvement from using CC (0.51%) to using 40CC_hBN (2.26%). The space time yield of methanol increase from 27.42 mg/g h using CC to 62.93 mg/g h using 40CC_hBN, as seen in Fig 4.24 (b). In addition, without hBN loading, the CO conversion would decrease over time which resulted in the decrease of methanol production, show that adding hBN could increase the stability of the catalyst. The high methanol space time yield even at low CO conversion is due to the high selectivity (100%) of the product as there is no side product detected in the GC.

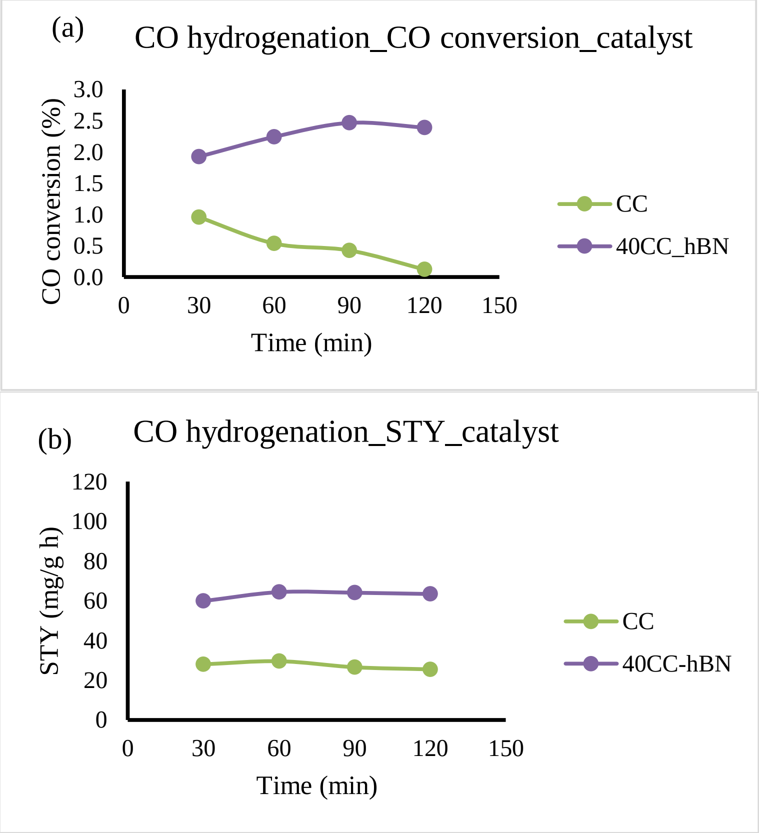

Fig. 4.24 The (a) CO conversion and (b) space time yield of methanol synthesis via CO hydrogenation with different metal loading T = 230°C, P = 10 bar, CO/H_2 = 25/75 sccm, catalyst loading = 0.5 g, GHSV = 6131 h^{-1}

4.2.6 Catalyst Type (CO Hydrogenation)

In chapter 2.4, a research on CO hydrogenation is conducted using copper-ceria catalyst, as such copper-ceria supported with hBN is tested and compared with the commercial methanol synthesis catalyst and 40CZZC_hBN. CO hydrogenation is tested at 230^{o}C and 10 bar. Fig 4.25 below shows that 40CC_hBN shows an inferior performance followed by the commercial catalyst and 40CZZC_hBN. The CO conversion in order, as shown in Fig 4.25 (a), is as follow: 40CZZC_hBN (3.62%) > commercial catalyst (2.50%) > 40CC_hBN (2.26%). The space time yield of methanol, as seen in Fig 4.25 (b), is as follow: 40CZZC_hBN (97.94 mg/g h) > commercial catalyst (91.56 mg/g h) > 40CC_hBN (62.83 mg/g h). The high methanol space time yield even at low CO conversion is due to the high selectivity (100%) of the product as there is no side product detected in the GC.

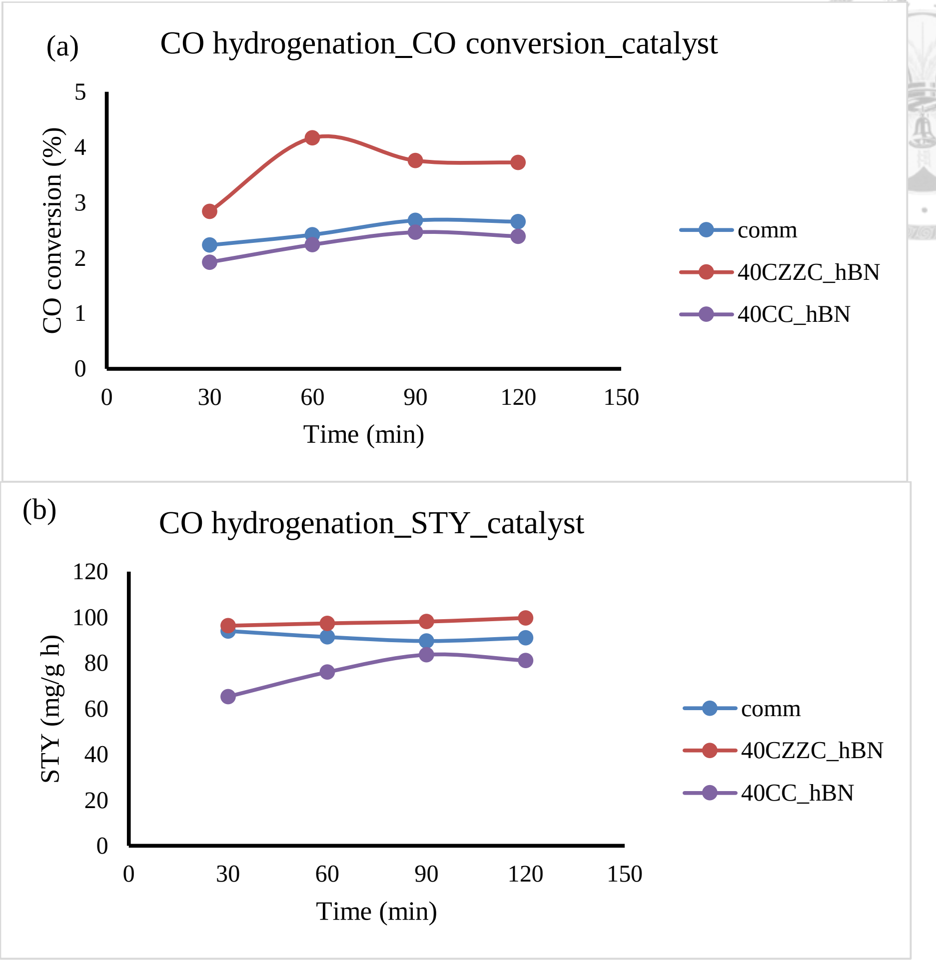

Fig. 4.25 The (a) CO conversion and (b) space time yield of methanol synthesis via CO hydrogenation with different catalyst type at T = 230°C, P = 10 bar, CO/H_2 = 25/75 sccm, catalyst loading = 0.5 g, GHSV = 6131 h^{-1}

4.2.7 Temperature Effect (RWGS)

Similar to CO_2 hydrogenation, temperature plays an important role in reverse water gas shift. Unlike CO_2 hydrogenation to methanol, pressure does not affect the reaction due the chemical equilibrium (the reactant and product has the same amount of gas), thus making temperature the most critical factor for this reaction. As reverse water gas shift is an endothermic reaction, the CO_2 conversion and CO yield will increase with elevated temperature. Fig 4.26 shows RWGS tested with CZZ catalyst at 1 bar and three different temperature (250°C, 300°C and 350°C). The result shows a significant effect on the CO_2

conversion with temperature as seen in Fig 4.26 (b), with 350°C having 31.41% CO_2 conversion compared to 250°C having only 10.25% CO_2 conversion. Additionally, methanol will start to form at 250°C which is evident with a lower selectivity of CO at 250°C seen in Fig 4.26 (a).

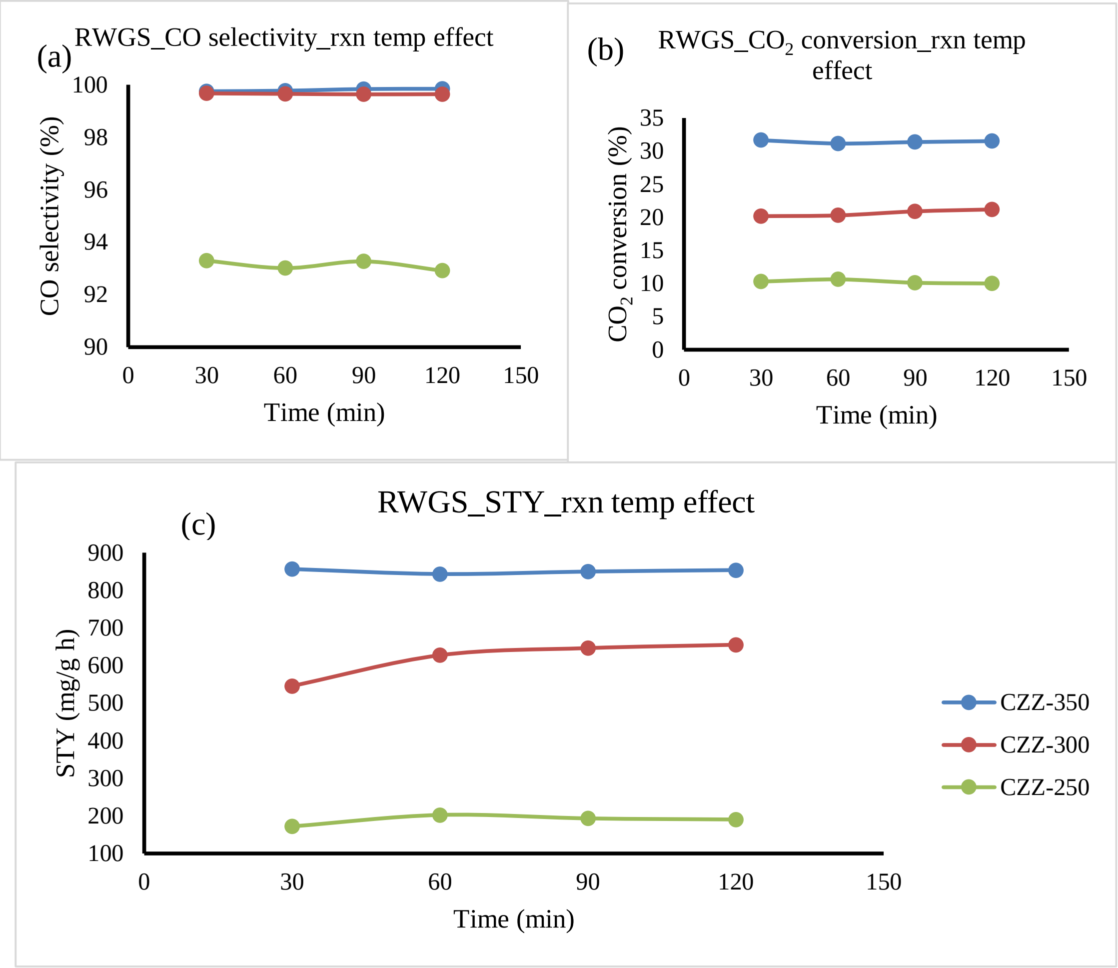

Fig. 4.26 The (a) CO selectivity, (b) CO_2 conversion and (c) space time yield of reverse water gas shift with different temperature using CZZ catalyst with operating condition of T = 250 °C /300°C / 350°C, P = 1 bar, CO_2/H_2 = 20/80 sccm, catalyst loading = 0.5 g, GHSV = 6131 h^{-1}

4.2.8 Metal and hBN Loading Effect (RWGS)

The effect on hBN loading is also tested for reverse water gas shift to see if this support can enhance the performance of reverse water gas shift, as one of the benefit of hBN support is themal stability. Fig 4.27 shows the performance of using hBN as a support in catalytic RWGS. The effect of hBN is tested with 40CZZC_hBN catalyst and CZZC catalyst at 350°C and 1 bar. The result shows that the addition of hBN will increase the CO_2 conversion from 34.67% to 37.95% seen in Fig 4.27 (b), thus improving the CO yield shown in Fig 4.27 (c) for reverse water gas shift. As hBN is a support with high thermal stability, this property will prevent further sintering of the catalyst and enhance the performance of the catalyst (Jedrzejczak-Silicka et al., 2018).

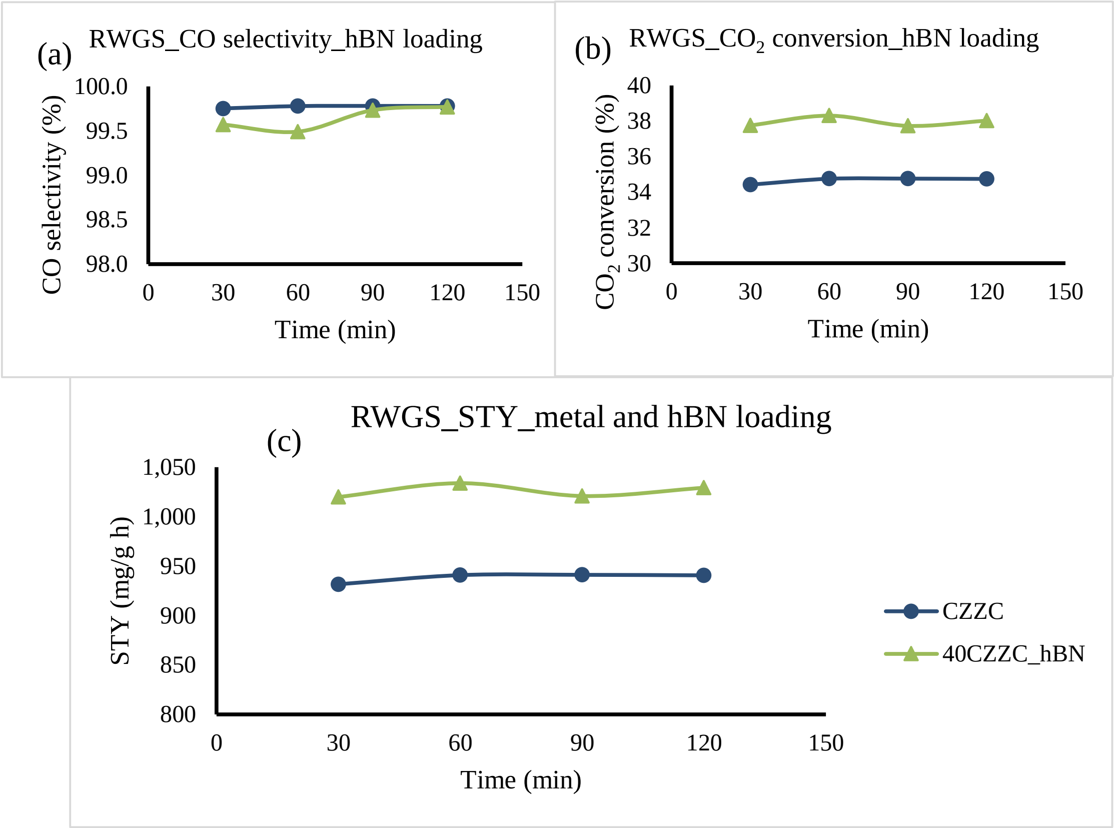

Fig. 4.27 The (a) CO selectivity, (b) CO_2 conversion and (c) space time yield of reverse water gas shift with different metal loading with operating condition of T = 350°C, P = 10 bar, CO_2/H_2 = 20/80 sccm, catalyst loading = 0.5 g, GHSV = 6131 h^{-1}

4.2.9 Promoter Effect (RWGS)

Fig 4.28 shows the effect of promoter type on the catalytic performance of RWGS. The same promoter that is being used for CO_2 hydrogenation is also tested for reverse water gas shift to observe if the effect of additional promoter can further improve the performance of reverse water gas shift. All catalyst is compared with the commercial $Cu/ZnO/Al_2O_3$ catalyst at 350^{o}C and 1 bar. The reaction test shows that 40CZZC_hBN shows the best performance followed by 40CZZL_hBN, 40CZZM_hBN, 40CZZW_hBN and the commercial catalyst from the conversion seen in Fig 4.28 (b) and space time yield of CO seen in Fig 4.28 (c). From the XPS result shows 40CZZC_hBN contains Ce^{3+} that will increase the oxygen vacancy it increases the CO_2 adsorption to the catalyst surface. 40CZZC_hBN will be used as the the catalyst in the first reactor for the CAMERE reaction, which happens to be similar to the catalyst that is used for the second reactor in the CAMERE reaction.

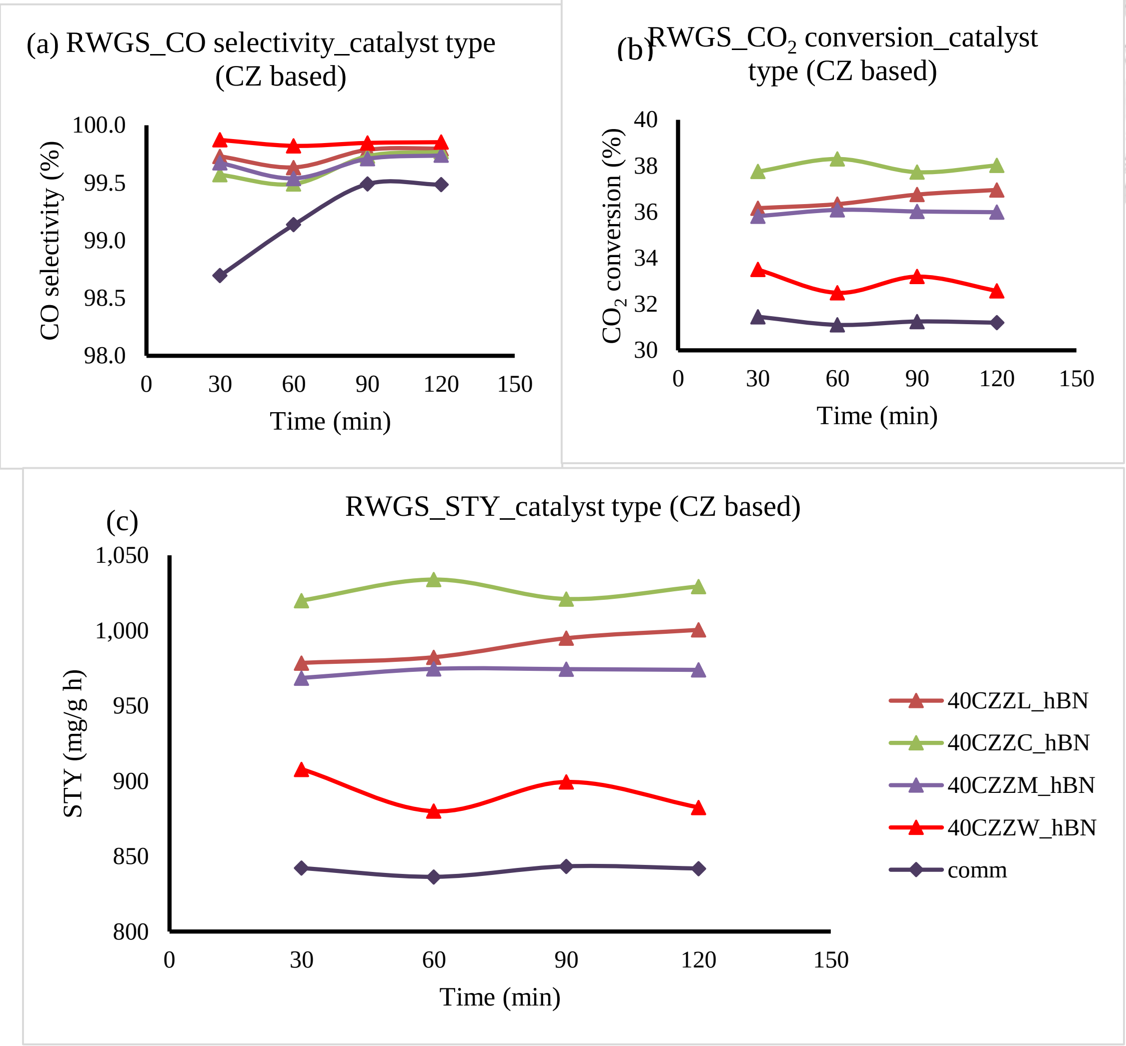

Fig. 4.28 The (a) methanol selectivity, (b) CO_2 conversion and (c) space time yield of reverse water gas shift with different promoter compared to the commercial catalyst with operating condition of T = 350°C, P = 1 bar, CO_2/H_2 = 20/80 sccm, catalyst loading = 0.5 g, GHSV = 6131 h^{-1}

4.2.10 Addition of Fe Effect (RWGS)

In chapter 2.4, a research in RWGS shows an enhancement of catalytic performance by adding Fe into a copper based catalyst. Fe in copper based catalyst can stabilize the catalyst and prevent aggregation due to high temperature sintering that will occur in copper based catalyst. However, in Fig 4.29, the addition of iron does not improve the kinetics activity of reverse water gas shift. The catalyst coprecipitated with iron has a poor performance at 350^{o}C and requires a higher reduction temperature to undergo reverse water gas shift reaction. CFC catalyst is notably the only catalyst in which hBN addition does not improve the catalytic performance. Compared to 40CZZC_hBN, CFC has an inferior performance at the same reaction temperature, at both 350^{o}C and 450^{o}C. There is two reasons of the low performance of Fe based catalyst that can be drawn from the catalyst characteristic result, which is low surface area of Fe based catalyst from BET and the CuFe alloy having a shift to high energy level for the Fe species in XPS analysis seen in Fig 4.17 (d), hindering the reaction.

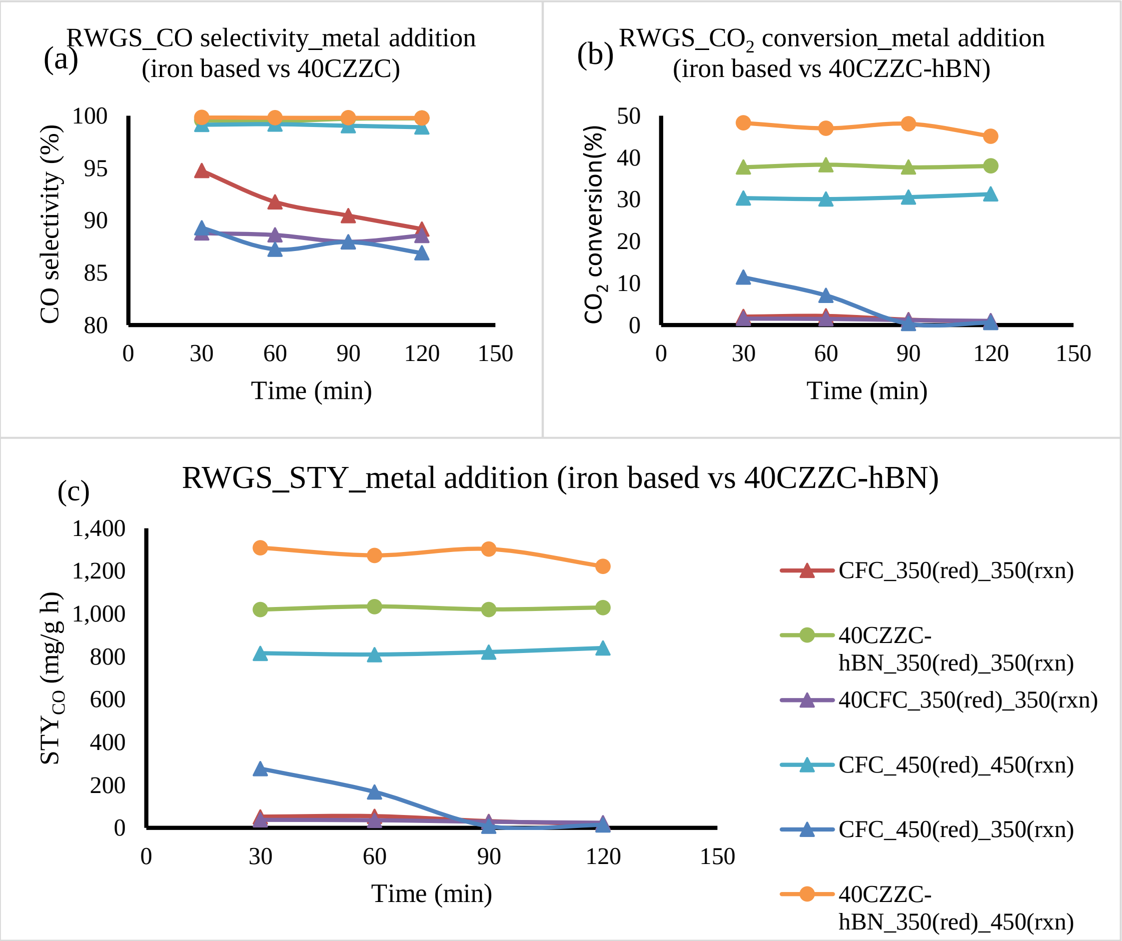

Fig. 4.29 The (a) CO selectivity, (b) CO_2 conversion and (c) space time yield of reverse water gas shift with Fe addition with operating condition of T = 350^{o}C/450^{o}C, P = 1 bar, CO_2/H_2 = 20/80 sccm, catalyst loading = 0.5 g, GHSV = 6131 h^{-1}

4.2.11 Catalyst Loading Effect (CO/CO_2 Hydrogenation)

To optimize the CAMERE reaction, the amount of catalyst loaded in the reactor is tested with 3 different weight, 0.5 g, 0.8 g, and 1.0 g. The amount of catalyst will affect the gas hourly space velocity and surface area that is available by the catalyst. All catalyst was tested using 40CZZC_hBN at 10 bar with a mixture of CO and CO_2 as the carbon source for methanol synthesis, which is done to simulate the condition for the second reaction in the CAMERE reaction. The inlet flow composition is intended to emulate the outlet of RWGS where the CO_2 at high temperature (~450^oC) reaching 50%. However, an malfunction of CO mass flow controller resulted in no flow if the flow is set below 16 sccm, as such it is the flow rate set for CO. Even so, one of the key point of this experiment is to observe the effect of catalyst loading on a system that is similar to the second reactor for CAMERE reaction.

The result in Fig 4.30 shows that 0.8 g of catalyst has the best performance for methanol synthesis, having the highest carbon conversion as shown in Fig 4.30 (a) methanol selectivity as shown in Fig 4.30 (b) and methanol space time yield as shown in Fig 4.30 (c). Interestingly, using 1.0 g of catalyst will reduce the space time yield of methanol synthesis to half compared to 0.5 g of catalyst, which means the methanol yield is similar to each other as doubling the amount of catalyst will halved the space time yield. This phenomena also shows that this catalyst has a mass transfer limitation if too much catalyst is inserted in the reactor. At higher catalyst loading, the catalyst are more likely to clump on each other in a small volume resulting in a smaller contact area for reaction. Furthermore, due to the equation used to calculate STY_{MeOH} that is shown in Equation 3-4, by doubling the amount of catalyst it can result in halving the STY_{MeOH}, especially if both scenario has a similar carbon conversion and methanol selectivity. From this result, 0.8 g of 40CZZC_hBN wil be used as the catalyst amount loaded and type of catalyst

doi:10.6342/NTU202403130

used as the second reactor for two reactor system

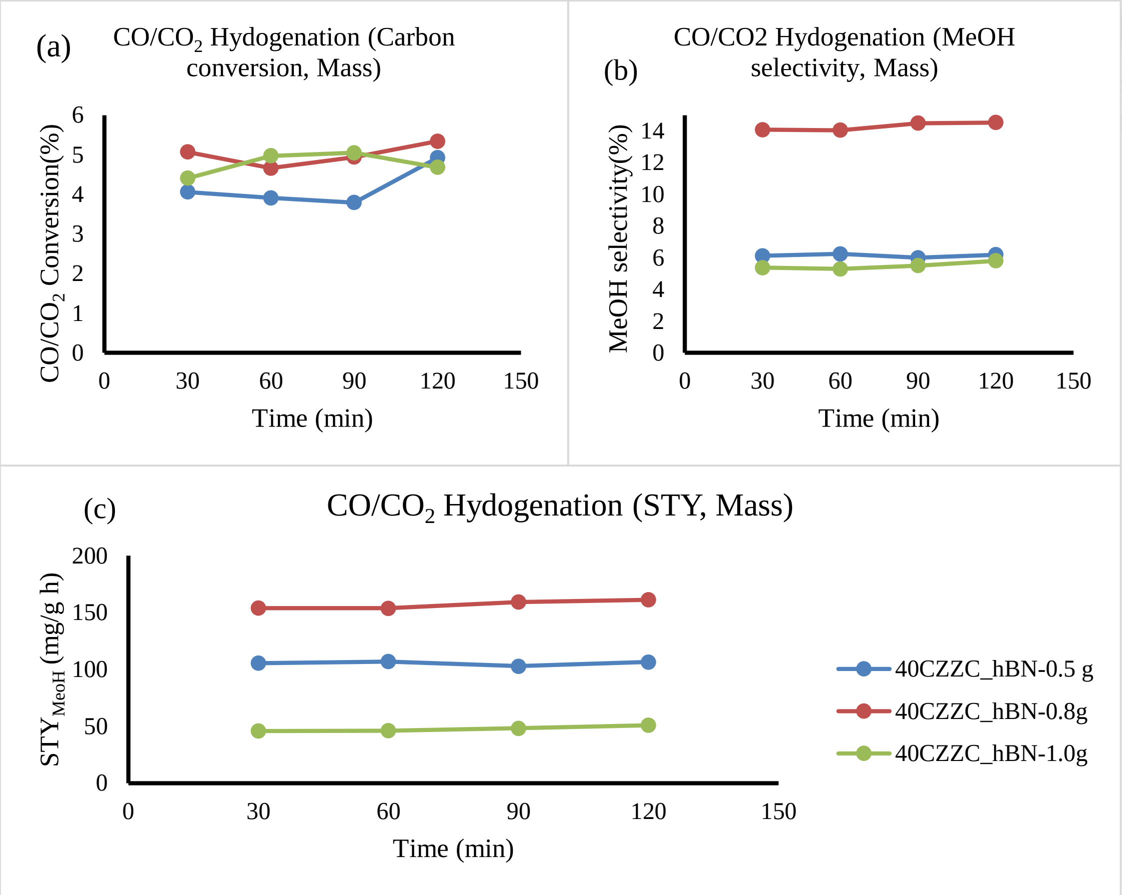

Fig. 4.30 The (a) carbon conversion, (b) methanol selectivity and (c) space time yield of reverse water gas shift with different catalyst loading with operating condition of T = 230°C, P = 10 bar, $CO/CO_2/H_2$ = 16/10/80 sccm, catalyst loading = 0.5g/0.8g/1.0g, GHSV = 6131h^{-1}/3832h^{-1}/3065h^{-1}

4.2.12 Catalyst Type Effect (CAMERE)

To determine the best catalyst for the second reactor and the main carbon source for the methanol synthesis in the second reactor, a catalyst that prefers CO_2 hydrogenation (40%CZZC_hBN) and a catalyst that prefers CO hydrogenation (40%CC_hBN) is being used as the methanol synthesis catalyst. The first reactor uses 40%CZZC_hBN as the reverse water gas shift catalyst, operating at 500°C and 10 bar using 0.5 g of catalyst. The second reactor is operated at 230°C and 10 bar using 0.8 g of catalyst. Between the two reactors, a desiccant chamber filled with molecular sieve 3A is used for water removal in between the two reactors. Even though both catalysts are calcined at lower temperature than the operating condition of RWGS in the CAMERE reaction, deactiviation is not observed as most cases will have a steady state condition or a slight increase in activity after 2 hours of reaction.

The result in Fig 4.31 shows that 40%CZZC_hBN has higher methanol selectivity shown in Fig 4.31 (a), overall CO_2 conversion shown in Fig 4.31(b), and methanol space time yield shown in Fig 4.31 (c), suggesting that the main source of carbon used for the methanol synthesis in CAMERE reaction is CO_2.

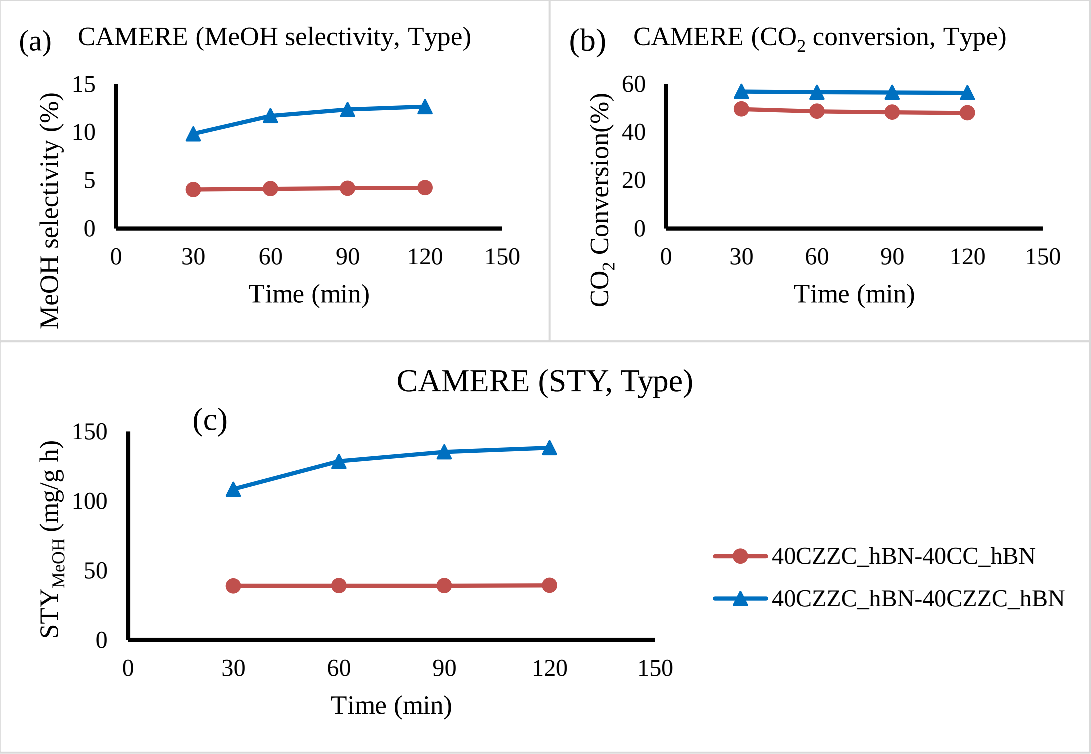

Fig. 4.31 The (a) methanol selectivity, (b) CO_2 conversion and (c) space time yield of CAMERE reaction with different type of catalyst at the second reactor with operating condition of T = 500°C (1st reactor) /230°C (2nd reactor), P = 10 bar (1st and 2nd reactor), CO_2/H_2 = 20/80 sccm, catalyst loading = 0.5 g (1st reactor) / 0.8 g (2nd reactor) GHSV = 3832 h^{-1}

doi:10.6342/NTU202403130

4.2.13 Pressure Effect (CAMERE)

Methanol synthesis is largely affected by the reaction's pressure due to the chemical equilibrium. By using 40%CZZC_hBN as the catalyst for the first and second reactor, with the operating temperature of 500°C and 230°C respectively, and molecular sieve 3A as the desiccant, the pressure is tested at 10 bar and 30 bar to observe how pressure will affect the CAMERE reaction.

As shown in Fig 4.32, by increasing the pressure, the methanol selectivity will significantly increase as seen in Fig 4.32 (a) while the CO_2 conversion shown in Fig 4.32 (b) shows an almost similar value. While the methanol selectivity of both condition is low (both condition has a selectivity lower than 30%, less than a single reactor system) due to the majority of CO_2 reacted to produce CO, at elevated pressure the production of methanol will be higher based on the chemical equilibrium, evident by the doubling of MeOH selectivity from 10 bar to 30 bar. As such, the space time yield of methanol will also increase more than twofold as illustrated in Fig 4.32 (c).

doi:10.6342/NTU202403130

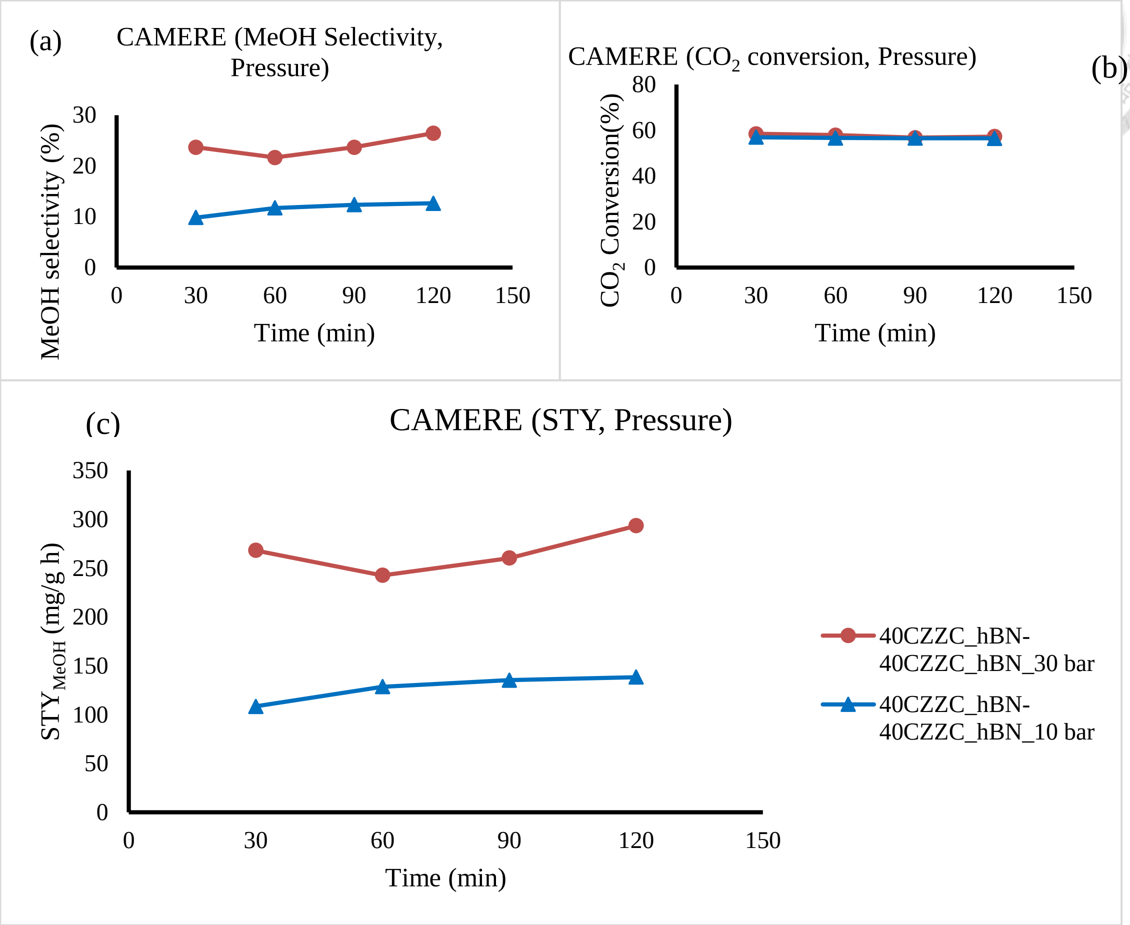

Fig. 4.32 The (a) methanol selectivity, (b) CO_2 conversion and (c) space time yield of CAMERE reaction with different pressure with operating condition of T = 500°C (1st reactor) /230°C (2nd reactor), P = 10 bar (1st and 2nd reactor), CO_2/H_2 = 20/80 sccm, catalyst loading = 0.5 g (1st reactor) / 0.8 g (2nd reactor) GHSV = 3832 h^{-1}

4.2.14 Desiccant Type Effect (CAMERE)

Lastly, the effect of desiccant type is observed to see which desiccant is more suitable for water removal in CAMERE reaction. Two types of water desiccant is utilized, molecular sieve 3A and $CaCl_2$. Molecular sieve 3A is often used as a selective water desiccant as the molecular size of water (2.7 Å) is smaller than the pore sized of molecular sieve 3A (which is around 3Å). $CaCl_2$ is a drying agent that is commonly used to dehumidify a room or chamber.

As shown in Fig 4.33, molecular sieve 3A shows a better performance for water removal, as seen by the methanol selectivity as seen in Fig 4.33 (a) and CO_2 conversion as seen in Fig 4.33 (b), increasing the methanol yield as seen in Fig 4.33 (c) for the CAMERE reaction compared to $CaCl_2$.

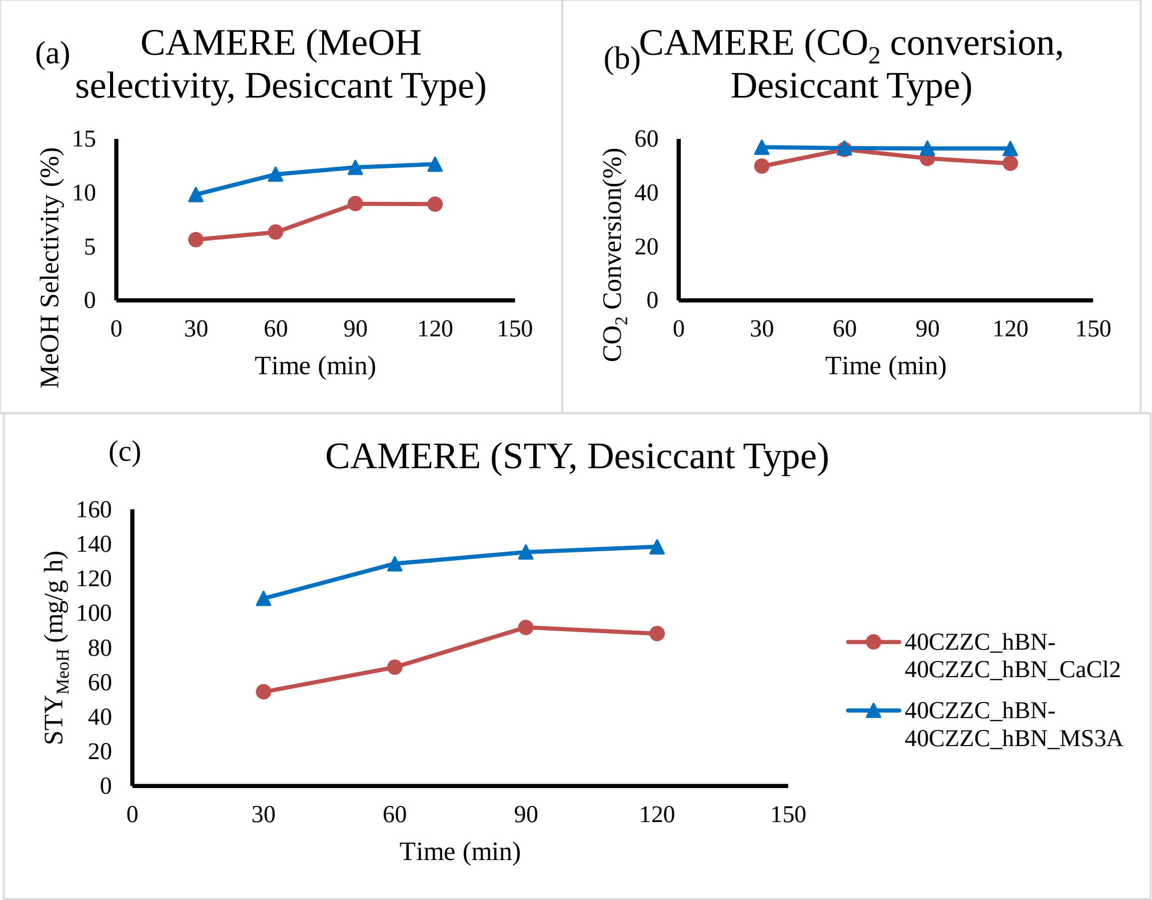

Fig. 4.33 The (a) methanol selectivity, (b) CO_2 conversion and (c) space time yield of CAMERE reaction with different desiccant with operating condition of T = 500°C (1st reactor) /230°C (2nd reactor), P = 10 bar (1st and 2nd reactor), CO_2/H_2 = 20/80 sccm, catalyst loading = 0.5 g (1st reactor) / 0.8 g (2nd reactor) GHSV = 3832 h^{-1}

4.2.15 1 Reactor Compared to 2 Reactors (and reaction type in the first reactor)

The performance of 1 reactor is compared with the performance of two reactors to observe the feasibility of utilizing two reactors for CO_2 hydrogenation to methanol. Due to the fact that the CAMERE reaction uses the same catalyst for two reactions and the minimal effect of CO to methanol synthesis as seen in a very low selectivity, the CAMERE reaction is also compared with 2 CO_2 hydrogenation to methanol reactor in series, with water being removed midway (similar to CAMERE). The result is studied using 0.5 grams of 40CZZC_hBN in the first reactor and 0.8 grams of 40CZZC_hBN catalyst in the second reactor at 10 bar and 230^oC for the CO_2 hydrogenation to methanol (the first reactor for CAMERE has an operating temperature of 500^oC while the first reactor for 2 CO_2 hydrogenation to methanol in series has an operating temperature of 230^oC).

The result in Fig 4.34 shows that both 2 reactors has a better performance compared to the single reactor. The CAMERE reaction has the highest CO_2 conversion (Fig 4.34 (b)) due to the operating temperature at the first reactor (high temperature will lead to high CO_2 conversion) but poor selectivity shown in Fig 4.34 (a) due to the majority of CO_2 being converted to CO. While the single reactor and two reactor in series have similar methanol selectivity as shown in Fig 4.34 (a), the conversion seen in Fig 4.34 (b) at the two reactor series doubled compared to the single reactor due to some CO_2 having been converted into CO and methanol beforehand. In addition, all two reactor systems has a water removal in between the reactor which not only prevents catalyst deactivation but also shift the chemical equilibrium to the product side. Overall, the best perfoming reaction is the 2 CO_2 hydrogenation to methnaol in series with a methanol space time yield of 177.27 mg/g h as seen in Fig 4.34 (c). The result is also being compared to the equilibrium result calculated using Aspen Plus. While the conversion of the two reactor system is similar to the equilibrium of two reactor in series, the selectivity and STY of the reactor in series system is better than the equilibrium calculation.

doi:10.6342/NTU202403130

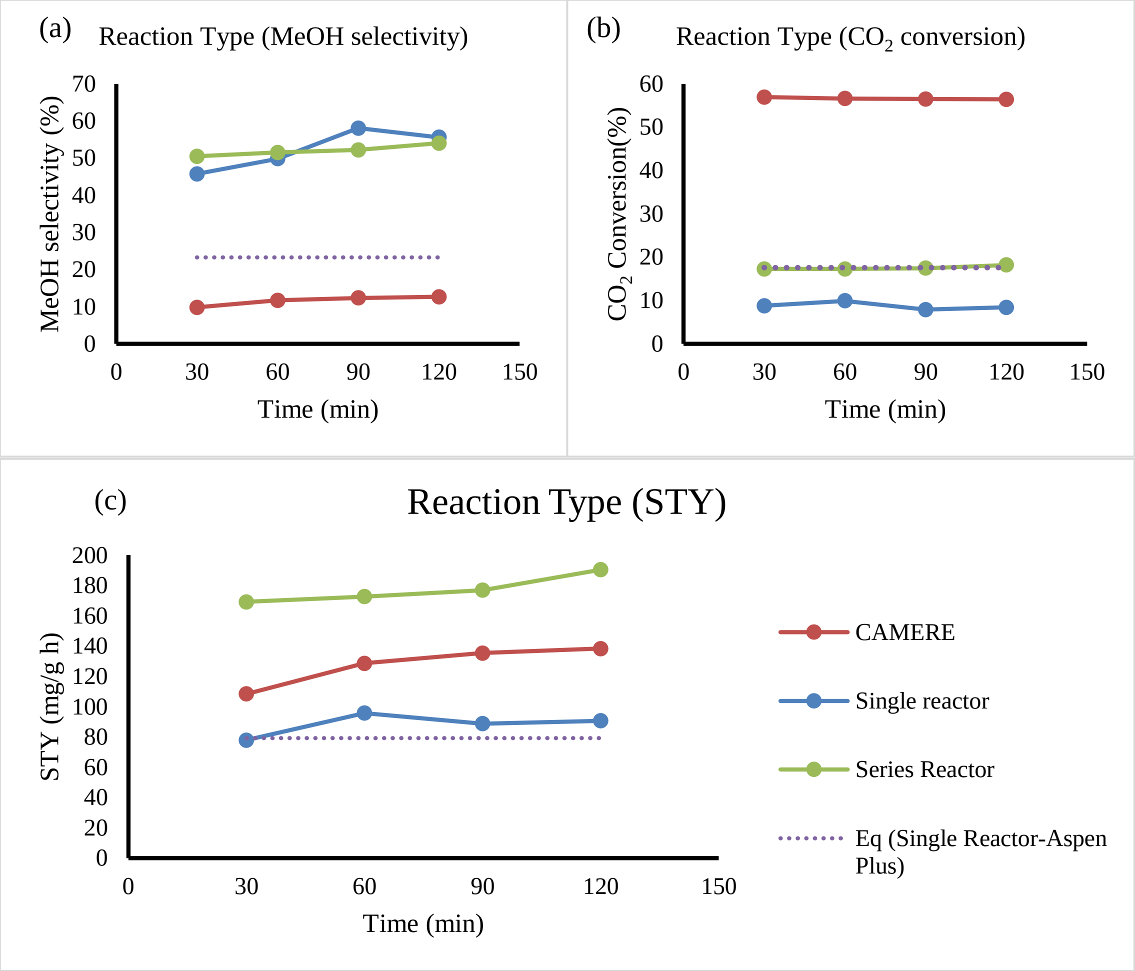

Fig. 4.34 The (a) methanol selectivity, (b) CO_2 conversion and (c) space time yield of 1 reactor compared to 2 reactors (CAMERE and 2 CO_2 hydrogenation to methanol in series) with operating condition of T = 500°C (1st reactor CAMERE) /230°C (single reactor,2nd reactor CAMERE, both reactor in series), P = 10 bar (1st and 2nd reactor), CO_2/H_2 = 20/80 sccm, catalyst loading = 0.5 g (1st reactor) / 0.8 g (2nd reactor) GHSV = 6131 h^{-1}(single reactor) / 3832 h^{-1} (CAMERE and reactor in series)

4.2.16 Pressure Effect (2 CO2 Hydrogenation to Methanol in Series)

As pressure provides a significant boost of methanol yield for CO_2 hydrogenation to methanol, the effect of pressure is also tested to observe the improvement of the reaction. The reaction is tested using 0.8 g 40CZCC_hBN catalyst in the second reactor and the

doi:10.6342/NTU202403130

operating temperature for both reactor is 230°C.

The result in Fig 4.35 shows that increasing the pressure will increase the methanol selectivity in Fig 4.35 (a) from 52.06% at 10 bar to 65.37% at 30 bar, the CO_2 conversion shown in Fig 4.35 (b) from 17.54% at 10 bar to 26.02% at 30 bar and the space time yield shown in Fig 4.35 (c) from 177.27 mg/g_{cat} h at 10 bar to 337.58mg/g_{cat} h at 30 bar). The space time yield for 2 CO_2 hydrogenation to methanol in series also shows the highest space time yield overall at 337.58 mg/g_{cat} h. While the result shows a room for improvement in CO_2 conversion compared to the equilibrium result from Aspen Plus, the selectivity and STY shows a better result.

doi:10.6342/NTU202403130

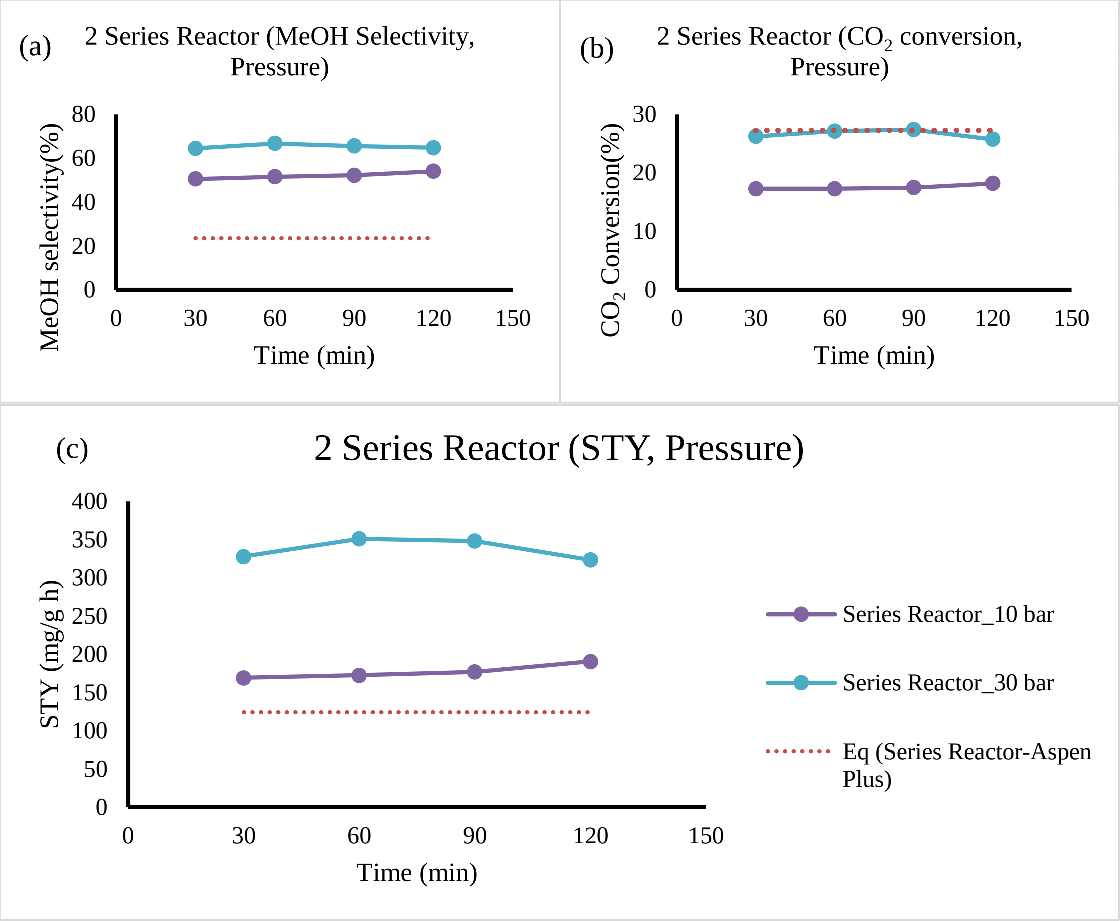

Fig. 4.35 The (a) methanol selectivity, (b) CO_2 conversion and (c) space time yield of 2 CO_2 hydrogenation to methanol in series reaction with different pressure with operating condition of T = 230°C (both reactor in series), P = 10 and 30 bar (1^{st} and 2^{nd} reactor), CO_2/H_2 = 20/80 sccm, catalyst loading = 0.5 g (1^{st} reactor) / 0.8 g (2^{nd} reactor) GHSV = 3832 h^{-1} (reactor in series)

4.2.17 Addition of Zn and Zr (CO_2 Hydrogenation, CO Hydrogenation, CAMERE)

To summarize the overall reaction for methanol synthesis, 40CZZC_hBN and 40CC_hBN performance is being compared for three methanol synthesis reaction. The summary of 40CZZC_hBN catalytic performance is shown in Fig 4.36. 40CZZC_hBN shows a better performance when there is CO_2 present in the feed, as shown in Fig 4.36

(a) where the three highest carbon conversion are reactions with CO_2 present as feed and Fig 4.36 (b) with the high STY of CAMERE reaction, and CO_2 hydrogenation to methanol in reactor series with the latter having the highest space time yield. The CO hydrogenation methanol space time yield appears slightly higher than CO_2 hydrogenation due to the different catalyst loading, with CO_2 hydrogention being conducted with 0.8 g and CO hydrogenation being conducted with 0.5 g. The result from both figures in Fig 4.36 shows that 40CZZC_hBN prefers methanol synthesis via CO_2 hydrogenation

Fig 4.37 shows the comparison of 40CC_hBN catalytic performance for methanol synthesis. 40%CC_hBN has poor performance at the presence of CO_2 as seen Fig 4.37 (b) with space time yield of 40CZZC_hBN being 1 order of magnitude higher than 40CC_hBN for CO_2 hydrogenation and 40CC_hBN performs better with only CO in the feed as seen in Fig 4.37 (b). However, CO hydrogenation STY using 40CC_hBN is lower than CO hydrogenation using 40%CZZC_hBN, suggesting that CO hydrogenation is not the preferred route for methanol synthesis. While the CAMERE reaction shows a good performance for methanol synthesis, the presence of carbon monoxide is ultimately trivial for methanol synthesis. This experiments also confirms the study done by Studt et al. in 2015 where the presence of Zn will provide the Cu-Zn synergy that assist the production of methanol using CO_2, while the absence of Zn will cause it to prefer CO hydrogenation.

doi:10.6342/NTU202403130

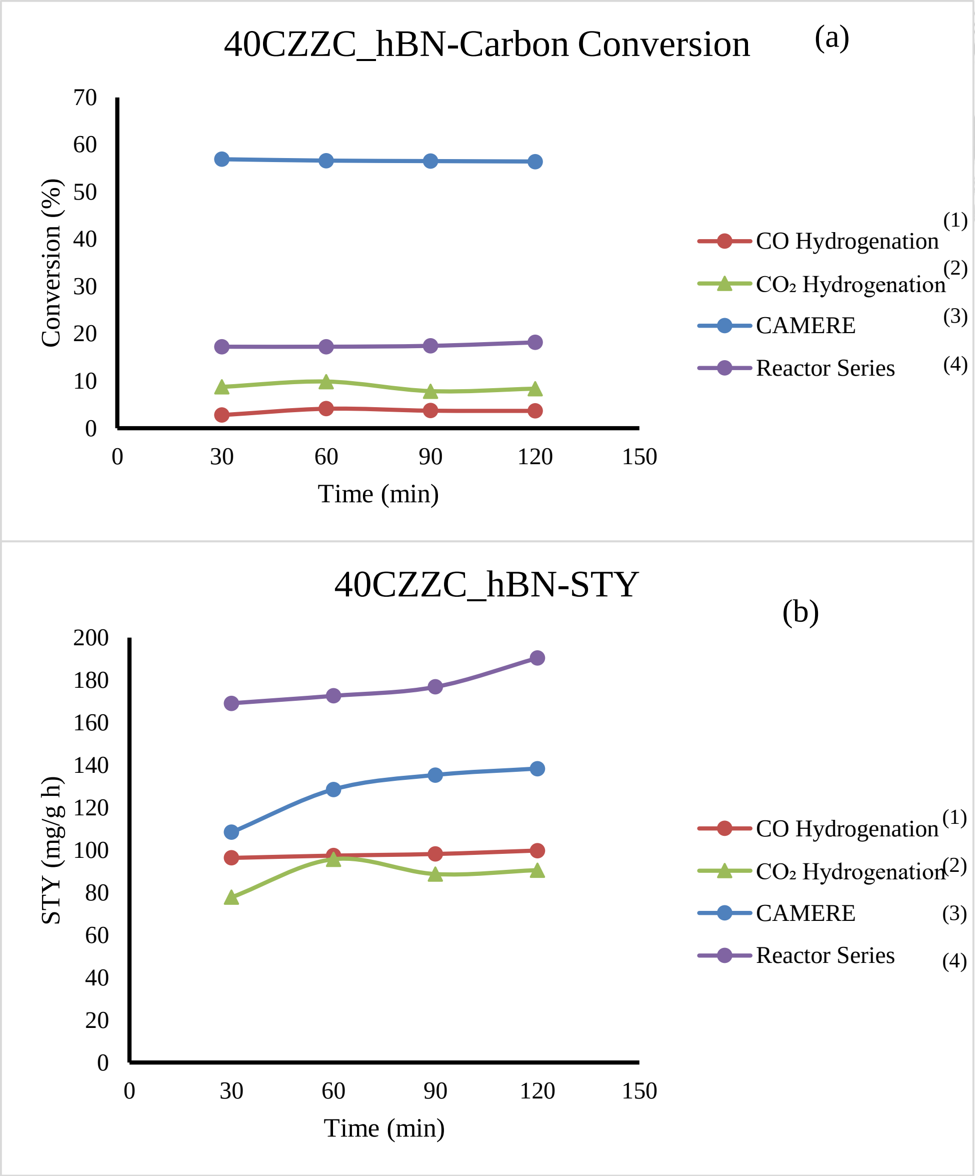

Fig. 4.36 The (a) carbon conversion and (b) space time yield of methanol synthesis via CO_2 hydrogenation, CAMERE, and CO hydrogenation with 40CZZC_hBN catalyst with the condition of (1) T=230°C, P=10 bar, catalyst loading 0.8 g, GHSV=3832 h^{-1}, (2) T = 500°C (1st reactor) /230°C (2nd reactor), P = 10 bar, catalyst loading 0.5 g (1st reactor) / 0.8 g (2nd reactor), GHSV=3832 h^{-1}, (3) T=230°C, P=10 bar, catalyst loading 0.5 g, GHSV=6131 h^{-1}, (4) T = 230°C (1st and 2nd reactor), P = 10 bar (1st and 2nd reactor), catalyst loading 0.5 g (1st reactor)/ 0.8 g (2nd reactor), GHSV=3832 h^{-1}

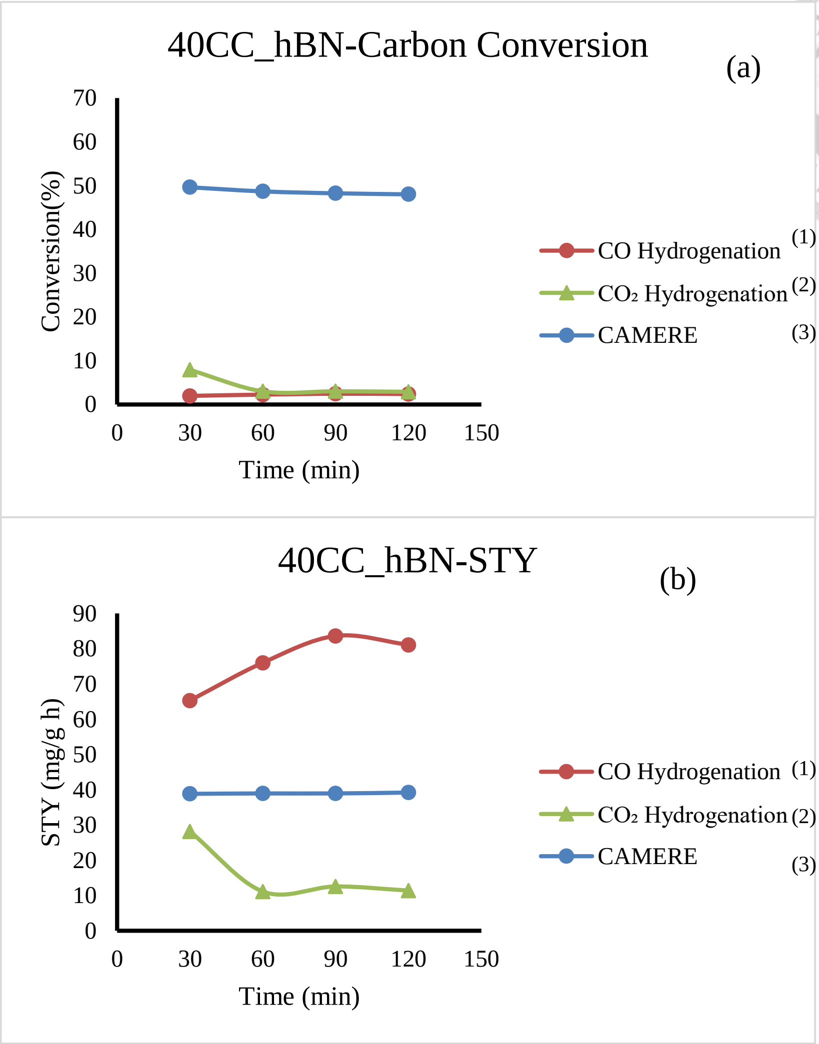

Fig. 4.37 The (a) carbon conversion and (b) space time yield of methanol synthesis via CO_2 hydrogenation, CAMERE, and CO hydrogenation with 40CC_hBN catalyst $^{(1)}$ T=230°C, P=10 bar, catalyst loading 0.5 g, GHSV=6131 h^{-1}, $^{(2)}$ T = 500°C (1st reactor) /230°C (2nd reactor), P = 10 bar (1st and 2nd reactor), catalyst loading 0.5 g (1st reactor) / 0.8 g (2nd reactor), GHSV=3832 h^{-1}, $^{(3)}$ T=230°C, P=10 bar, catalyst loading 0.5 g, GHSV=6131 h^{-1}

4.3 State of the Art

Table 4.6 showed a comparison of several past research on CO_2 hydogenation to methanol using different catalys and condition compared to this research. Our research demonstrated that hBN supported Cu/Zn catalyst gave superior performance over other studies.

Table 4.6 State of the art on the topic of CO_2 hydrogenation to methanol

Catalyst	GHSV (/h)	Pressure (bar)	Temperature (°C)	CO_2 conv. (%)	MeOH sel. (%)	STY (mg/ g_{cat} h)	Reference
CuZnZrCe	-	30	230	22.8	53.0	102.53	Ban et al., 2014
PdZn/CeO_2	2400	20	220	14	95	114	Ojelade & Zaman, 2019
Cu/CeO_2	-	30	250	1	53	45	Zhu et al., 2020
Cu/ZnO–activated carbon	3000	31	240	5	28.92	71.08	Xie et al., 2023
CuZnO/n-Al_2O_3	7800	30	300	19.8	58.5	41.97	Wang et al., 2022
15Cu/6.4ZnO/ AlFum MOF	10000	50	230	45	88	51.8	Duma et al., 2022

Table 4.6 State of the art on the topic of CO_2 hydrogenation to methanol (cont.)

Catalyst	GHSV (/h)	Pressure (bar)	Temperature (°C)	CO_2 conv. (%)	MeOH sel. (%)	STY (mg/ g_{cat} h)	Reference
Cu/Zno/CeO_2 @ MOF-5	-	10	250	11	79	23.3	Vali et al., 2024
Cu/ZnO/Al_2O_3 silylation	-	45	180	5	92.9	39.9	Cui et al., 2023
K-Ni/MoS_2/MgO	-	50	320	25	19.93	19	Jiang et al., 2023
40%-CuZnZrCe_hBN	**3831**	**30**	**230**	**15.06**	**77.99**	**227.94**	**This work**
40%-CuZnZrCe_hBN (CAMERE)	**3831**	**30**	**500 / 230**	**57.54**	**23.85**	**266.11**	**This work**
40%-CuZnZrCe_hBN (2 reactor series)	**3831**	**30**	**230 (both)**	**26.62**	**65.37**	**337.58**	**This work**

While the performance of 40CZZC_hBN in 2 reactor series system is better than several literature result, the performance is still inferior to an industrial case where the STY_{MeOH} can reach up to 1.8 kg_{MeOH}/l_{cat} due to the usage of higher pressure (75 bar) and recycle flow of 5100 m^3_N/t MeOH (Wurzel, 2006).

CHAPTER V

CONCLUSION

5.1 Conclusion

1. Loading a metal catalyst with hBN will improve its performance in CO_2 hydrogenation, reverse water gas shift, and CO hydrogenation. The addition of promoter can improve CZZ based catalyst and cerium is shown to have the best performance for CO_2 hydrogenation, reverse water gas shift, and CO hydrogenation.
2. The optimal temperature for CO_2 hydrogenation to methanol is 230^{o}C and increasing the pressure will improve the methanol synthesis. Reverse water gas shift on the other hand is not affected by pressure and will have improved performance with increasing temperature.
3. The surface area, electron configuration of the elements on the surface, reducibility, and number of basic site contributes to the catalytic performance.
4. Two reactors will have a better performance for CO_2 hydrogenation to methanol compared to single reactors. By conduction 2 CO_2 hydrogenation to methanol reactions in series, it will have a higher methanol yield (STY = 337.58 mg/g_{cat} h at 30 bar) compared to CAMERE reaction (STY = 266.11 mg/g_{cat} h at 30 bar).

5.2 Suggestion

1. Study the usage and effect of recycle stream to increase the CO_2 conversion on the reactor system
2. Study the effect of promoter ratio to observe the difference in methanol space time yield

REFERENCE

Abdullah, Avin & Mohammed, Azad. (2019). Scanning Electron Microscopy (SEM): A Review.

Azhari, N. J., Erika, D., Mardiana, S., Ilmi, T., Gunawan, M. L., Makertihartha, I. G. B. N., & Kadja, G. T. M. (2022). Methanol synthesis from CO_2: A mechanistic overview. *Results in Engineering*, *16*, 100711. https://doi.org/10.1016/j.rineng.2022.100711

Ban, H., Li, C., Asami, K., & Fujimoto, K. (2014). Influence of rare-earth elements (La, Ce, Nd and Pr) on the performance of Cu/Zn/Zr Catalyst for CH_3OH synthesis from CO_2. *Catalysis Communications*, *54*, 50–54. https://doi.org/10.1016/j.catcom.2014.05.014

Balachandar, G., Khanna, N., & Das, D. (2013). Biohydrogen Production from Organic Wastes by Dark Fermentation. *Biohydrogen*, 103–144. https://doi.org/10.1016/b978-0-444-59555-3.00006-4

Brauer, G. (1965). Manganese. In *Handbook of Preparative Inorganic Chemistry* (pp. 1459–1460). essay, Academic Press

Brunauer, S., Emmett, P. H., & Teller, E. (1938). Adsorption of gases in multimolecular layers. *Journal of the American Chemical Society*, *60*(2), 309–319. https://doi.org/10.1021/ja01269a023

Bunaciu, A. A., Udristioiu E.G., & Aboul-Enein, H.Y. (2015). X-Ray Diffraction: Instrumentation and Applications. *Critical Reviews in Analytical Chemistry*, *45*(4), 289-299

Chen, X., Qu, Z., Liu, Z., & Ren, G. (2022). Mechanism of oxidization of graphite to graphene oxide by the Hummers method. *ACS Omega*, *7*(27), 23503–23510. https://doi.org/10.1021/acsomega.2c01963

Chinchen, G. C., Denny, P. J., Parker, D. G., Spencer, M. S., & Whan, D. A. (1987). Mechanism of methanol synthesis from CO_2/CO/H_2 mixtures over copper/zinc oxide/alumina catalysts: Use OF14C-labelled reactants. *Applied Catalysis*, *30*(2), 333–338. https://doi.org/10.1016/s0166-9834(00)84123-8

Cui, X., Liu, Y., Yan, W., Xue, Y., Mei, Y., Li, J., Gao, X., Zhang, H., Zhu, S., Niu, Y., & Deng, T. (2023). Enhancing methanol selectivity of commercial Cu/ZnO/Al_2O_3 Catalyst in CO_2 hydrogenation by Surface Silylation. *Applied Catalysis B: Environmental*, *339*, 123099. https://doi.org/10.1016/j.apcatb.2023.123099

Deka, T. J., Osman, A. I., Baruah, D. C., & Rooney, D. W. (2022). Methanol fuel production, utilization, and Techno-Economy: A Review. *Environmental Chemistry Letters*, *20*(6), 3525–3554. https://doi.org/10.1007/s10311-022-01485-y

Denise, B., Sneeden, R. P. A., & Hamon, C. (1982). Hydrocondensation of carbon dioxide: IV. *Journal of Molecular Catalysis*, *17*(2–3), 359–366. https://doi.org/10.1016/0304-5102(82)85047-5

Duma, Z. G., Dyosiba, X., Moma, J., Langmi, H. W., Louis, B., Parkhomenko, K., & Musyoka, N. M. (2022). Thermocatalytic hydrogenation of CO_2 to methanol using Cu-ZnO bimetallic catalysts supported on metal–organic frameworks. *Catalysts*, *12*(4), 401. https://doi.org/10.3390/catal12040401

EPA (2023) Inventory of U.S. Greenhouse Gas Emissions and Sinks: 1990-2021. U.S. Environmental Protection Agency, EPA 430-R-23-002. https://www.epa.gov/ghgemissions/inventory-us-greenhouse-gas-emissions-andsinks-1990-2021.

Friedlingstein, P., O'Sullivan, et al.. (2022). Global Carbon Budget 2022. *Earth System Science Data, 14*(11), 4811-4900. doi:10.5194/essd-14-4811-2022

Galarneau, A., Mehlhorn, D., Guenneau, F., Coasne, B., Villemot, F., Minoux, D., Aquino, C., & Dath, J.-P. (2018). Specific surface area determination for microporous/mesoporous materials: The case of mesoporous fau-y zeolites. *Langmuir*, *34*(47), 14134–14142. https://doi.org/10.1021/acs.langmuir.8b02144

Goehna H. & Koenig P. (1994). Producing methanol from CO_2. Chemtech; (United States) 36–39.

Goldstein, Lyman, Newbury, Echlin, Joy, Lifshin, Michael, Sawyer, & Goldstein. (2003). *Scanning electron microscopy and X-ray microanalysis*. Kluwer Academic.

Guczi, L., Molnár, & Teschner, D. (2013). Hydrogenation reactions: Concepts and practice. *Comprehensive Inorganic Chemistry II*, 421–457. https://doi.org/10.1016/b978-0-08-097774-4.00713-0

Hannah Ritchie and Pablo Rosado (2017) - “Fossil fuels” Published online at OurWorldInData.org. Retrieved from: 'https://ourworldindata.org/fossil-fuels' [Online Resource]

Hu, J.-C. (2023). *Hydrophobic h-BN Supported Cu/ZnO for CO_2 Hydrogenation to Methanol*. https://doi.org/http://tdr.lib.ntu.edu.tw/jspui/handle/123456789/88212

Hummers, W. S., & Offeman, R. E. (1958). Preparation of graphitic oxide. *Journal of the American Chemical Society*, *80*(6), 1339–1339. https://doi.org/10.1021/ja01539a017

IEA (2023), World Energy Outlook 2023, IEA, Paris https://www.iea.org/reports/world-energy-outlook-2023, License: CC BY 4.0 (report); CC BY NC SA 4.0 (Annex A)

Ishii, T., & Kyotani, T. (2016). Temperature programmed desorption. *Materials Science and Engineering of Carbon*, 287–305. https://doi.org/10.1016/b978-0-12-805256-3.00014-3

Jedrzejczak-Silicka, M., Trukawka, M., Dudziak, M., Piotrowska, K., & Mijowska, E. (2018). Hexagonal boron nitride functionalized with au nanoparticles—properties and potential biological applications. *Nanomaterials, 8*(8), 605. https://doi.org/10.3390/nano8080605

Jiang, S., Weng, Y., Ren, Y., Meng, S., Li, X., Huang, C., Zhang, Y., & Sun, Q. (2023). Conversion of CO_2 Hydrogenation to Methanol over K/Ni Promoted MoS_2/MgO Catalyst. *Catalysts, 13*(7), 1030. https://doi.org/10.3390/catal13071030

Kammerer, S., Borho, I., Jung, J., & Schmidt, M. S. (2022). Review: CO_2 capturing methods of the last two decades. *International Journal of Environmental Science and Technology*, *20*(7), 8087–8104. https://doi.org/10.1007/s13762-022-04680-0

Kattel, S., Liu, P., & Chen, J. G. (2017). Tuning selectivity of CO_2 Hydrogenation reactions at the metal/oxide interface. *Journal of the American Chemical Society*, *139*(29), 9739–9754. https://doi.org/10.1021/jacs.7b05362

Kaur, G., & Sharma, S. (2018). Gas Chromatography – A Brief Review. *International Journal Of Information and Computing Science*, *5*(7).

Khan, S. A., Khan, S. B., Khan, L. U., Farooq, A., Akhtar, K., & Asiri, A. M. (2018). Fourier transform infrared spectroscopy: Fundamentals and application in functional groups and nanomaterials characterization. *Handbook of Materials Characterization*, 317–344. https://doi.org/10.1007/978-3-319-92955-2_9

Kitson, F. G., Larsen, B. S., & McEwen, C. N. (1996). What is GC/MS? *Gas Chromatography and Mass Spectrometry*, 3–23. https://doi.org/10.1016/b978-012483385-2/50002-6

Klier, K. (1982). Methanol synthesis. *Advances in Catalysis*, 243–313. https://doi.org/10.1016/s0360-0564(08)60455-1

Krishna, D. N., & Philip, J. (2022). Review on surface-characterization applications of X-ray photoelectron spectroscopy (XPS): Recent developments and challenges. *Applied Surface Science Advances*, *12*, 100332. https://doi.org/10.1016/j.apsadv.2022.100332

Kundu, A., Shul, Y. G., & Kim, D. H. (2007). Methanol reforming processes. *Advances in Fuel Cells*, 419–472. https://doi.org/10.1016/s1752-301x(07)80012-3

Li, S., Guo, L., & Ishihara, T. (2020). Hydrogenation of CO_2 to methanol over Cu/AlCeO catalyst. *Catalysis Today*, *339*, 352–361. https://doi.org/10.1016/j.cattod.2019.01.015

Lin, L., Yao, S., Rui, N., Han, L., Zhang, F., Gerlak, C. A., Liu, Z., Cen, J., Song, L., Senanayake, S. D., Xin, H. L., Chen, J. G., & Rodriguez, J. A. (2019). Conversion of CO_2 on a highly active and stable Cu/FeO_x/CeO_2 catalyst: Tuning catalytic performance by oxide-oxide interactions. *Catalysis Science & Technology*, *9*(14), 3735–3742. https://doi.org/10.1039/c9cy00722a

Liu, G., Hagelin-Weaver, H., & Welt, B. (2023). A concise review of catalytic synthesis of methanol from synthesis gas. *Waste*, *1*(1), 228–248. https://doi.org/10.3390/waste1010015

Liu, Z., Li, J., Ruan, Q., Zhang, K., Ma, W., Dong, H., & Wang, R. (2018). Probing the optimal thermohydrogen processing conditions of titanium alloy shavings via chemisorption method. *International Journal of Hydrogen Energy*, *43*(45), 20783–20794. https://doi.org/10.1016/j.ijhydene.2018.09.081

López, M. del, Palomino, J. L., Silva, M. L., & Izquierdo, A. R. (2016). Optimization of the synthesis procedures of graphene and graphite oxide. *Recent Advances in Graphene Research*. https://doi.org/10.5772/63752

Marcano, D. C., Kosynkin, D. V., Berlin, J. M., Sinitskii, A., Sun, Z., Slesarev, A., Alemany, L. B., Lu, W., & Tour, J. M. (2010). Improved synthesis of graphene oxide. *ACS Nano*, *4*(8), 4806–4814. https://doi.org/10.1021/nn1006368

Maradin, D. (2021). Advantages and disadvantages of renewable energy sources utilization. *International Journal of Energy Economics and Policy*, *11*(3), 176–183. https://doi.org/10.32479/ijeep.11027

Martínez-Jiménez, C., Chow, A., Smith McWilliams, A. D., & Martí, A. A. (2023). Hexagonal boron nitride exfoliation and dispersion. *Nanoscale*, *15*(42), 16836–16873. https://doi.org/10.1039/d3nr03941b

Mohtar, S. S., Aziz, F., Ismail, A. F., Sambudi, N. S., Abdullah, H., Rosli, A. N., & Ohtani, B. (2021). Impact of doping and additive applications on photocatalyst textural properties in removing organic pollutants: A Review. *Catalysts*, *11*(10), 1160. https://doi.org/10.3390/catal11101160

Monajjemi, M. (2017). Graphene/(h-BN) n/x-doped graphene as anode material in lithium ion batteries (x=Li, be, b and N). *Macedonian Journal of Chemistry and Chemical Engineering*, *36*(1), 101. https://doi.org/10.20450/mjcce.2017.1134

Murthy, P. S., Liang, W., Jiang, Y., & Huang, J. (2021). Cu-based Nanocatalysts for CO_2 Hydrogenation to Methanol. *Energy & Fuels*, *35*(10), 8558–8584. https://doi.org/10.1021/acs.energyfuels.1c00625

Obeidat, Y. (2021). The most common methods for breath acetone concentration detection: A Review. *IEEE Sensors Journal*, *21*(13), 14540–14558. https://doi.org/10.1109/jsen.2021.3074610

Ojeda, J. J., & Dittrich, M. (2012). Fourier transform infrared spectroscopy for molecular analysis of Microbial Cells. *Microbial Systems Biology*, 187–211. https://doi.org/10.1007/978-1-61779-827-6_8

Ojelade, O. A., & Zaman, S. F. (2019). CO_2 Hydrogenation to Methanol over $PdZn/CeO_2$ Catalyst. https://doi.org/10.7546/crabs.2019.06.05

Owusu, P. A., & Asumadu-Sarkodie, S. (2016). A review of renewable energy sources, sustainability issues and climate change mitigation. *Cogent Engineering*, *3*(1), 1167990. https://doi.org/10.1080/23311916.2016.1167990

Peppas, A., Kottaridis, S., Politi, C., & Angelopoulos, P. M. (2023). Carbon capture utilisation and storage in extractive industries for Methanol Production. *Eng*, *4*(1), 480–506. https://doi.org/10.3390/eng4010029

Rohde, R. (2023, March 29). *Global temperature report for 2022*. Berkeley Earth. https://berkeleyearth.org/global-temperature-report-for-2022/

Sahu, T. K., Ranjan, P., & Kumar, P. (2021). Chemical exfoliation synthesis of boron nitride and molybdenum disulfide 2D sheets via modified hummers' method. *Emergent Materials*, *4*(3), 645–654. https://doi.org/10.1007/s42247-021-00170-0

Shen, W.-J., Ichihashi, Y., & Matsumura, Y. (2005). Low temperature methanol synthesis from carbon monoxide and hydrogen over Ceria supported copper catalyst. *Applied Catalysis A: General*, *282*(1–2), 221–226. https://doi.org/10.1016/j.apcata.2004.12.046

Sowinska, M., Bertaud, T., Walczyk, D., Thiess, S., Calka, P., Alff, L., Walczyk, C., & Schroeder, T. (2014). In-operando hard X-ray photoelectron spectroscopy study on the impact of current compliance and switching cycles on oxygen and carbon defects in resistive switching TI/HFO2/Tin Cells. *Journal of Applied Physics*, *115*(20). https://doi.org/10.1063/1.4879678

Studt, F., Behrens, M., Kunkes, E. L., Thomas, N., Zander, S., Tarasov, A., Schumann, J., Frei, E., Varley, J. B., Abild-Pedersen, F., Nørskov, J. K., & Schlögl, R. (2015). The Mechanism of CO and CO_2 Hydrogenation to Methanol over Cu-based Catalysts. *ChemCatChem*, *7*(7), 1105–1111. https://doi.org/10.1002/cctc.201500123

Todaro, S., Frusteri, F., Wawrzyńczak, D., Majchrzak-Kucęba, I., Pérez-Robles, J.-F., Cannilla, C., & Bonura, G. (2022). Copper and iron cooperation on micro-spherical silica during methanol synthesis via CO_2 hydrogenation. *Catalysts*, *12*(6), 603. https://doi.org/10.3390/catal12060603

Vali, S.A., Moral-Vico, J., Font, X. *et al.* (2024). Cu/ZnO/CeO_2 Supported on MOF-5 as a Novel Catalyst for the CO_2 Hydrogenation to Methanol: A Mechanistic Study on the Effect of CeO_2 and MOF-5 on Active Sites. *Catal Lett*. https://doi.org/10.1007/s10562-023-04554-1

Wang, C., Li, Y., Xu, C., Badawy, T., Sahu, A., & Jiang, C. (2019). Methanol as an octane booster for gasoline fuels. *Fuel*, *248*, 76–84. https://doi.org/10.1016/j.fuel.2019.02.128

Wang, G., Mao, D., Guo, X., & Yu, J. (2019). Methanol synthesis from CO_2 hydrogenation over Cuo-ZnO-ZrO_2-M_xO_y catalysts (M=Cr, Mo and W). *International Journal of Hydrogen Energy*, *44*(8), 4197–4207. https://doi.org/10.1016/j.ijhydene.2018.12.131

Wang, L., Etim, U. J., Zhang, C., Amirav, L., & Zhong, Z. (2022). CO_2 activation and Hydrogenation on Cu-ZnO/Al_2O_3 nanorod catalysts: An in situ FTIR Study. *Nanomaterials*, *12*(15), 2527. https://doi.org/10.3390/nano12152527

Wu, J. C.-S., Lin, Z.-A., Pan, J.-W., & Rei, M.-H. (2001). A novel boron nitride supported Pt catalyst for VOC incineration. *Applied Catalysis A: General*, *219*(1–2), 117–124. https://doi.org/10.1016/s0926-860x(01)00673-1

Wurzel, T. (2006). "Lurgi MegaMethanol technology. Delivering the building blocks for the future fuel and monomer demand." Germany.

Xie, Z., Hei, J., Li, C., Yin, X., Wu, F., Cheng, L., & Meng, S. (2023). Constructing carbon supported copper-based catalysts for efficient co2 hydrogenation to methanol. *RSC Advances*, *13*(21), 14554–14564. https://doi.org/10.1039/d3ra01502e

Xu, Y., & Zhao, F. (2023). Impact of energy depletion, human development, and income distribution on Natural Resource Sustainability. *Resources Policy*, *83*, 103531. https://doi.org/10.1016/j.resourpol.2023.103531

Yan, Y., Wong, R. J., Ma, Z., Donat, F., Xi, S., Saqline, S., Fan, Q., Du, Y., Borgna, A., He, Q., Müller, C. R., Chen, W., Lapkin, A. A., & Liu, W. (2022). CO_2 hydrogenation to methanol on tungsten-doped Cu/CeO_2 catalysts. *Applied Catalysis B: Environmental*, *306*, 121098. https://doi.org/10.1016/j.apcatb.2022.121098

Yang, N., Kang, F., Zhang, K., Zhou, Y., & Lin, W.-F. (2023). A strategy for CO_2 capture and utilization towards methanol production at industrial scale: An integrated highly efficient process based on multi-criteria assessment. *Energy Conversion and Management*, *293*, 117516. https://doi.org/10.1016/j.enconman.2023.117516

Yang, Y.-N., Huang, C.-W., Nguyen, V.-H., & Wu, J. C.-S. (2022). Enhanced methanol production by two-stage reaction of CO_2 hydrogenation at Atmospheric Pressure. *Catalysis Communications*, *162*, 106373. https://doi.org/10.1016/j.catcom.2021.106373

Zhu, Jiadong & Su, Ya-Qiong & Chai, Jiachun & Muravev, Valery & Kosinov, Nikolay & Hensen, Emiel. (2020). *Mechanism and Nature of Active Sites for Methanol Synthesis from CO/CO_2 on Cu/CeO_2.* ACS Catalysis. 10. 11532-11544. 10.1021/acscatal.0c02909.

Zhu, T., Song, H., Li, F., & Chen, Y. (2020). Hydrodeoxygenation of benzofuran over bimetallic Ni-cu/γ-al2o3 catalysts. *Catalysts*, *10*(3), 274. https://doi.org/10.3390/catal10030274

AUTOBIOGRAPHY

Elicia Kusuma was born in Medan, Indonesia on August 7, 1999. She finished her undergraduate in Bandung Institute of Technology, Bandung, Indonesia in the Department of Chemical Engineering in 2021. She continued her master degree in National Taiwan University's Department of Chemical Engineering from 2022-2024.

doi:10.6342/NTU202403130